Porosity engineering of MOF-based materials for electrochemical energy storage

Ran Du,[1] Yifan Wu,[2] Yuchen Yang,[3] Tingting Zhai*,[1]* Tao Zhou,[2] Qiyao Shang,[3] Lihua Zhu,[2,3,4] Congxiao Shang[2,3] and Zhengxiao Guo[1,2,3]**

[1] Department of Mechanical Engineering, The University of Hong Kong, Hong Kong SAR, China;

[2] Department of Chemistry, The University of Hong Kong, Hong Kong SAR, China;

[3] Zhejiang Institute of Research and Innovation, The University of Hong Kong, Hangzhou, China;

[4] College of Chemistry and Chemical Engineering, Faculty of Materials Metallurgy and Chemistry, Jiangxi University of Science and Technology, Ganzhou 341000, Jiang Xi, China.

Abstract

Metal-organic frameworks (MOFs) feature rich chemistry, ordered micro-/meso- porous structure and uniformly distributed active sites, offering great scope for electrochemical energy storage (EES) applications. Given the particular importance of porosity for charge transport and catalysis, a critical assessment of its design, formation and engineering is highly needed for the development and optimization of EES devices. Such efforts can be realized via the design of reticular chemistry, multi-scale pore engineering, synthesis methodologies and post-synthesis treatment, which remarkably expand their scope of applications. Particularly, by imparting conductive backbones, guest compounds and/or redox-active centers, MOFs and their derivatives have been heavily explored for EES in the last decade. To improve the design of MOF-based materials for EES, the strategies of pore architecturing of MOFs and their derivatives are systematically analysed and their applications reviewed for supercapacitors and metal-ion batteries. Potential challenges and future opportunities are also discussed to guide future development.

1. Introduction

Global energy and environmental challenges have driven extensive development of sustainable and clean energy technologies in decades. Energy storage is of particular importance to resolve the intermittency of renewable energy sources (*e.g.*, solar, wind and tidal), the efficiency and frequency balancing of electricity grids, and the electrification of transport. In this regard, one of the most promising strategies is to develop electrochemical energy storage (EES) —primarily supercapacitors and metal-ion batteries (MIBs, *e.g.*, lithium-ion batteries (LIBs), sodium-ion batteries (SIBs), and potassium-ion batteries (PIBs)).

Both supercapacitors and batteries typically consist of current collectors, electrodes, electrolyte and a separator. By applying a suitable potential between current collectors, the charge/discharge process takes place mediated by the electrode materials, and the electrolyte ions (*i.e.*, the charge carriers) are accordingly driven to travel across the separator so as to connect the circuit. In recent years, solid-state electrolytes (SSEs) are also under popular development to enhance cell voltage (energy density) and safety of the devices.[1] Upon charging, electrical energy is converted to electrostatic potential for supercapacitors and to chemical energy for batteries, and vice versa. Therefore, each device has pros and cons. Supercapacitors usually provide a high power density (*i.e.*, a fast charge/discharge velocity) due to the fast physical charge-discharge process across the interfaces between electrode materials and the electrolyte solutions, while the energy density is usually small (~5 Wh kg^{-1}). In comparison, batteries often offer a large energy density (*i.e.*, a large specific energy capacity of ~200 Wh kg^{-1}) attributed to the chemical redox reactions which take place throughout the whole volume of electrode materials, while the operation rate is relatively slow.[2]

To construct desirable energy storage devices, porous materials have been widely adopted, particularly for electrodes and SSEs. These materials typically feature a large fraction of interconnected or reticulated porosity with a high specific surface area (SSA), offering numerous potential active sites and mass transfer channels. For example, porous materials based on nanocarbons (*e.g.*, carbon nanotubes, graphene), conducting polymers, and conjugated microporous polymers (CMPs) with high electrical conductivity and large SSAs have been frequently adopted for supercapacitors,[3] while porous carbons, MoS$_2$, and metal oxides have been used for LIBs because of the theoretically large stoichiometric lithium content in the respectively lithiated compound and an accelerated Li diffusion rate inside the pores.[4-6] Despite considerable progress made so far, these porous materials fall short of sufficiently large

SSAs and readily tunable pores, which constrain the upper limit for the performance optimization and affect an accurate investigation of the structure-performance relationship.

Metal-organic frameworks (MOFs) are a class of porous materials formed by interconnected metal-centered nodes (single-metal nodes, such as Zn^{2+} in ZIF-8, or polynuclear clusters, *known commonly as* secondary building units (SBUs), such as $Zr_6O_4(OH)_4$ in UiO-66), with polytopic organic linkers, as proposed originally by Yaghi *et al.* in 1995.[7] Compared to single-metal nodes, the SBU clusters are thermodynamically stable via strong covalent bonds, and further impart architectural and mechanical stability by relatively strong directional bonds to pin down the positions of the metal centres. Such "directionality" determines further the directional bonding with the linkers, and eventually the topological structure of the resulting MOF.[8-9] The judicious assembly of suitable SBUs with different linkers can generate different types of MOFs with predictable long-range order of porous structures (size, shape and reticularity) with uniformly distributed active sites or functionalities, unmatched by other porous materials. As a result, MOFs can show remarkable nano-confinement effects, while also hold the record-high SSAs from experimental results (7839 m^2 g^{-1} for DUT-60) and theoretical predictions (14600 m^2 g^{-1}) among all as-known materials.[10-11] More importantly, a huge library of available SBUs and linkers endow remarkable flexibility for synthesis, resulting in over 100 thousand structures as documented in Cambridge Crystallographic Data Centre in August 2020 (the classification has been summarized in Reticular Chemistry Structure Resource). This fact not only enables highly designable and well-defined pore structures (geometry, volume, aperture size, *etc.*) across a large length scale (from subnanometer to several tens of nanometers), but also allows MOFs to be furnished with versatile chemistry.[12-13] By further integration with other strategies (*e.g.*, templating, 3D-printing, and self-assembly), it is now possible to generate MOFs with controlled micro- (< 2 nm), meso- (2–50 nm), or macropores (>50 nm),[14-15] allowing for stepwise and precise tailoring of their functionalities, and rendering them as ideal platforms for mechanistic studies and diverse applications.

Conventionally, MOFs are primarily targeted for gas adsorption/separation, drug delivery and catalysis. More recently, there is increasing interest in employing MOFs in EES devices, due to substantial advancement in the design and synthesis of new structures, such as anchoring redox-active metal centers/linkers on MOFs,[16] improving the electrical conductivity via highly-conjugated backbones[17-18] or conjugated guest molecules[19]. Of particular interest are the rapidly growing number of reports on MOFs for energy storage, including supercapacitors[20] and LIBs[21-22], as noted from **Figure 1**. By the control of pore size, the applications have been further extended to SIBs and PIBs in the recent years.[23-24]

Moreover, MOFs can also be further modified, predominantly by controlled annealing of as-prepared MOFs in a specific atmosphere.[25] Such MOF derivatives include porous carbon, metal oxides, metal oxides/carbon, metal sulfides/carbon, metal selenides/carbon, metal nitrides/carbon, and metal/carbon — even with some surface ligand groups.[26-34] The derivatives can inherit unique structural attributes of MOFs (e.g., high porosities and large SSAs), gain hierarchically-structured pores and enhanced electrical conductivity, and attain new chemistry for enhanced selectivity in sorption and catalysis. By judiciously devising MOF precursors and tailoring processing parameters, it is possible to manipulate the chemistry and structure of MOF-derived materials,[35-36] optimizing their beneficial functionalities for supercapacitors and batteries.[37-39]

Despite substantial progress in the design and application of MOF-based materials for EES, formidable challenges remain, such as large-SSA-induced low initial Coulombic efficiencies (CEs), low-electrical-conductivity-directed poor rate capacities and energy loss, lack of investigation of the correlation between the device performance and redox stability of MOFs, undefined-voltage-profile-led low energy density for MIBs, as well as narrow voltage windows (typically < 0.8 V) adopted for supercapacitors. Additionally, because of the potential knowledge gap between MOF researchers and supercapacitor/battery researchers, discussions on the MOF-based energy storage devices need to be more carefully. A few recent reviews have summarized the synthesis methodologies of MOFs and/or their derivatives,[13, 35-36] or documented their applications in energy storage (e.g., supercapacitors,[37, 40] electrodes for batteries,[41-44] and electrolytes for batteries[45]). However, with a wide range of pore structures and chemistry, a comprehensive overview is still lacking, particularly on the design and control of multi-scale (micro-, meso- and macro-) pores in MOF-based structures and their specific influences on energy storage.

In this regard, the current manuscript aims to provide a systematic and the state-of-the-art assessment focusing on (1) methods for designing multi-scale pores of MOFs and MOF-derivatives and (2) application of such approaches to explore the underlying mechanisms and to boost the performance of supercapacitors or MIBs. Following the Introduction, the significance and manipulation strategies for both the pore structures and the pore chemistry of MOF-based materials are elaborated. Then, their applications for supercapacitors and MIBs are overviewed, respectively — highlighting the importance of pore architecturing for performance optimization. Finally, further challenges and opportunities are discussed for both fundamental studies and energy storage applications in relation to porosity engineering of MOF-based materials.

2. Porosity engineering of MOF-based materials

Both structure and chemistry of pores are important in dictating properties and functionalities of MOFs. Considerable progresses in synthesis methodologies and characterization techniques across organic synthesis chemistry, reticular chemistry and material science have led to practical tuning of a wide range of pore sizes and chemistry of MOF-based materials, thus extending their applications.

2.1. Significance of pores for EES

Pores are ubiquitous in natural and artificial solids, which can be utilized to channel and tailor chemical interactions. By controlling the aperture size, volume, shape and reticulation of pores, as well as its environment, we can create the smallest reactors, kinetic pathways and purposely selected products. The relatively large internal space can also tolerate remarkable deformation and accommodate specific guest molecules to confine certain reactions. These features have led to a spurt of research activities on porous materials across a wide range of fields, including molecule storage, separation, catalysis and drug delivery.[46] The application of porous materials has recently been extended to the EES field, due to the unique advantages of rich reactive sites (large SSAs) and enhanced mass transfer (interconnected voids)

Supercapacitors and metal-ion batteries are the main EES devices. For a pure electrochemical supercapacitor, *i.e.*, an electrochemical double-layered capacitor (EDLC), oppositely charged electrolyte ions will be physically adsorbed on electrode surfaces by electrostatic interactions and form an electrochemical double layer upon charging (the effective thickness of the EDL is characterized as the Debye length), thus storing energy between the electrode surface and Helmholtz planes.[47] For this EDL storage mechanism, a large SSA and a high electrical conductivity are required to maximize the number of adsorbed ions and to reduce the *iR* drop

(*i.e.*, the energy loss), respectively; meanwhile, an appropriate pore size distribution (PSD) is necessary to satisfy a large SSA, a fast mass transfer, and a sufficiently high volume-normalized energy/power density. Particularly, when the size of pores is down to the nanoscale / sub-nanoscale, quantum confinement effects appear and can be tuned to promote performance, e.g. by breaking the Coulombic ordering.[48] Besides structural consideration, judicious modification of the chemical compositions of electrode materials can further enhance the capacitance by activating the Faradic charge storage mechanism. In such cases, redox-active materials, such as metal oxides (*e.g.*, MnO_2 and RuO_2) and conducting polymers (*e.g.*, polyaniline, polythiophene, and polypyrrole), are frequently employed,[49] where reversible surface redox reactions contribute to additional capacitance though at the expense of a relatively slow kinetics compared with EDLC.

Regarding MIBs, the conversion of electrical energy to chemical energy accounts for the energy storage, and vice versa — which is mediated by the transportation and diffusion-limited redox reactions of specific metal ions (*e.g.*, Li^+, Na^+, and K^+). Upon charging, metal ions leave the cathode (positive) electrode (*e.g.*, delithiation for Li^+ batteries) and travel to the anode (negative) electrode, where those are reduced to zero-valence atoms (*i.e.*, lithiation). In this way, the electrical energy is converted to chemical energy as presented by the difference of working potentials between the two electrodes. The charge/discharge process is based either on metal-ion-intercalation or conversion-reaction mechanisms,[6, 50] both of which can potentially proceed throughout the whole electrode materials. Therefore, it is essential to design materials with a high theoretical capacity as well as a large voltage window to boost the energy density, and a high electrical conductivity as well as an appropriate PSD to promote the rate performance by facilitating charge/mass transfer. For example, compared to widely-studied LIBs, the larger size of metal ions in SIBs and PIBs (*i.e.*, Na^+ and K^+) necessitates larger pore sizes, so as to accommodate the corresponding ions for operation.

Among different types of porous materials, MOFs stand out for their highly reticulated, long-range-ordered and tunable pore structures. It is easy to attain large SSAs and pore volumes by judicious design of respective components (*i.e.*, metal-based nodes and organic linkers). Very recently, a record-high SSA (7839 m^2 g^{-1}) and porosity (5.02 cm^3 g^{-1}) has been obtained for a mesoporous DUT-60 MOF, which further suggests unprecedented potential towards energy storage. Although conventional MOFs feature an inferior electrical conductivity which retards EES, this issue has been partially overcome by using conductive additives (*e.g.*, acetylene black [51-52]) or highly-conjugated organic linkers[53-54]. On the other hand, MOF-derived materials obtained by post-treatment of MOFs contribute to another category of promising porous materials. Such structures partly inherit the original structural attributes of MOFs and can gain substantial electrical conductivity, stability and chemical selectivity by post-treatment process (*e.g.*, annealing).[55-57] From the next section, the strategies for synthesizing structure/chemistry-tailored MOF-based materials will be discussed in detail.

2.2. Pore architecturing for MOFs

Synthesis of MOFs involves the knowledge of conventional organic chemistry, reticular chemistry and coordination chemistry.[58] As schemed in **Figure 2a**, the formation of MOFs can be conceptualized as the assembly of polyhydra (*i.e.* metal nodes) and lines (*i.e.* linkers) via the coordinating interactions between metal clusters/ions and organic ligands along specific directions, leading to the formation of long-range-ordered frameworks featuring specific topologies. MOFs are thermodynamically unstable with respect to their dense phase, because the smaller amounts of bonds and dispersive interactions between the voids tend to cause the collapse of pores. Nevertheless, the metastability (*i.e.*, kinetic stability) can be achieved by raising the energy barrier via using inert metal ions (with low ligand-exchange kinetics), employing strong metal-ligand bonds (e.g., increase the donor strength of the ligand or the valency of the metal ion), and enhancing the connectivity between linkers and nodes, accounting for the stability of MOFs.[59] It is fascinating to note that the structure and chemistry of resulting MOFs can be well devised by considering the geometry and functionality of metal nodes and ligands, which is generally realized by retro-synthetic and *de novo* reticular design.[13] For the retro-synthetic design (also known as isoreticular approach), with a target topology as a blueprint, desirable molecular equivalents of the geometric units are chosen as building blocks for establishing a framework. For *de novo* design, starting with subtly designed molecular building blocks with desirable geometry and chemistry, it is possible to explore new topological structures. Such highly tunable structure/chemistry and ordered pores make MOF an ideal platform for mechanistic studies and for applications in a wide range of fields.

To modulate properties and functions of MOFs, it is essential to tailor both pore structures (*e.g.*, size, volume, and topology) and pore chemistry (*e.g.*, chemical composition/functionalities of metal secondary building units and ligands). Generally, the design strategies can be classified into four groups, *i.e.*, 1) molecular design, 2) templating, 3) controlled assembly, and 4) defect

engineering (**Figure 2b-e**). To systematically and clearly demonstrate these tactics, we will delineate them from perspectives of pore chemistry and pore structure design. Particularly, in the pore structure subsection, the manipulation of micro-, meso- and macro- pores will be separately elaborated, so as to provide a clear picture for multiscale engineering of porosities.

2.2.1. Design of pore chemistry

Chemistry is fundamental to the structure, properties and functionalities of MOFs. On the one hand, the chemical/thermal stability and electrical conductivity of backbones can be tuned by devising strength of coordination bonds and the degree of conjugation of organic ligands, respectively; On the other hand, one or more functional sites can be uniformly installed in the long-range-ordered pores with desirable geometries, achieving 1) site isolation, 2) site coupling, or 3) site cooperation effect.[13] To realize the above, it is essential to select and modify metal-nodes and organic linkers.

Metal-node design

Metal-nodes can either be single-metal ions or metal secondary building units. Compared to single-metal nodes, the covalent-bonded SBUs are thermodynamically more stable and can provide directional bonds, thus usually offering a higher stability.[8] Tuning these metal-sites, either by changing metals or by modifying ligands coordinated to the metals, can considerably influence the electronic structure of the corresponding MOFs, thus dictating properties such as catalytic activities and the affinities towards specific gases. The corresponding modulations can be implemented by either designing building units or by post modification.

Design of metal nodes prior to MOF synthesis is a frequently adopted approach. The judisious selection of the composition of metals can exert a profound effect on the stability and the chemical properties of MOFs. For instance, Zhou's group has reported a series of isostructural

PCN-224 (Fe) analogues by linking Zr_6 clusters with diverse iron porphyrins, where Zr-based SBUs can offer relatively high stability due to the robust combinations of hard acids (high-valent metal ions, *e.g.*, Zr^{4+}) and hard bases (*i.e.*, carboxylates), and meanwhile iron porphyrin units can provide well-isolated catalytic centers.[60] In this work, the β-position of iron porphyrin units with ethyl-, bromo-, chloro-, and fluoro- groups have been pre-functionalized, so as to acquire PCN-224 (Fe) analogues with diverse compositions without affecting pore structures (pore sizes of ~1.9 nm and SSAs of 2142~2359 $m^2\,g^{-1}$) and chemical stability. They found that the bromo-functionalized MOFs showcase a remarkable catalytic selectivity towards tertiary alcohols (>99%) for oxygenation of 3-methylpentane, which is attributed to the electron-withdrawing feature of bromo-moiety.

To avoid issues such as the complexity of precursor synthesis, chemical/thermal stability of precursors under reaction conditions, compatibility of functional groups and weak crystallization ability of specific MOFs, post modification has been developed to furnish metal nodes.[61-64] This concept has been exemplified by an early work, where 1,1'-ferrocenediyl-dimethylsilane have been grafted onto the metal SBUs of $[Al(OH)-(BDC)]_n$ (MIL-53(Al), BDC=1,4-benzendicarboxylic acid) via a ring-opening reaction.[61] Another route is based on post-synthetic ion metathesis proceeding under mild conditions. As demonstrated in **Figure 3a-b**, by soaking crystals of $Zn_4O(1,4\text{-benzenedicarboxylate})_3$ (MOF-5) in concentrated DMF solutions of desirable metal salts for one week, various divalent (V^{2+}, Cr^{2+}, Mn^{2+}, Fe^{2+}) and trivalent metal ions (Ti^{3+}, V^{3+}, Cr^{3+}) have been incorporated into the metal SBUs. Powder x-ray diffraction (PXRD) patterns of those derived MOFs are similar to that of MOF-5 (**Figure 3c**), confirming a retained topological structure.

Organic linker design

Similar to the design of metal nodes, the pre- and post- modification of organic linkers can also exert a nontrivial influence on properties/functions of the resulting MOFs.

Engineering of organic linkers has been well investigated prior to MOF synthesis. Colombo *et al.* have reported Ni- and Zn- MOFs based on a series of functionalized 1,4-bis(1*H*-pyrazol-4-yl)benzene (H$_2$BDP) linkers.[65] The selectivity of MOFs towards gas mixtures containing molecules with different polarities (*e.g.*, N$_2$/CO$_2$ or CH$_4$/CO$_2$) has been remarkably improved by the substitution of specific functionalities (−NO$_2$, −NH$_2$, −OH, and −SO$_3$H) on the β-position of H$_2$BDP. Another study performed by Yaghi's group have prepared eighteen MTV-MOF-5 structures by linking Zn-based SBUs with 1,4-benzenedicarboxylate (BDC), its derivatives (-NH$_2$, -Br, -(Cl)$_2$, -NO$_2$, -(CH$_3$)$_2$, -C$_4$H$_4$, -(OC$_3$H$_5$)$_2$, and -(OC$_7$H$_7$)$_2$), or their combinations.[66] Of particular interest is that a "whole is better than the sum of its parts" (synergistic) effect has been unambiguously unveiled for a MTV-MOF-5-EHI (containing a mixture of -NO$_2$, -(OC$_3$H$_5$)$_2$ and -(OC$_7$H$_7$)$_2$) towards differentiating carbon dioxide from carbon monoxide.

Post-synthetic linker functionalization has also been well studied.[67-70] On the one hand, desirable linkers can be chemically bonded into parent MOFs to realize certain functions. In a recent study, Hu *et al.* elegantly have installed Brønsted acid and base functionalities in a Zr-based MOFs.[68] In brief, PCN-700 has been fabricated by coordinating Zr$_6$ clusters (Zr$_6$O$_4$(OH)$_8$(H$_2$O)$_4$) with H$_2$Me$_2$-BPDC linkers (H$_2$Me$_2$-BPDC = 2,2'-dimethylbiphenyl-4,4'-dicarboxylic acid) to serve as parent MOFs. In light of two-type pockets presented in the structure of PCN-700 (see **Figure 3d**), Brønsted basic (2-aminoterephthalic acid) and acidic linkers ([(1,1':4',1"-terphenyl)-2,2",4,4"-tetracarboxylic acid]) have been sequentially bonded into a network structure and thus yielded PCN-700-AB. In spite of a similar pore structure as reflected from **Figure 3e** (Brunauer–Emmett–Teller (BET) surface area of 1145–1289 m^2 g^{-1} and total pore volumes of 0.519–0.598 cm^3 g^{-1}) due to a single-crystal-to-single-crystal transformation, a striking acid-base cooperative effect have been observed. Both a high yield and a high selectivity have been achieved here using a one-pot tandem conversion reaction of benzaldehyde dimethyl acetal into benzylidene malononitrile as a model reaction.

Postsynthetic exchange (PSE), on the other hand, facilitates the replacement of inert linkers by functional ones without loss of crystallinity or porosity of parent MOFs.[69-70] It has been proven that even for stable Zr(IV)-based UiO-66 MOFs, the ligand exchange can occur in solvent through either a solid-solid reaction between microcrystals of different MOFs or a solid-liquid reaction between a specific kind MOF and free anionic ligands.[69] Kim *et al.* have reported the similar attempts to a variety of chemically robust MOFs including MIL-53(Al), MIL-68(In), and Zn(II)-based RHO-type ZIF-71, verifying the dynamic nature of the coordination between anionic ligands or cationic metal ions as well as the universality of the PSE strategy.[70]

Certain metal-containing linkers (e.g., metal-porphyrin units), can serve as a new class of linkers capable of largely expand the application territory of MOFs. For example, 36 multivariate metal−organic frameworks (MTV-MOFs) have been designed, with a general composition of $(M_3O)_2(TCPP-M)_3$ (M, metal; TCPP, tetrakis (4-carboxyphenyl) porphyrin).[71] As schemed in **Figure 3f**, the metals in trigonal metal oxide SBUs (Mn, Fe, Co, Mg, Ni and their mixtures) and porphyrin units (Mg, Co, Ni, Cu and Zn) have been separately modulated. The spatial arrangement of metals in MOFs can be precisely controlled by further taking advantage of ordered molecular structures of MOFs and alternatingly distributed SBUs and porphyrin units. In this regard, the band structures of the resulting MOFs can be well adjusted to promote their photocatalytic performance.

2.2.2. Design of pore structure

The pore structure — which includes pore size, SSA, pore volume and topological structure — is of significant importance to dictate properties and functionalities of MOFs. For example, engineering of micropores can tailor the confinement effect that enhances the performance of supercapacitors,[48] while large pores can facilitate mass transfer which benefits the rate

performance of EES devices. Moreover, judiciously devising nano/micro structures can exert an amplification effect to achieve superwettability,[72] which has been proven to affect considerably electrochemical processes.[73-74] As summarized in **Table 1**, versatile strategies have been developed to manipulate pore structures of different dimensions, from molecular (*e.g.*, the selection of linkers) to macroscopic scale (*e.g.*, templating and controlled assembly). However, it is challenging to decouple structural parameters (*e.g.*, PSD and SSA) and to control pore structure across large length scales.

Engineering of Micropores

Micropores in MOFs are dominantly stemmed from the space enclosed by the metal SBUs and organic linkers. Therefore, the modulation strategies of these intrinsic pores are mostly based on pre- and post- molecular design of building units (*i.e.*, linkers and metal nodes).

Linker design

To pre-design MOFs, micropores can be tailored by the selection of desirable organic linkers and metal SBUs as precursors. In a study, Zr-MOFs of the same metal nodes (Zr_6 cluster) while diverse topological structures have been prepared by devising linkers based on 2,2'-dihydrobiphenyl-3,3',5,5'-tetra(phenyl-4-carboxylic acid) (2,2'-H-H_4TPCB, *i.e.*, L1) and its derivatives.[75] The specific functionalization of 2,2'-H-H_4TPCB has been found to greatly influence the resulting topologies, which is rationalized by steric hindrance (**Figure 4a**). Without additional functionalization, both position 1 and position 2 can freely rotate, giving rise to a D_2-symmetry linker (*i.e.*, L1) and a PCN-605 structure accordingly. In contrast, substitution at 4,4'-positions of the biphenyl group (*e.g.*, 4,4'-NH$_2$-H4TPCB (L4)) can hinder the rotation of the inner biphenyl group and reduce the dihedral angle between the two phenyl rings to almost zero, thus leading to a C_{2h} symmetry for L4 and a PCN-606 structure for the derived MOF. By further restricting the rotation of both inner and outer biphenyl groups by substituting bulky groups (4,4'-OCp-H$_4$TPCB (L7)), pure PCN-608-structured Zr-MOF has

been obtained. The modulation of topologies can further affect pore structures, *e.g.*, uniform channels with a diameter of 1.2 nm have been found in PCN-606, while both mesoporous channels (3.3 nm) and microporous channels (1 nm) have been found in PCN-608. By using mixed ligands, the topology of resulting MOFs can be further adjusted.

Besides tuning substituents, control of the aspect ratio (AR) of linkers has been proposed by Wang *et al.*[76] In this work, three Zr-MOFs have been fabricated by solvothermal reactions, where Zr_6 clusters have been used as metal nodes and three organic ligands with similar geometry but different ARs as tetratopic linkers (3,3',5,5'-biphenyltetracarboxylate (BPTC), 3,3',5,5'-azobenzene-tetracarboxylate (ABTC), and 2',5'-dimethyl-[1,1':4',1"-terphenyl]-3,3",5,5"-tetracarboxylate (TPTC-$(Me)_2$)). Impressively, increase of ARs (from 1.45 to 1.78 and to 2.28) have greatly changed the connectivity of metal SBUs (decrease from 12 to 4 with the increase of AR) and thus the topologies of derived MOFs (**Figure 4b**). With a small-AR linker, the Zr-MOF features **ftw** topology (compound 1) which contained cubic cage-like pores (~1.2 nm). Increase of AR has resulted in a **scu** topology comprising of 1D channels with a diameter of ~0.7 nm, which has been interpreted by a severe steric hindrance induced by the high-AR linkers. A further increase of AR led to a rarely reported 4-c **lvt** topology.

In addition to employing one kind of ligand, the pore space partition strategy can split a large pore into several small pores by adopting two size-complementary ligands.[77-78] As shown in **Figure 4c**, CPM-12 based on a dimeric {$In_2(OH)$} cluster has been fabricated by using size-complementary 1,3,5-tri(4-carboxyphenyl)benzene (BTB) and 1,3,5-benzenetricarboxylic acid (BTC) ligands by one-pot synthesis, where BTB serve as pore-partition agents to split large pores.[77]

Postsynthetic modification, particularly for post ligand exchange, can serve as a complementary route to adjust pore structures of MOFs without altering the original topology.[64] As demonstrated by Karagiaridi *et al.*,[79] a pillared-paddlewheel MOF containing meso-1,2-di(4-

pyridyl)-1,2-ethanediol pillars (~0.9 nm long) has been used as the parent material (denote as SALEM-5). After solvent-assisted ligand exchange with longer pillars (1.1, 1.4, and 1.7 nm), pore sizes have been increased accordingly. Additionally, it is potentially possible to finely tune the pore structure by controlling the degree of ligand exchange and by using mixed ligands.

Metal-node design

Aside from linker design, functionalization of metal nodes can play a vital role in dictating microporosities of MOFs.[80-81] This has been exemplified with a coordination templated cyclotrimerization (CTC) reaction, where guest molecules have been bonded at specific positions/directions in pores of MOFs to promote in-pore reactions, thereby modulating porosities accordingly.[81] Briefly, $[Fe_3(\mu_3\text{-}O)(BDC)_3X(H_2O)_2]$ (MIL-88B, X = OH$^-$ / Cl$^-$ / F$^-$) has been used as a prototypical material and 1,4-benzenedicarboxylic acid (H$_2$BDC) as the host coordination template. As schemed in **Figure 4d**, taking advantage of the highly directional coordination bonds of the octahedral Fe(III) ions in MIL-88B, a [2+2+2] CTC reaction has been performed by anchoring three monomers (2,4,6-tri(pyridin-4-yl)-1,3,5-triazine (TPT)) in each pore followed by heating at 140°C within 12 h. The resulting MIL-88B-TPT has demonstrated a much higher BET surface area (S_{BET}=1113 m^2 g^{-1}) and pore volume (0.56 cm^{-3} g^{-1}) compared to original MIL-88B (with a negligible adsorption volume of nitrogen). In another study, by modification of Ni$_3$O(COO)$_6$ SBU with dimethylamine, pyridine, 4-aminopyridine, and isonicotinic acid, the accessible diameter of the cages has decreased from 1.90 nm to as small as 0.44 nm.[80]

Engineering of Mesopores

Mesopores, featuring a larger size than that of micropores (2−50 nm *vs.* <2 nm), is beneficial to promote mass transport inside networks and increase SSAs by maximizing the surface area-to-mass ratio. Since the length scale of mesopores crosses the boundary of common molecules,

hence strategies from both molecular engineering (*e.g.*, ligand design and defect engineering) and material engineering (*e.g.*, templating and controlled assembly) have been developed.

Linker design

From the conceptual model as shown in **Figure 2a**, a straight forward thought to gain the mesopores in MOFs lies in the design of ligands, so as to enlarge the original micropores by isoreticular expansion (*i.e.*, retro-synthetic design by lengthening ligands) or by modulating the topological structure (*i.e.*, de novo reticular design by altering topologies).

In early studies, repeating phenyl groups have been frequently involved to afford a robust structure for linker elongation.[82] For example, with octahedral $Zn_4O(CO_2)_6$ as nodes, isoreticular expansion has been achieved by extending the length of linkers through changing linkers from 1,4-benzenedicarboxylate 4,4',44''-benzene-1,3,5-triyl-tribenzoate (BTB) to 4,4',4''-[benzene-1,3,5-triyl-tris(ethyne-2,1-diyl)]tribenzoate (BTE) and 4,4',44''-[benzene-1,3,5-triyl-tris(benzene-4,1-diyl)]tribenzoate (BBC).[83-84] Although the resulting MOF-177, MOF-180, and MOF-200 held a same topology (**qom**), increasing pore sizes (from micropore- to mesopore-scale) and porosities (1.89 *vs.* 3.59 cm^3 g^{-1} for MOF-177 and MOF-200, respectively) have been unambiguously identified.

Later, Zhou's group has found that the effectiveness of ligand elongation through the isoreticular approach is largely affected by the pore shape or symmetry of MOFs.[85] Approximating the cross-section of a pore as a regular polygon, the diameter d of the inscribed circle of the corresponding pores has been expressed by

$$d = \frac{1}{\tan(\pi / \text{n})} \times a \qquad (1)$$

where a and n denote the length and the number of edge of the regular polygon. As a large n can efficiently enlarge the pore size as deduced from the above equation, the isoreticular approach has been applied to MIL-100 (n=12) where 1,3,5-benzenetricarboxylate (BTC) serves

as the linker.[86] As shown in **Figure 5a**, larger-dimension benzo-tris-thiophene carboxylate (BTTC) and 4,4',4"-s-triazine-2,4,6-triyl-tribenzoate (TATB) featuring pseudo- or idealized D_{3h} symmetry have been applied as linkers, yielding PCN-332 and PCN-333, respectively. In addition to micropores, mesopores with a size of 3−6 nm have been generated, which afforded their much larger porosities (*e.g.*, 3.81 cm^{-3} g^{-1} for PCN-333(Al)) compared to ~1.16 cm^{-3} g^{-1} for MIL-100.

Aside from direct synthesis, PSE strategy has also been adopted to extend the length of linkers.[87-88] Li *et al.* has linked zinc-adeninate clusters (Zn$_8$Ad$_4$O$_2^{8+}$; Ad = adeninate) with 2,6-naphthalenedicarboxylate (NDC) ligands, yielding bio-MOF-101 with continuous uninterrupted mesoporous channels as a parent MOF.[88] Afterwards, short linkers (*i.e.*, NDC) have been replaced by the longer ones proceeding via a crystal-to-crystal transformation manner (schemed in **Figure 5b**). In short, bio-MOF-101 has been successively incubated in the solution of ligands with increasing length (4,4'-biphenyldicarboxylate (BPDC), azobenzene-4,4'-dicarboxylate (ABDC), and 2'-amino-1,1':4,1"-terphenyl-4,4"-dicarboxylate (NH$_2$-TPDC)) at elevated temperature (348 K), yielding bio-MOF-100, bio-MOF-102, and bio-MOF-103, respectively. As characterized by nitrogen sorption test (**Figure 5c-d**), elongation of linkers stepwise has enlarged the average pore size from ~2.0 to ~2.8 nm. Particularly, a strikingly high pore volume of 4.36 cm^{-3} g^{-1} has been obtained for bio-MOF-102.

Besides popular ligand elongation strategy in the framework of retro-synthetic design, mesopores MOFs have also been accessed through de novo reticular design. In this way, instead of lengthening organic struts, subtle ligand design plays a more vital role for altering the topology. For instance, moving beyond phenyl-only struts in linkers,[82, 84] Farha *et al.* incorporated certain more "area-efficient" acetylene as struts.[10] By solvothermal reacting copper salts and 1,3,5-tris[((1,3-carboxylic acid-5-(4-(ethynyl)phenyl))ethynyl)phenyl]-benzene (LH$_6$-2), NU-110 with a **rht**-topology has been obtained. Featuring both micropores

(~1.9 nm) and mesopores (*ca.*, 3–6 nm), ultrahigh pore volume (4.40 cm^{-3} g^{-1}) and SSA (7140 m^{-2} g^{-1}) have been observed.

Mixing of tritopic and ditopic linkers contributes to another efficient method of attaining mesopores via. topological modification.[11, 83, 89] The crosslinking of Zn-based clusters and mixed BTE/BPDC ligands has yielded MOF-210 in a **toz** topology, with the largest cage of 2.69×4.83 nm, a pore volume of 3.60 cm^{-3} g^{-1}, and a SSA of 6240 m^{-2} g^{-1}.[83] In a recent study by Kaskel's group, Zn$_4$O(BBC)$_{4/3}$(BCPBD) (*i.e.*, DUT-60) with a **ith-d** topology has been obtained by linking Zn-based clusters with tritopic BBC and ditopic bis-pcarboxyphenylbuta-1,3-diene (BCPBD) linkers.[11] As shown in **Figure 5e-f**, DUT-60 is constituted by large mesopores (3.7×4.2 nm) surrounded by eight smaller mesopores (1.5×2.7 nm). Impressively, this MOF holds the record-high pore volume (5.02 cm^{-3} g^{-1}) and SSA (7839 m^{-2} g^{-1}) reported to date.

Defect engineering

In comparison with strategies for linker design where tedious synthesis process are frequently involved, mesoporous MOFs can also be accessed by introducing defects via chemical etching or controlled thermolysis.[90-93]

As schemed in **Figure 6a**, Zhou's group reported a linker labilization approach.[93] The parent MOF has been created by firstly linking Zr$_6$-clusters with an azobenzene-based robust linker (azobenzene-4,4'-dicarboxylate, AZDC) to yield Zr-AZDC-MOF (*i.e.*, PCN-60), then by partially replacing AZDC with an imine-based pro-labile linkers (4-carboxybenzylidene-4-aminobenzate, CBAB) under low-temperature and acid-free conditions. Because of the acid sensitivity of CBAB, the as-obtained Zr-AZDC/CBAB-MOF has been subjected to acetic acid treatment, so as to controlled introduce missing-linker defects by dissociating CBAB. The pore size can be tuned from ~1.5 nm to ~20 nm by adjusting the percentage of CBAB in parent MOFs and the concentration of acetic acid. In another study, hierarchical porous MOFs have

been created by reacting metal precursors with an insufficient amounts of linkers in the presence of monocarboxylic acid (as a modulator).[90] The monocarboxylic acid can simultaneously coordinate with metal ions to form metal–oxo clusters and introduce structural defects by its alkyl chain. Taking UiO-66 ($Zr_6O_4(OH)_4(BDC)_6$, BDC=1,4-benzenedicarboxylate) as an example, by altering the chain length of the monocarboxylic acid (2~16 carbons) and its ratio with respect to organic linkers (*i.e.*, BDC), a tunable pore size ranging from *ca.* 1−10 nm has been achieved.

Besides wet-chemistry approach, removing sacrificial linkers by selective thermal decomposition contributes to an alternative route. In a UiO-66 system, mixed thermal-sensitive linkers (2-amino-1,4-benzenedicarboxylate, $BDC-NH_2$, decomposition temperature < 300 ºC) and thermal-stable linkers (BDC, decomposition temperature ~480 ºC) have been employed to construct MTV UiO-66-NH_2-R%, where R% represents the percentage BDC-NH_2 (0–41%).[92] As schemed in **Figure 6b**, the selective decomposition of thermal-sensitive linkers can generate mesopores without affecting the crystallinity of MOFs. By adjusting the R%, thermolysis temperature (325−375 ºC), and thermolysis time (0−120 min), the pore size has been manipulated from < 2 nm to ~13 nm. The thermolysis mechanism has been explained by 1) a decarboxylation process, 2) removal of resulting terminal ligands, and 3) the conversion of Zr_6 clusters to ultrasmall metal-oxide nanoparticles. However, the narrow available pore size and the influence on the structures/compositions of original MOFs may challenge its feasibility.

Templating

Instead of delicate molecular engineering of building blocks, templating is a straightforward strategy to tailor the pore size of MOFs by selection of appropriate templates. To meet the length scale of mesopores, soft templates and MOF-based templates are widely practiced.

Block copolymers and surfactants are two typical soft templates for tailoring mesoporosities of MOFs. A low-cost nonionic triblock copolymer (*i.e.*, pluronic P123, also known as a nonionic

surfactant) has been reported to prepare mesoporous HKUST-1 by templating its micelles in DMF.[94] By modulating the amount of P123 in the precursor solution, pronounced mesoporous (*ca.* 3−30 nm) have been evidenced from nitrogen sorption test and TEM observation. In another study, mesoporous HKUST-1 has been fabricated by using a combination of a positively-charged surfactant (cetyltrimethylammonium bromide, CTAB) and a chelating agent (hydroxy polyacid) as templates.[95] Here, citric acid serves as a mediator to bridge MOFs (via chelating metal ions) and surfactant molecules (via electrostatic attraction), thus activating the structure-directing function of CTAB and yielding mesopores centering around 19.6 nm. However, templates have been left in the products for the aforementioned two examples and may shield intrinsic properties of MOFs. For another work, MOF-5 with highly-ordered hexagonal pores have been obtained in an emulsion system containing a surfactant (N-ethyl perfluorooctylsulfonamide), an ionic liquid (1,1,3,3-tetramethylguanidinium acetate), and supercritical CO_2.[96] The underlying mechanism has been explained by the conformal growth of MOFs along the external walls of cylindrical surfactant micelles, thus generating neat MOFs with well-ordered mesopores after removing all exotic substances. Despite a high purity of resulting MOFs, this method may suffer from high cost of specific surfactants and ionic liquids.

Aside from soft templates, MOF itself has also been implemented as a template. It is well-known that MOFs with high-valent metal ions (*e.g.*, Zr^{4+}) are typically much more stable than those with low-valent metal ions (*e.g.*, Zn^{2+}), which can be attributed to a robust combination between hard acids (*i.e.*, high-valent metal ions) and hard bases (carboxylate linkers). Taking advantage of the stability difference, relatively unstable MOFs may serve as a sacrificial template to impart mesopores in stable MOFs. Following this idea, Huang *et al.* have prepared hierarchical-porous UiO-66 (Zr) by templating MOF-5 (schemed in **Figure 6c**).[97] Briefly, nanosized MOF-5 particles have been in situ incorporated into the UiO-66 during the synthesis of the latter. Afterwards, the resulting MOF-5@UiO-66 has been subjected to acid aqueous

solution for etching MOF-5, thus generating hierarchical porous UiO-66. As seen from **Figure 6d**, the mesopore size can be modulated from 4 to 30 nm depending on the amounts of two MOFs. Moreover, this MOF-based templating method has been proven to be quite universal, affording diverse hierarchical porous MOFs based on ZIF-8, MIL-101 (Cr), DUT-5, *etc.*

Controlled assembly

To avoid potential impurities introduced by templates, controlled assembly appears as a greener approach to create mesoporous MOFs. This has been realized by either controlling the solvent composition or the temperature.

A switchable solvent strategy based on CO_2-expanded liquids has been proposed by Peng *et al.*, where CO_2-expanded N,N-dimethylformamide (DMF) has been used to prepare mesoporous Cu-BTC MOFs.[98] It has been deduced that small MOF building blocks have been produced in the CO_2-expanded DMF due to the reduced solvency and viscosity incurred by CO_2 expansion, which then assembled to networks driven by their high surface energy. After removal of DMF and CO_2, meso-cellular MOFs have been obtained. Since the expansion degree can be stepwise boosted by increasing the pressure of CO_2, average sizes of mesopores ranging from 13 to 23 nm (CO_2 pressure from 2.0 to 6.6 MPa) have been accordingly acquired.

In a more recent study, mesopores have been incorporated by controlled stacking microporous Cu-BTC MOFs by modulating the reaction temperature in the presence of acetic acid and triethylamine.[99] Acetic acid and triethylamine have been used to adjust the crystallization rate and prevent the formation of big crystals, while the reaction temperature can also be used to finely tune the size of obtained MOF particles. As seen from **Figure 6e-f**, with increasing temperatures, pores have been gradually enlarged from *ca.* 26 to 72 nm, and the S_{BET} gradually decreased from 1048 to 612 m^2 g^{-1}. This has been attributed to that a lower temperature facilitates the formation of smaller MOF particles and thus resulting in a tighter packing, while

bigger particles generated from a higher temperature can lead to a loose packing and thereby producing larger pores.

Engineering of Macropores

Similar to the occasion of mesopores, strategies for dealing with macropores mainly consist of defect engineering, templating, and controlled assembly.

Defect engineering

It is known that the protonation of nitrogen-containing ligands can destroy the linkage between metal nodes and organic linkers due to enhanced electrostatic repulsion, thus developing structural defects and producing large pores. As shown in **Figure 7a**, upon the treatment of ZIF-8 or ZIF-67 with a mixed xylenol orange/HCl etchant solution (pH=2.5), non-truncated rhombic dodecahedra have been preferentially etched from twelve {211} edges which contain more metal-2-MIM (2-methylimidazole) linkages.[100] In this way, pinholes have been formed at the threefold-vertices, from which the inside MOFs have been etched away and thus form hollow boxes containing submicrometer-sized macropores. In contrast, raising pH to 3.5 decreased etching rate along <211> directions, affording concave tetrahedra free of large pores (**Figure 7b**).

In another study, a large-size tannic acid (TA) has been adopted as etchant following a different etching process.[101] After incubating monodispersed ZIF-8 polyhedrons in a TA solution (5 g L^{-1}), hollow-structured ZIF-8 has been obtained with an average shell thickness of 20 nm and a cavity size >100 nm. It has been deduced that upon adsorption on the surfaces of ZIF-8 polyhedrons, TA simultaneously provides protons to etch frameworks, alters the surface wettability from hydrophobicity to hydrophilicity, and holds the integrity of the framework by utilizing its large size. Then protons can more easily penetrate into the internal space of polyhedrons through the hydrophilic surface, thus etching the inside ZIF-8 and producing

macroporous hollow structures. However, the etching strategy suffers from a low yield of resulting MOFs, inevitably increasing the cost.

Templating

To tailor macropores, hard templates are frequently used. Metal foams are known to feature pores of micrometer to sub-centimeter scales, providing a conductive template to prepare 3D macroporous MOFs that are favorable for EES. Although MOF-5 on copper foams and HKUST-1 on nickel foams have been reported,[102-103] the rigid metal foams may retard their application for flexible devices. By replacement of metal foams with flexible and low-cost polymer sponges (*e.g.*, melamine sponges), ZIF-8/sponge and PCN-224(Fe)/sponge have been fabricated by ex situ grafting and in situ growth, respectively.[104-105] However, the limited loading of MOFs, the presence of exotic skeletons, and the non-ordered porous structures of those composites can largely limit the exploration and maximization of the excellent properties of MOFs.

In this regard, Shen *et al.* have reported ordered macro-microporous ZIF-8 single crystals by templating polystyrene (PS) spheres.[106] As schemed in **Figure 7c**, 2-MIM and zinc salts have been filled into the interstices of 3D monolith assembled from monodisperse PS spheres, which have been subsequently soaked in $CH_3OH/NH_3 \cdot H_2O$ solutions, thus yielding single-crystal ordered macroporous ZIF-8 (SOM-ZIF-8) after removal of PS spheres with tetrahydrofuran. As revealed by scanning electron microscopy (SEM), individual ZIF-8 crystals grown on the external surface of the PS template have been clearly shown (**Figure 7d**). High-angle annular dark-field scanning transmission electron microscopy (HAADF-STEM) further confirm highly-ordered macroporous structure of SOM-ZIF-8 (**Figure 7e-f**), where the pore size of macropores can be simply adjusted from 191 to 466 nm by using PS spheres of respective diameters. As expected, the introduction of macropores caused negligible influence on the SSA and total pore volume as given by nitrogen sorption test, because the detection range of gas

sorption technique is mainly located in the micro- and mesopore region (*i.e.*, pore size <50 nm) and the contribution of SSA by large pores is negligible.

Controlled assembly

To gain macroporosity, free of templates, it is feasible to assemble MOFs to form aerogels or to shape them by 3D printing.

Aerogels are monolithic and porous materials structured from 3D solid networks that are made up of silica, (nano)carbons, polymers, oxides, semiconductors, metals, and so on.[107-109] From their light weight (density usually < 100 mg cm^{-3}), it is easily to deduce that a large amount of macropores exist in the network structure.[109] Along with the appearance of new building blocks such as semiconductors and metals,[110-111] it is potentially interesting to formatting microporous MOFs into aerogel form so as to attain macropores.[112-116] The first MOF aerogel is based on Fe-BTC, where the gelation has been observed after vigorous stirring of precursor solutions.[114] Purified with ethanol and dried by supercritical-state CO_2, the resulting MOF aerogels have manifested low densities (14.5–110.5 mg cm^{-3}), broad PSDs, and a remarkably high pore volume (up to 5.62 cm^3 g^{-1}). A deep understanding of the gelation mechanism for MOFs has been delivered by a later work based on Al-BDC aerogels.[116] As shown in **Figure 7g**, in the first step, a strong metal-ligand coordination (*i.e.*, Al-O bonds) promotes the formation of small MOF particles (MOFPs) as nuclei (*i.e.*, the nucleation stage); then owing to a reduced concentration of precursors along with reactions, the nucleation process is gradually replaced by the assembly process, where crystalline MOFs will form if directional growth is favored (*i.e.*, the crystal growth) while non-ordered gels will generate if the coordination equilibria are disturbed by other competing interactions. On this basis, an elevated temperature (353 K) has been adopted to suppress crystal growth and promote gel formation, eventually yielding Al-BDC aerogels with pore size of up to ~90 nm as measured by nitrogen sorption test.

On the other hand, as an emerging technique appearing in last few decades, 3D printing brings hope to create complex macroscopic architectures of desirable compositions. However, to obtain an ink with suitable rheological properties, specific additives are inevitably involved and may permanently incorporated in the final MOF products.[117-119] For example, anionic 2,2,6,6-tetramethylpiperidine-1-oxylradicalmediated oxidized cellulose nanofibers (TOCNFs) have been used as carriers, where ZIF-8 has been anchored on it by successively addition of zinc salts, triethylamine, and 2-MIM solutions, thus yielding hybrid inks.[118] It is also possible to incorporate a model of anticancer drug (*i.e.*, curcumin) into inks before 3D-printing. As shown in **Figure 7h-k**, both inks can be 3D-printed to form monoliths with macropores that can be resolved by naked eyes.

2.3. Pore architecturing for MOF-derivatives

MOF-derivatives are obtained from pristine MOFs by suitable treatment. By selecting suitable MOF precursors and controlling processing parameters, a variety of porous materials partially inheriting attributes of MOFs and typically with enhanced electrical conductivity can be obtained, including metal oxides (MO_x), metal sulfides (MS_x), metal selenides (MSe_x), metal phosphides (MP_x), metal nitrides (MN_x), their composites with carbon, pure carbon, and metal hydroxides ($M(OH)_x$). As schematically illustrated in **Figure 8**, the pore architecturing methods for these MOF-derivatives can be roughly divided into pore chemistry (diverse chemical compositions) and pore structure design (various pore volumes, SSAs, dimensions, and complicated architectures) similar to that for pristine MOFs. Typical synthesis strategies are summarized in **Table 2**. In the following, the pore chemistry/structure design will be separately introduced.

2.3.1. Pore chemistry design

In this section, we will review typical solutions to fabricate MOF-derivatives of various kinds. For certain well-studied MOF-derivatives (e.g., porous carbons and metal oxides), in-depth chemistry design will be elaborated.

The majority of MOF-derived materials are created by controlled annealing specific MOF precursors, and both the type of precursors and the processing parameters are of paramount importance. Basically, annealing in air usually causes the total decomposition of organic ligands, resulting in the porous metal oxides (MO_x).[120-130] For example, porous NiO nanoparticles have been fabricated by annealing a $Ni_3(HCOO)_6$ MOF at 400 °C in air.[131] To expand the kinds of metals, MOFs can be pre-modified before annealing. Guan *et al.* have fabricated porous $NiCo_2O_4$ via a two-step process, *i.e.*, 1) conversion of 2D Co-MOF (*i.e.*, Co-2-MIM) to Ni–Co layered double-hydroxide (denoted as Ni – Co LDH) with $Ni(NO_3)_2$ solution through a hydrolysis-controlled ion-exchange and etching process, and 2) annealing at 350 °C in air.[27] In another study, MIL-101(Cr) has been impregnated with $RuCl_3$ solution before annealing at 450–650 °C in air, yielding rutile $Cr_{0.6}Ru_{0.4}O_2$ with superior oxygen evolution reaction activity.[125]

In comparison, a non-air atmosphere can convert ligands to carbon, producing either porous carbon,[26, 132-141] MO_x/carbon (MO_x/C),[28, 142-148] or metal/C,[31, 149] depending on the properties of precursors and reaction conditions. By pyrolysis of a Zn-MOF derived from zinc salts and boron- and nitrogen-containing ligands at 900–1100°C in 5% H_2-Ar mixed atmosphere, zinc has been thermally reduced and evaporated, leaving behind porous B,N dual-doped carbon with a SSA of up to 1348 m^2 g^{-1}.[133] However, most MOF-derived carbon requires a post-acid-etching step, so as to fully removed metal residuals (**Figure 9a** shows an example for preparing ZIF-67-derived porous carbon).[26, 132] It needs to mention that the pyrolysis condition is critical for determining the composition of resulting porous carbon. To realize nitrogen doping, a Mn-

BDC MOF has been annealed in ammonia atmosphere following by acid treatment, yielding N-doped porous carbon (NPC).[134] By modulation of pyrolysis temperature from 500 to 700°C, the content of pyridinic N in the NPC can be tailored, achieving a maximized value of 5.32 at.% for NPC-600 (**Figure 9b**).[132]

Starting from Mn-BTC, MnO@C microspheres have been obtained by pyrolysis at 570°C in Ar for 2 h (**Figures 9c & 9d**).[144] Similarly, MFe_2O_4/C (M = Zn, Mn, Co, Ni) spindles have been produced from appropriate bimetallic MOF precursors, where the MFe_2O_4 NPs have been wrapped by thin carbon shells.[28] In another study, a metal–organophosphine framework prepared by linking copper with 1,3,5-triaza-7-phosphaadamantane has been synthesized as precursors, which has been then subjected to 600 °C treatment in nitrogen. Taking advantage of the co-existence of the σ-bond (bonding of lone pair electrons of P atoms to transition metals) and the π-backbonding (bonding of d-electrons of transition metals to empty d orbitals of P atoms) in the metal-P system, a carbon-microcuboid-supported phosphorus-coordinated single atomic copper has been obtained, showing an impressively high loading of copper (26.3 wt.%).[31]

To further expand the territory of MOF-derived materials, new strategies are required and additional sources need to be introduced during processing. $M(OH)_x$ are often obtained by treating with alkaline solutions either at room temperature or under hydrothermal conditions.[150-151] For example, surface-mounted Ni/Co-BDC MOFs have been transformed into the corresponding hydroxides by immersing in 0.1 M KOH aqueous solution.[151] As shown in **Figures 9e & 9f**, By mixing Ni/Co-based MOF-74 with 2 M KOH aqueous solution under hydrothermal condition (120°C for 2 h), the corresponding double hydroxides have been yielded.[150]

Generally, MS_x-based materials have been obtained via either annealing or solvothermal processing with sulfur sources,[29, 152] while MP_x-based materials have been acquired mainly by

annealing with phosphorous sources.[152-155] Starting from a NiCo-MOF-74, bimetallic oxide $NiCo_2O_4$ has been firstly obtained via calcination in air, then the metal sulfides ($NiCo_2S_4$) and phosphides (CoNiP) have been obtained by solvothermal reaction with thiourea at 180°C (*i.e.*, sulfuration process) and co-annealing with $NaH_2PO_2 \cdot H_2O$ at 300°C in Ar (*i.e.*, phosphatization process), respectively.[152] A recent study has shown that the carbonization of a Co-MOF and sulfur powder at 550 °C in N_2 can facilely yield hollow spheres made up of thin-carbon-layer-coated CoS_2 NPs in one step.[29] By introduction of phosphorous sources (sodium phosphate) through a hydrothermal process, a high-SSA metal phosphates (SSA of 142.2 $m^2 g^{-1}$) have been acquired resulting from substituting BTC ligands with the phosphoric ions. Recently, MOF-derived MSe_x/C material has also been demonstrated.[30, 156] As shown in **Figure 9g & 9h**, NiSe@C hollow microspheres have been acquired by 1) transforming Ni-MOF to NiO@C and 2) selenidation with Se powder through sequential hydrothermal reaction and high-temperature annealing.[30] The resulting materials display a high SSA of 64.8 $m^2 g^{-1}$ and an average pore size of 46.3 nm, showing good potential for sodium-ion storage.

2.3.2. Pore structure design

Relying on the morphologies of MOF precursors, fabrication tactics, and processing parameters, pore structures of MOF-derived materials can be versatilely tailored. This section will delineate this topic from the perspective of PSD & SSA, dimensions of microstructures, and complex architectures, all of which can directly or indirectly influence pore structures.

Pore size distribution & specific surface area

PSD and SSA are usually coupled together, hence the modulation of them will be introduced together here. The manipulation strategies can be mainly grouped in three categories, *i.e.*, annealing temperature control, chemical activation/etching, and templating.

As mentioned before, controlled annealing is the most widely adopted method of preparing MOF derivatives, where the processing temperature plays the most crucial role in determining the pore structure of products. A high annealing temperature is beneficial for sufficiently decomposing MOFs to yield ordered graphitic carbon with outstanding electrical conductivity, while the original pore structure may collapse and metal compounds tend to severely aggregate, leading to a low SSA.[35] An Al-MOF has been converted into carbon nanosheets by pyrolysis (600–1000°C in Ar) followed by acid treatment. With increasing pyrolysis temperature, the SSA firstly increased from 1321.0 to 1571.4 m^2 g^{-1} (600–700°C), then decreased to 465.1 m^2 g^{-1} (at 1000°C).[157] The same phenomenon has been observed for ZIF-8-derived nitrogen-doped porous carbons, where the largest SSA (>600 m^2 g^{-1}) has been realized at a pyrolysis temperature of 700°C.[140] The considerable low SSA for the sample derived at 600°C (349.9 m^2 g^{-1}) can be attributed to the less well developed pores as a result of insufficient decomposition. Slightly different from porous carbons, the SSA for MOF-derived metal oxides monotonically decrease with increasing annealing temperature. For example, by calcinating $Sn_m[Fe(CN)_6]_n$ in air, the yielded $Sn_{0.72}Fe_{0.28}O_2$ displays decreasing SSA (108.6 to 51.6 m^2 g^{-1}) with increasing calcination temperature (350 to 650°C).[123] This has been assigned to the conversion of small to large pores (4 to 11 nm) as well as the aggregation of metal oxides.

Aside from tuning annealing temperature, additional chemical activation has also been employed to promote SSA and porosity. As shown in a recent study, a porous carbon has been firstly produced from a Cu-BIB (BIB = 1,4-bis(2-methyl-imidazol-1-yl)butane) MOF by sequential pyrolysis and HCl etching, then has been converted into activated porous carbon nanosheets by KOH activation (800°C under N_2).[158] After activation, the resulting material

featured abundant pores and amorphous structures, displaying ultrahigh SSA and substantial pore volume (2491 m^2 g^{-1} and 1.50 cm^3 g^{-1}) which are desirable for supercapacitors.

Compared to structure-ordered MOFs, their derivatives typically hold uncontrolled pore size distribution across micro-, meso-, and macroscales due to the influence of drastic preparation conditions. It is challenging to realize accurate control over PSD. In spite of the mentioned difficulties, certain success has been realized in modulating macropores of MOF-derivatives by designing the pore size of MOF precursors. Here, two strategies have been developed, *i.e.*, templating and defect engineering. Similar to the report discussed before,[106] monodispersed PS spheres have been applied as templates to tailor macroporous structure of single-crystal MOFs (ZIF-8[159] or HKUST-1[160]). MOF-derived carbons are further achieved with size-tailored macropores after removal of PS templates, high-temperature annealing (at 800–900°C in Ar), and elimination of metal residuals. The well-ordered large pores in those porous carbons can provide abundant mass transfer channels, strongly enhancing the performance for electrochemical energy storage. In another study, the as-prepared Co–Co Prussian blue analogue (PBA) solid microcubes have been firstly converted to MOF microframes by treatment with ammonia solution based on the complexation between NH$_3$ and Co^{2+}, then to Co$_3$O$_4$ microframes by calcination in air at 600°C. As schemed in **Figure 10a**, the eight corners of microcubes have been preferentially etched and the etching process proceeds along the diagonal direction, eventually producing macropores whose size increases with prolonged etching time. In comparison with solid-state Co$_3$O$_4$ microcubes, the resulting Co$_3$O$_4$ microframes display higher SSA and pore volume (26 m^2 g^{-1} and 0.15 cm^3 g^{-1} *vs.* 9 m^2 g^{-1} and 0.12 cm^3 g^{-1}) as reflected by nitrogen adsorption isotherms (**Figure 10b & 10c**).

Dimensions

Designing the dimension of microstructures provides another route to indirectly tune the pore structure of MOF-derived materials.

On the one hand, the microscopic dimension of MOF precursors has been tailored before converting to their derivatives. Zhao *et al.* have reported confinement growth of ultrathin Zn(bim)(OAc) MOF nanosheets (UT-Zn(bim)(OAc)) by introducing hydrophilic gluconate, whose long chains can inhibit crystal growth that is perpendicular to the crystal plane.[161] After annealing, ultrathin carbon nanosheets have been obtained with a thickness of ~2.5 nm, manifesting a much higher SSA compared to that of porous carbon derived from the bulk MOF (1834 *vs.* 1098 m^2 g^{-1}). Similarly, planar growth of MOFs has been achieved by adding a monodentate ligand — sodium benzoate — as termination agent during synthesis, yielding 2D Mn-MOFs with a thickness of ~ 4.5 nm.[134] Subsequent pyrolysis in ammonia and acid cleaning has given rise to Na and Mn components/N-rich carbon foils (MNC-1) and nitrogen-doped carbon foils (NC-1), respectively (**Figure 10d**). The rich meso- and macropores in NC-1, which comes from the vacancies left by metal components etched away through acid treatment, lead to a SSA of up to 417.8 m^2 g^{-1} (**Figure10e**). In another study, a high-SSA cobalt-doped 2D nanoporous carbon nanosheets (thickness of ~3.5 nm, SSA of 896 m^2 g^{-1}) has been synthesized from pyrolyzing ultrathin ZIF-67 nanosheets, where the latter has been pre-obtained by NaCl-template confinement growth.[162]

On the other hand, the generation of specific dimensions have been realized during the transformation from MOFs to their derivatives. Pachfule *et al.* have fabricated graphene nanoribbons by 1) controlled growth of rod-shape MOF-74 with salicylic acid as a modulator, 2) pyrolysis at 1000 °C to form 1D carbon nanorods, and 3) KOH treatment under ultrasonication followed by thermal activation to exfoliate nanorods into graphene nanoribbons (50–70 nm wide and 100–150 nm long).[163] In another interesting work, 1D N-doped carbon nanotube frameworks (NCNTFs) have been prepared by pyrolyzing ZIF-67 at 700°C in Ar/H2

atmosphere followed by acid cleaning.[26] During this process, H2 atmosphere can promote the formation of metallic Co NPs, which is known to catalytically decompose carbon to form 1D carbon nanotubes. The resulting NCNTFs feature high SSA and pore volume (513 m^2 g^{-1} and 1.16 cm^3 g^{-1}) as well as excellent electrical conductivity, thus showing impressive performance for oxygen evolution reaction. Very recently, 2D metal oxyhydroxide (MOOH) nanosheets have been derived from a metastable Co-doped Fe MOF by an electric-field assisted hydrolysis strategy.[164] Compared to simply treatment with alkaline solution (1 M KOH), application of an electric-field can facilitate transfer of charged hydrolyzed products (*i.e.*, ligands and metal complexes) and the OH^- anions, thus promoting the destruction of MOFs block to their 2D derivatives as fast as 20 seconds.

Complex architectures

Fabrication of complex architectures, particularly multi-shelled structures, offers a new avenue to modulate pore structure. Most studies focus on multi-shelled metal oxides.[120, 122, 165] As seen from **Figures 10f & 10g**, triple-shelled manganese–cobalt oxide hollow dodecahedra (Co/Mn-HD) have been produced by a continuous two-step calcination process with a Co/Mn-ZIF precursor.[120] In the first-step calcination at 270°C, metal oxide can gradually nucleate and grow at the outer surface while the inner ZIF shrink inward due to continuous decomposition, causing the separation of the rigid metal oxide outer shell and the inner part. Increase of temperature to 350°C can promote the further decomposition of inner ZIF, repeating the aforementioned process and eventually producing triple-shelled Co/Mn-HD. In another study, hetero-structured double-shelled nanoboxes (DSNBs) have been fabricated.[122] Firstly, as-synthesized ZIF-67 nanocubes have been transformed into ZIF-67/Co-Fe Prussian blue analogue yolk-shell nanocubes (PBA YSNCs) through an anion-exchange reaction with $[Fe(CN)_6]^{3-}$ ions. After annealing, those PBA YSNCs have been further converted into shell-

in-shell Co_3O_4/Co-Fe oxide, where Fe, Co, and O elements distributed in the outer shell while Co and O elements distributed in the inner box. Attributed to this double-shelled structure, a higher SSA (43.3 m^2 g^{-1}) compared to single-shelled nanocubes based on Co-Fe oxide and Co_3O_4 (32.1 and 10.7 m^2 g^{-1}) has been obtained.

3. Applications for Supercapacitors

Thanks to the unique structure and diverse chemistry for MOF-based materials, as well as increasing demand for energy management ranging from portable electronics, electrical vehicles, to grid applications, there is a spurt of tailoring neat MOFs and MOF-derived materials for EES in the last decade (**Figure 1**). As elaborated in introduction part, supercapacitors and metal-ion batteries (*e.g.*, LIBs, SIBs, and PIBs) contribute to the majority part of EES devices, in which MOF-based materials can play pivotal roles (**Figure 11**).

Supercapacitors store electricity in the form of electrostatic energy dominantly by rapid physically adsorption of opposite-charged ions (for pure EDLC), though accompanying with surface reversible redox reactions in certain scenarios (for pseudocapacitance). Therefore, these usually feature high power density and cycling stability. To determine the specific capacitance, both three-electrode and two-electrode methods have been adopted. In short, a three-electrode system is conducted through a working electrode and a counter electrode, where only the former is analyzed and the capacitance of the latter is not evaluated. In contrast, the two-electrode system, which is more approaching the practical use, is usually assembled from two symmetric working electrodes in series. Generally, three-electrode measurements yield values approximately doubling that of two-electrode measurements because of the different potential range experienced by a single electrode.[166]

Despite a quick charge/discharge process and outstanding cycling/rate performance (high power density & high stability) resulting from rapid physical process and surface-based reactions, the bottle neck of supercapacitors lies in a relatively low energy density. For EDLC, a linear increase of voltage upon charging/discharging leads to a triangular shape of a galvanostatic charge/discharge curve (*i.e.*, *U-t* curve), thus cutting the energy to half as given by:

$$E = 1/2 \times CU^2 \quad (2)$$

Where E, C, and U denote energy, capacitance, and voltage window, respectively.[167] Hence, to boost the energy density, a large specific capacitance and a wide potential window (*e.g.*, by using high-voltage organic electrolytes) are preferred. However, the use of organic electrolytes will lead to a low ionic conductivity, compromising the specific capacitance and rate performance.

So far, the supercapacitor performance for MOF-based materials is evaluated predominantly in aqueous solutions with a three-electrode configuration. Hence, in this section, the test conditions will not be detailed if the measurements are performed in this way. It needs to mention that aside from the EDLC mechanism, many MOF-based supercapacitors also involve pseudocapacitance due to the reversible valance change of metals as deduced from their very high measured capacitance. Here, we will focus on how the pore chemistry (element compositions, electrical conductivity, chemical environments, *etc.*) and structures (pore volume, PSD, SSAs, geometries, *etc.*) of MOF-based materials affect their supercapacitor performance. Note that the dimension and morphology effects are also classified in the pore structure subsections, because they can influence the meso-/macro- porosities to some extent though it is hard to quantify. Because pore environment/structures of MOFs and their derivatives are quite different, they will be delineated separately.

3.1. MOFs

MOFs are known for their large SSAs, abundant surface-active sites (both metals and ligands), and high porosities, which simultaneously offer substantial EDL/pseudocapacitance and rapid mass transfer channels. However, the first reported MOF-based electrode (*i.e.*, Co8-MOF-5, $Zn_{3.68}Co_{0.32}O(BDC)_3(DEF)_{0.75}$ with a SSA of 2900 m^2 g^{-1}) has delivered an extremely low specific capacitance of only 0.3 F g^{-1} at 0.01 A g^{-1} (0.1 M tetrabutylammonium hexafluorophosphate in acetonitrile).[20] The main issues can be associated with its low electrical conductivity and inappropriate PSD. Subsequent efforts have greatly improved the supercapacitor performance of MOFs by versatile design, which will be presented below from aspects of pore chemistry/structure engineering.

3.1.1. Engineering of pore chemistry

A considerable part of capacitance of MOFs can be associated with the Faradic process. For instance, the capacitance value of MOFs (see **Table 3**) is typically much larger than that of carbon materials (< 180 F g^{-1} in aqueous solutions), even though their SSAs are at a similar level. Therefore, tailoring the chemical nature of MOFs is a feasible way of modulating their performance. The supercapacitor performance of 23 MOFs has been compared, suggesting the non-negligible influence of the chemical nature.[168] For example, mixing of more than three metals in MOFs (*e.g.*, $Co_{0.54}Mg_{0.27}Ni_{0.60}Zn_{0.34}Mn_{0.35}(DOT)$, DOT = 2,5-dihydroxy-1,4-benzenedicarboxylate) has delivered an apparently better performance than that of single-metal $Co_2(DOT)$ MOFs (*ca.* 0.095 *vs.* 0.049 F cm^{-3} at 1 mA cm^{-3}), which is attributed to more significant redox reactions for the multi-metallic MOFs.

A critical challenge encountered by MOF-based supercapacitors resides in the low electrical conductivity of MOFs, which leads to a large resistance that causes serious energy loss (from a

36

large *iR* drop) and poor rate performance. Therefore, most studies have fabricated electrodes by mixing MOFs with a considerable amount of conductive additives (typically 15−30% acetylene black or Super P[169-170]), raising the cost and decreasing device-based gravimetric capacitance. To address this issue, some recent studies have devoted to promoting conductivity of MOFs by designing highly-conjugated backbones.[53-54, 171] As initiated by Dincă's group in 2017, a highly conductive MOF $Ni_3(HITP)_2$ (bulk conductivity > 5000 S m^{-1}), which is made up of stacked π-conjugated 2D layers that are penetrated by 1D cylindrical channels (**Figure 12a**), has been applied as neat electrode materials.[54] The measurement has been performed with a two-electrode configuration in a tetraethylammonium tetrafluoroborate/acetonitrile system. The cyclic voltammetry (CV) curves show a rectangular shape featured by EDL capacitive behavior, and a capacitance of 111 to 15 F g^{-1} (current densities from 0.05 to 10 A g^{-1}) has been observed (**Figure 12b-c**). Additionally, a high areal capacitance (18 F cm^{-2} @ 0.05 A g^{-1}) and good cycling performance (90% @ 10000 cycles) have been obtained. To further boost the capacitance by enlarging the portion of pseudocapacitance, Bao's group coordinated ultrasmall hexaaminobenzene (HAB) ligands with metal centers, producing conductive and highly dense frameworks (conductivity ~70 S m^{-1} for Ni-HAB).[53] Attributed to the high-density redox-active HAB ligands, clear redox peaks have been identified and a high gravimetric capacitance of 420 F g^{-1} for Ni-HAB has been obtained at 1 mV s^{-1}. Additionally, the freestanding additive-free Ni-HAB pellets showcase outstanding areal- and volumetric capacitance (17 F cm^{-2} and 460 F cm^{-3} for a 360 μm-thick pellet), rivaling the best-performing carbon or transition metal oxide electrodes.

Besides low electrical conductivity, another concern is related to the poor stability of MOFs during operation. Three1,4-diazabicyclo[2.2.2]octane (DABCO) pillared nickel-based MOFs (*i.e.*, Ni-DMOFs) have been synthesized with different in-plane carboxylate linkers (*i.e.*, 2,3,5,6-tetramethyl-1,4-benzenedicarboxylic acid (TM), 1,4-naphthalene-dicarboxylic acid

(NDC), and 9,10-anthracenedicarboxylic acid (ADC)) (**Figure 12d**).[172] Both TM- and ADC-based MOFs show excellent water stability due to their less polarity compared to NDC-based MOFs. Particularly, presumably due to a more conjugated structure for ADC, the Ni-DMOF-ADC exhibit the best performance, featuring both excellent rate performance (552 to 395 F g^{-1} @ 1–50 A g^{-1}) and remarkable cycling stability (98% retention after 15000 cycles) (**Figure 12e-f**).

3.1.2. Engineering of pore structures

Specific surface area

The specific surface area is one of the major parameters that is closely related to the pore structure and the supercapacitor performance of MOFs. While a large SSA can offer abundant accessible sites for charge storage, it may deteriorate the stability particularly for pseudocapacitance-dominated MOFs. For example, Zr-BDC MOFs with different SSAs (596–1047 m^2 g^{-1}) have been prepared by solvothermal treatment at different temperatures (50–110 °C).[169] A positive correlation between SSAs and specific capacitance (from 207 to 1144 F g^{-1} at 5 mV s^{-1} with increasing SSAs) has been found, while the best-performing electrode suffers from a poor rate performance (~32% capacitance retention at 50 mV s^{-1}) and a low cycling stability (~71.8% after 2000 cycles). By controlling the solvent composition during synthesis, several Co-BTC MOFs with various SSAs have been obtained, where the N,N-dimethylformamide (DMF)/ethanol system has yielded MOFs (*i.e.*, Co-MOF/D-E) with the highest SSAs (31.98 m^2 g^{-1} *vs.* <6 m^2 g^{-1} for others).[173] As expected, the Co-MOF/D-E manifests the best performance, holding a high specific capacitance of 958 F g^{-1} at 2 A g^{-1} (retained ~627 F g^{-1} even at 30 A g^{-1}) as well as a good cycling performance (92.3% retention after 3000 cycles). In another study, by lengthening the size of linkers (from short BDC, NDC

to BPDC), Co-MOFs with different morphologies and increasing SSAs (from 9.09 to 138.35 m^2 g^{-1}) have been obtained (**Figure 13a-c**), leading to enhanced specific capacitance (131.8 to 179.2 F g^{-1}) and reduced stability (77.4 *vs.* <6% retention after 1000 cycles, see **Figure 13d**).[174]

Pore size distribution

Aside from SSAs, the PSD serves as another critical parameter that substantially affects the performance.[170, 175-177] From the previous experience,[20] MOFs with dominant micropores are not suitable for high-performance charge storage because of retarded mass transfer. An indium-based mesoporous MOF (*i.e.*, 437-MOF) has been used for investigation.[176] With 4,4',4"-[benzene-1,3,5-triyl-tris(oxy)]tribenzoic acid (H_3BTTB) as ligands, the coordination framework features regular 1D hexagonal channels (diameter ~3 nm) (**Figure 13e-f**). After treatment in boiling water, ordered channel-like morphologies have been observed (**Figure 13g**). Though with an increase of pore volume/SSA from 0.92 cm^3 g^{-1}/1576 m^2 g^{-1} to 1.11 cm^3 g^{-1}/2379 m^2 g^{-1} and a good cyclability, the specific capacitance (150.2 @ 0.2 A g^{-1}) is still not satisfactory (**Figure 13h**). In another study, hierarchically porous UiO-66 (HP-UiO-66) prepared by etching MOF-5 from UiO-66/MOF-5 composite showcase broad PSD (1−40 nm, total volume (V_{tot}) and microporous volume (V_{micro}) are 1.08 and 0.35 cm^3 g^{-1}, respectively).[170] On this basis, a high capacitance of 849 F g^{-1} at 0.2 A g^{-1} has been obtained. Another interesting work has shown that doping zinc into a Ni-PTA MOF (PTA = p-benzenedicarboxylate) can enlarge the interlayer distance (from 0.95 to 1.04 nm), thus facilitating ion diffusion and boosting the performance (*ca.* 1620 *vs.* 1250 F g^{-1} @ 0.25 A g^{-1}, and 92% *vs.* 66% retention after 3000 cycles for Zn-doped and pristine Ni-PTA).[177]

Dimensions and morphologies

In addition to apparent pore parameters, microscopic dimensions and morphologies can also largely influence the device performance by modulating the ion diffusion distances. 1D Ni-based MOF nanorods ($Ni(HOC_6H_4COO)_{1.48}(OH)_{0.52} \cdot 1.1H_2O$) has been pioneered by Xu *et al.*[178] With a moderate SSA (~186 m^2 g^{-1}) and mesopores (~3.2 nm), a remarkable specific capacitance of 1698 F g^{-1} has been obtained at 1 A g^{-1} presumably due to its large pseudocapacitance. In addition, the rate and cycling performance are also excellent (49.4% @ 10 A g^{-1}, and 94.8% @ 1000 cycles). Meanwhile, 2D MOFs nanosheets (NSs) have also attracted wide attention. The first 2D Ni-based MOF NSs have been prepared by using PTA as linkers.[179] Featuring parallel-stacked 2D NSs (thickness of ~10 nm), efficient 2D ion transfer has been enabled, highlighting an excellent rate performance (1127/668 F g^{-1} at 0.5/10 A g^{-1}) and cycling performance (>90% after 3000 cycles). In comparison with Ni-based MOFs, Co-based MOF NSs have been more frequently applied probably due to their pronounced pseudocapacitance.[180-182] Although the first reported layered Co-based MOF (*i.e.*, Co−LMOF) holds a very high specific capacitance (2474 F g^{-1} @ 0.5 A g^{-1}),[182] the claimed 2D structure has been hard to be identified from electron microscopy. By adopting BDC as linkers and polyvinylpyrrolidone (PVP) as shape-directing agents, ultrathin Co-BDC NSs (thickness ~2 nm) have been obtained.[180] Due to largely shortened ion diffusion distances, an impressive rate performance has been observed, where 90.8% capacitance (1052 F g^{-1}) has been reserved by raising current density from 0.5 to 5 A g^{-1}. In a recent work, a record-high specific capacitance of 2564 at 1 A g^{-1} has been reported on a new-type 2D MOF NSs ($Co_2(OH)_2C_8H_4O_4$, thickness of 5−10 nm).[181] The ultrahigh performance has been attributed to a combination of a layer structure, conductive networks frames (conductivity of 0.375 S m^{-1}), and pseudocapacitance provided by cobalt species.

Beyond single dimension, complex nano-architectures hosting hybrid dimensions have been proven to exhibit striking properties.[183] Such hybrid-dimension-design has also been explored for MOF-based supercapacitors,[51-52, 177, 184] because it is feasible to facilitate ion transport by reducing charge-transfer resistance and shorter diffusion pathways. An early work has prepared a Co-oxalate MOF, which shows a 3D network-like microstructures assembled from 2D nanoflake arrays.[52] The specific capacitance has been measured to be 703 F g^{-1} at 1 A g^{-1} and retained 87% at 10 A g^{-1}. Afterwards, a 3D accordion-like Ni MOF assembled from 2D NSs (thickness <6 nm, see **Figure 13i**) has been reported.[184] The resulting 2D/3D hybrid dimensional MOFs possess a low charge-transfer resistance (6.3 Ω), enabling their high rate performance (1021 F g^{-1} @ 0.7 A g^{-1} and 823 F g^{-1} @ 7 A g^{-1}) and good cyclability (96.5% @ 5000 cycles). Very recently, a gear-like layered Ni-TDA (TDA = 2,5-thiophenedicarboxylate) MOF has been demonstrated, showing high specific capacity (1518.8 @ 1 A g^{-1}), outstanding cyclability (95.5% @ 10000 cycles), and compatibility for integration in flexible EES devices (**Figure 13j-l**).[51]

3.2. MOF-derivatives

In comparison with pristine MOFs, the electrical conductivity of their derivatives can be considerably increased during the conversion process. In addition, by selecting appropriate MOF precursors and controlling the processing parameters, a wide spectrum of MOF-derived materials with desirable composition and pore structures can be obtained. All these features allow MOF-derivatives for promising supercapacitor electrodes. After the first example reported in 2010 — porous carbon derived by directly decomposing MOF-5[185] — quite a few MOF-derivatives in the form of neat carbons, metal oxides, metal sulfides, and so on have been investigated. In the following, tailoring supercapacitor performance of MOF-derivatives will be separately discussed by devising their pore chemistry and structure.

3.2.1. Engineering of pore chemistry

Modulating pore chemistry can not only enhance the electrical conductivity for enhancing power density, but also introducing pseudo-capacitance to achieve high energy density. Generally, MOF-derived porous carbons can attain a quite high electrical conductivity, while MOF-derived metal-containing species feature large pseudo-capacitance owing to the Faradic-process involved in the charge-discharge process.

Carbon

By pyrolysis of a lamellar Cu-MOF following by acid etching and KOH activation, porous carbon nanosheets have been obtained.[158] The obtained porous carbon with built-in oxygen-containing functional groups shows excellent electrical conductivity, which has been reflected by very small charge equivalent series resistance ($< 1 \, \Omega$). As a result, a high specific capacitance of $260.5 \, F \, g^{-1}$ at $0.5 \, A \, g^{-1}$ has been obtained. Particularly, integrating such porous carbon into symmetric two-electrode supercapacitor has given rise to impressive energy density (11.43–18.38 Wh kg^{-1}) and power density (350–6881 W kg^{-1}), greatly surpassing commercial activated carbon (1.45 Wh kg^{-1}).

Metal oxides

Besides porous carbons, metal oxides are another class of MOF-derived materials frequently used for supercapacitors due to their reversible reactions during operation (*i.e.*, pseudo-capacitance). For example, a Ni-MOF (($Ni_3(HCOO)_6$) with regular polyhedral shape (size of 0.5–1 μm, SSA of 34 m^2 g^{-1}) has displayed a reversible capacitance of $324 \, F \, g^{-1}$ at $1 \, A \, g^{-1}$ and has sustained 46% of this capacitance with a current density of $40 \, A \, g^{-1}$.[131] The surface

oxidation/reduction reactions of Ni^{2+} and Ni^{3+} contribute to additional capacitance as reflected from the redox peaks in CV curves. Besides single-metallic oxides, multi-metallic oxides have also been explored for the enhanced performance. As shown in **Figures 14a-b**, MOF-74 based on neat Ni, Co, and Ni-Co mixture have been employed as precursors, yielding the porous NiO, Co_3O_4, and $NiCo_2O_4$, respectively.[186] Although bimetallic oxides feature only a moderate SSA (59.6 m^2 g^{-1} for $NiCo_2O_4$, 227.5 m^2 g^{-1} for NiO, and 48.9 m^2 g^{-1} for Co_3O_4), a considerable increase in specific capacitance has been observed (684 F g^{-1} for $NiCo_2O_4$, 105 F g^{-1} for NiO, and 181.5 F g^{-1} for Co_3O_4 at 0.5 A g^{-1}) and a capacitance of 362.4 F g^{-1} has been sustained at 10 A g^{-1}. The enhanced performance may be attributed to the co-existence of multiple charge-storage mechanisms shown in the $NiCo_2O_4$, highlighting the importance of synergistic effect of multiple metals. Aside from performance enhancement, it is also feasible to save the cost by replacing expensive cobalt with other metals. For an instance, porous ZnO/NiO microspheres have been prepared by calcinating cost-effective Zn/Ni-MOF ([ZnNi(BTC)(NO_3(1.6 H_2O)](0.4 DMF)).[187] However, in spite of a relatively high SSA (170 m^2 g^{-1}), the obtained ZnO/NiO microspheres only have delivered a moderate specific capacitance (172.9 F g^{-1} at 0.5 A g^{-1}).

Other MOF-derived materials

Recently, efforts have also been made to produce other types of porous materials from MOFs for supercapacitor application. A typical example is the use of metal double hydroxides (MDH) derived by treating MOFs with potassium hydroxide.[150] By modulating the ratio of nickel and cobalt, a series of MOF-74 have been produced and then converted to the corresponding MDH (X-Ni-MDH, X denotes the percentage of Ni in MOF-74). As demonstrated in **Figures 14c-d**, the optimized formula (*i.e.*, 65Ni-MDH with 65% Ni and 35% Co) outperforms MDH with all other compositions, featuring outstanding specific capacitance and rate performance (875 and 666 C g^{-1} (*i.e.*, 1750–1332 F g^{-1} at 1–20 A g^{-1}) as well as excellent long-term stability (90.1%

retention after 5000 cycles). The assembled 65Ni-MDH//N-doped porous carbon hybrid supercapacitor has delivered a high energy density of 81 W h kg^{-1} at a power density of 1.9 kW kg^{-1} and maintained 42 W h kg^{-1} at 11.5 kW kg^{-1}, outlining its profound practical values.

In another study, hollow porous nickel phosphates are derived from Ni-BTC. By substitution of organic ligands (*i.e.*, BTC) with phosphoric ions, the derived Ni$_x$P$_y$O$_z$ has displayed a much higher capacitance with respect to the original Ni-MOF (1627 *vs.* 399.3 F g^{-1} at 1 A g^{-1}, see **Figure 14e**).[188] This is attributed not only to the increased SSA from 2.5 to 142.2 m^2 g^{-1} upon substitution, but also the enhanced electrical conductivity and ionic conductivity as reflected from the smaller equivalent series resistance and charge-transfer resistance from electrochemical impedance spectroscopy (EIS) measurements (**Figure 14f**). In a recent report, the supercapacitor performance is evaluated for binary transition metal oxides, phosphates, and sulfides derived from NiCo-MOF-74.[152] Interestingly, conversion of oxides (*i.e.*, NiCo-O) to the phosphates (NiCo-P) and sulfides (NiCo-S) induces nanoscale structural change: the three bimetallic species feature hollow tubular structures with loosely-packed particles, densely-packed particles, and nanoflakes, respectively. It is claimed that the unique nanoflake-assembled rough surface structure of NiCo-S is responsible for its better performance compared to the other two derivatives (930, 305, and 410 F g^{-1} at 1 A g^{-1} for NiCo-S, NiCo-O, and NiCo-P, respectively, see **Figure 14g**). However, the cycling performance of NiCo-S is moderate, with 70.5 % retention after 10000 cycles. As illustrated in **Figure 14h**, an asymmetric supercapacitor from the NiCo-S with activated carbon displays a maximum energy density of 22.6 W h kg^{-1} at a power density of 0.8 kW kg^{-1}.

3.2.2. Engineering of pore structures

In addition to modulating chemical compositions, it is also essential to tune the pore structure of MOF-derivatives so as to boost device performance. Generally, the control of pore structures

can be realized by tuning the SSA and pore size, controlling the dimension of microstructures, and constructing complicated microstructures.

Specific surface area

To introduce more active sites, a high SSA is paramount. A series of NiO nanospheres have been obtained by controlling the calcination temperature of Ni-BDC.[189] With increase of calcination temperature from 400 to 600 °C, the SSA decreased from 66.8 to 5.0 m^2 g^{-1} due to the increased crystalline size as reflected from the PXRD patterns (**Figure 15a**). As a result, the NiO with the highest SSA has shown the best specific capacitance (473 F g^{-1} at 0.5 A g^{-1}) and good rate performance (see **Figures 15b, 15c**).

Pore size distribution

To accelerate the mass diffusion, it is desirable to introduce macroporosities. A hierarchically interconnected macro-microporous carbon has been prepared by annealing of a single-crystalline ordered interconnected macro-microporous Cu-based MOF (denoted as SIM-HKUST-1).[160] Inheriting the structural attribute of SIM-HKUST-1, the derived hierarchically-porous carbon (denoted as IM-HPC, see **Figure 15d**) has shown smaller charge-transfer resistance compared to that for microporous carbon (denoted as MPC, see **Figure 15e**) derived from conventional HKUST. As a result, IM-HPC has harvested a considerably higher specific capacitance that for MPC across a wide current density (171–236 F g^{-1} *vs.* 75–128 F g^{-1}, see **Figure 15f**) and featured negligible capacitance retention after 10000 cycles.

Compared to the construction of neat macroporous MOF-derived materials, fabrication MOF-derivatives on 3D self-supported macroporous substrates (*i.e.*, the current collectors) can not only facilely introduce macroporosities, but also increase the areal density and/or the

mechanical flexibility that are beneficial for practical use.[27, 190] In a recent study, hollow and porous $NiCo_2O_4$ nanowall arrays have been prepared on a flexible carbon cloth (CC@$NiCo_2O_4$) by transforming a 2D cobalt-based MOF to Ni-Co layered double-hydroxide (LDH) following by calcination.[27] This design leads to a specific capacitance of as high as 1055.3 F g^{-1} at 2.5 mA cm^{-2}. Particularly, a solid-state asymmetric supercapacitor has been assembled by pairing CC@$NiCo_2O_4$ (as the cathode) with nitrogen-doped carbon flakes on carbon cloth (CC@NC, as the anode), which has delivered a maximum energy density of 31.9 W h kg^{-1} at a power density of 2.9 kW kg^{-1} as well as excellent tolerance towards mechanical bending/twisting.

Dimensions and morphologies

In the recent years, MOF-derived materials with well-defined dimensions or specific morphologies have been successfully developed, facilitating the control of the porous structures and boosting their performance.

A recent study has reported 1D bamboo-like carbon nitride (denoted as c-CN) derived from the decomposition of $Ni(HNCN)_2$.[191] With a rich nitrogen content and the catalytic activity of the built-in nickel, the Ni-MOF has been transformed into a highly N-doped (10.8 at.% nitrogen), 1D hollow tubular structure, sp^2-C (diameter of ~80 nm), by annealing at 850°C under vacuum following by removal of nickel with acid. The unique architecture of c-CN has concurrently endowed a high SSA (181.3 m^2 g^{-1}), a low macroscopic sheet resistance (~3.1 Ω sq^{-1}) and high-content redox-active nitrogen. Those features have facilitated high-rate electron/ion transfer and imparted additional pseudo-capacitance, leading to a gravimetric capacitance of 333.8 F g^{-1} (measured at 5 mV s^{-1} by CV) and an outstanding long-term stability (88.1% retention after 12000 cycles at 8 A g^{-1}).

Besides, 2D MOF-derived carbon nanosheets have also been studied. Ultrathin Zn(bim)(OAc) MOF (UT-Zn(bim)(OAc), bim = benzimidazole) nanosheets have been synthesized with the

assistance of hydrophilic gluconate, which have then been converted into ultrathin carbon nanosheets (UT-CNSs, thickness of 2.5 ± 0.8 nm, see **Figure 15g**).[161] In comparison with the bulk carbon nanocubes (CNCs) and layered carbon nanocubes (L-CNCs) derived from $Zn_2(bim)_4$ and $Zn(bim)(OAc)$, the dimension confinement of UT-CNSs has rendered much improved SSA (1836 m^2 g^{-1}), pore volume (1.92 cm^{-3} g^{-1}) and charge-transfer resistance (see **Figure 15h**). These features determine the outstanding performance of UT-CNSs as shown in **Figures 15i**, with a specific capacitance of 347 F g^{-1} at 0.5 A g^{-1} and 98.8% retention after 5000 cycles at 5 A g^{-1}. In another study, a potassium-based nanorod-like MOF ($\{K_3[C_6H_3(CO_2)(CO_2H_{0.5})(CO_2H)]_2\}(H_2O)_2$) has been used as precursor, yielding 2D nanoporous carbon sheets (denote as NPS-800) by a two-step annealing process.[192] The obtained hierarchically porous NPS-800 has shown a graphene-like layered structure yet with a small domain size (5–10 nm), featuring both high SSA and pore volume (1192 m^2 g^{-1} and 1.06 cm^{-3} g^{-1}). Although the gravimetric capacitance is moderate (238 F g^{-1} at a scan rate of 5 mV s^{-1} by a two-electrode measurement), an impressive areal capacitance of as high as 21.35 μF cm^{-2} has been obtained, outperforming the majority of other carbon-based supercapacitors.

Recently, MOF-derived materials with special architecture have also been designed for enhancing supercapacitor performance. Starting from solid Zn/Co-ZIF rhombic dodecahedron (size of 1.9 μm), double-shelled zinc–cobalt sulfide rhombic dodecahedral cages have been obtained with shell thickness of ~120 nm.[193] Compared to the single-shelled counterpart, the double-shelled structure has exhibited a much-enhanced capacitance (1266 *vs.* ~700 F g^{-1} at 1 A g^{-1}) presumably due to a higher fraction of active species as well as a better electrical contact. Moreover, an extraordinary cycling stability of 91% retention after 10000 cycles has been achieved. Another study also suggests the advantage of the hollow structure.[194] Compared to solid CoP microcubes, the hollow structure allows for reduced charge-transfer resistance due to facile ion transfer as well as abundant active sites, thus giving rise to excellent rate

performance (560–324 F g^{-1} at 1–20 A g^{-1}) and stability (91.2% capacity retention after 10000 cycles).

4. Applications for metal-ion batteries

Metal-ion batteries, particularly for those based on Li$^+$, Na$^+$ and K$^+$, provide a complementary way of storing electrochemical energy to supercapacitors thanks to their relatively high energy density. Upon operation, theoretically two electrodes (*i.e.*, anodes and cathodes) work at two stable potentials which is determined by the specific electrode reactions (intercalation reaction or conversion reaction), thus generating a plateau region in the galvanostatic charge/discharge curve (*U-t* diagram). The electrode reactions can go through the bulk materials instead of being limited at the surfaces, thus enabling to store much more energy than supercapacitors without the need of large SSAs. However, they usually suffer from low kinetics due to sluggish electrode reactions and slow mass transfer inside the bulk materials. Additionally, the initial Coulomb efficiency (discharge/charge in the first cycle) is much less than 100%, which is mainly attributed to the decomposition of electrolytes and the consumption of alkaline metals in the formation of solid electrolyte interface (SEI). This fact requires to introduce over-stoichiometric alkaline metals during battery assembly, decreasing the energy density and raising the cost. Moreover, a much lower cycling stability compared to supercapacitors is another common issue for batteries.

The investigations of MOFs and their derivatives for MIBs are initiated from the beginning of this century,[21-24] and acquire extensive attention particularly in the last decade. Both the mechanistic study and performance optimization have been extensively explored for their use as anode and cathode materials, while the investigation of MOF-based solid-state electrolytes is only at its infant stage.[45] Among these studies, it is not surprising that LIBs have received the most attention because of the mature operation procedures and equipment. Cost-effective

SIBs and PIBs have also attracted interest gradually, while the corresponding studies are few, particularly for neat MOFs. This can be attributed to the large atomic mass and ionic radius (0.76 Å for Li^+, 1.02 Å for Na^+, and 1.38 Å for K^+) as well as relatively positive redox potential (-3.04 V vs SHE for Li^+, -2.71 V vs. SHE for Na^+, and -2.93 V vs SHE for K^+) for sodium and potassium, which inevitably retard the reaction kinetics, cause large structural distortions, and reduce the energy/power density.

Because MOFs and their derivatives are marked by different physicochemical properties and energy storage mechanisms, here they will be introduced separately. To better demonstrate guidelines for material design, pore chemistry and pore structure modulation will be sequentially introduced.

4.1. MOFs for electrodes

The feasibility of using MOFs as cathodes (by MIL-53(Fe)) and as anodes (by MOF-177) have been firstly demonstrated in 2007 and 2006, respectively.[21-22] The cathodes are mostly constructed by Fe- or Cu- based MOFs, generally showing a pronounced plateau similar to electrodes made of other materials. The corresponding energy storage mechanism has been attributed to the solid-solution insertion/extraction of alkaline metal ions/electrolyte anions, two-phase transition, and reversible redox reactions of metal/ligand of MOFs.[22, 195-196] In contrast, MOFs based on versatile metals (*e.g.*, Al, Co, Li, Mn, Ni, Ti, and Zn) have been studied for anodes, where additional storage mechanisms such as the insertion/deinsertion of alkaline metal ions to the carboxyl groups and/or benzene rings of ligands have been proposed,[197-199] leading to the absence of discernable plateau in the charge/discharge curves. It should be noted that due to the specific configuration of MOF structures, the electrochemical stability depends on the intrinsic stability of the node, the linker and/or their interconnecting bonds. The voltage window may then be considerably influenced by the stability of MOF-based

electrodes. Because most of the metal elements in MOFs (*e.g.*, Zn, Cu, and Fe) are of relatively high redox potentials, compared with alkali metals (Li, Na, K), the MOF metals can transfer from their high to low oxidation state (even the zero-valence state) when MOFs are used in the anode. In contrast, when used in the cathode, the oxidation-induced decomposition of the organic ligands may occur depending on their electronic structures. Nonetheless, the redox-stability of the two components and their effect on the performance of the corresponding MOF materials have not been well investigated.

In general, the MOF-based cathodes show a much lower capacity than that for the MOF-based anodes (*e.g.*, *ca.* 60–150 *vs.* 200–1000 mAh g^{-1} for LIBs, see **Table 4**), similar to the occasion of conventional MIBs. For both electrodes, they display inferior rate performance and low coulomb efficiency (basically < 75%) presumably due to sluggish reaction kinetics, low electrical conductivity, and poor stability of MOFs. Nevertheless, the last decade witnessed various creative works that largely advance the development of MOF-based electrodes. In the following, typical examples for MOF-based cathode/anode electrodes for LIBs, SIBs, and PIBs will be introduced, highlighting the design from pore chemistry and pore structure aspects.

4.1.1. Engineering of pore chemistry

MOFs as cathodes for LIBs

The properties of both metal centers and linkers of MOFs are critical for modulating their performance as LIB cathodes. Férey *et al.* have demonstrated the first reversible MOF-based LIB cathode by using MIL-53 (Fe), which has been prepared by linking iron-based SBUs and BDC linkers.[22] It has been proposed that MOFs based on earlier (3d) transition metals (*e.g.*, Fe) feature a stable M−O bond upon charge variations due to the lower occupation of 3d-electron orbitals, thus allowing for reversible charge/discharge. By cycling between 1.5–3.5 V

vs. Li/Li^{+}, MIL-53(Fe) has reversibly incorporated ~0.6 Li per Fe and delivered a reversible capacity of 75 mAh g^{−1} at 0.1 C. MIL-68 (Fe) and MIL-101(Fe) have also been synthesized with the same linkers for LIB cathodes, by changing the reaction conditions (*e.g.*, reactants and temperatures).[200-202] It has been found that initial coulomb (CE) is *ca.* 79% and 0.35 Li per Fe can be inserted in MIL-68(Fe) at 0.1 C, corresponding to a low capacity (~30 mAh g^{−1}).[200] In the aforementioned studies, a well-defined charge voltage plateau (~3 V) and a relatively sloping discharge curve were observed. By optimizing processing conditions and performing charge/discharge at 2.0–4.2 V, a discharge capacity of *ca.* 72 mAh g^{−1} has been obtained for MIL-101(Fe) (~0.67 Li per Fe) after 100 cycles at 0.2 C.[202] However, the voltage plateau disappears in this work, which is in contradiction to another report for MIL-101(Fe)[201] and other Fe-based MOF cathodes.[22, 200]

Besides Fe-based MOFs, Cu-based MOFs have also been explored. In 2014, Cu(2,7-AQDC) (2,7-H$_2$AQDC = 2,7-anthraquinonedicarboxylic acid, see **Figure 16a**) has been synthesized as cathode materials,[195] for the first time the independent redox active sites on both metal and ligands have been imparted. As seen from **Figure 16b**, two isolated peaks at 3.1 and 2.4 V have been identified from CV curves, corresponding to the redox reactions of metal clusters (Cu(I)/Cu(II)) and anthraquinone groups, respectively. The additional energy storage mechanism has boosted the initial specific capacity of 147 mAh g^{−1}, which has been stabilized to ~105 mAh g^{−1} within 50 cycles (**Figure 16c**). However, the discernible plateau is absent for this material. In a follow-up work, Cu-TCA (H$_3$TCA = tricarboxytriphenyl amine) which holds both redox-active metal clusters (Cu^{+}/Cu^{2+}) and organic ligands (N/N[+]) has been designed, achieving a reversible capacity of *ca.* 60 mAh g^{−1} @ 0.5 C and a high discharge voltage plateau at ~4 V *vs.* Li/Li^{+}.[203] However, the initial CE is moderate (~75%) and cycling stability is relatively poor.

The insulative nature of most MOFs is detrimental to their use as electrode materials, and this is usually bypassed by including a large portion of conductive additives (20−70 wt.% carbon black [195, 200-201, 204]) in electrode preparation. This can not only add extra costs and reduce the device-based energy- and power density, but also affect the evaluation of intrinsic properties of MOFs because of potential capacity contribution from carbons. In this regard, application of intrinsically conductive MOFs as electrodes is highly desirable.[171, 205-206] A conductive 2D Cu-CuPC (CuPC = copper phthalocyanine) MOF has been synthesized with an electrical conductivity of 1.6×10^{-4} S m^{-1} (at 80ºC), manifesting reversible capacitance of ~60 mAh g^{-1} (@ 0.4 C within 2.0−4.4 V) and an excellent stability (87% @ 200 cycles).[205] Recently, 2D highly conductive Cu-HHTP MOF (HTTP = 2,3,6,7,10,11-hexahydroxytriphenylene, conductivity ~20 S m^{-1}) has been applied for LIB cathode, delivering outstanding rate performance (~95 mAh g^{-1} @ 1 C and ~86 mAh g^{-1} @ 20 C within 1.7−3.5 V) yet a poor cyclability (~50% @ 500 cycles).[206] Additionally, it is worth noting that quite low initial CE ($< 70\%$) has been obtained for the aforementioned two examples, which might be attributed to their high SSAs (> 300 m^2 g^{-1}).

MOFs as cathodes for SIBs & PIBs

The study for MOFs as cathodes for sodium- and potassium-ion batteries are mostly concentrated on Prussian blue (PB) and its analogues. This might be started from an early report in 2004, where PB has been tested as rechargeable PIB cathode in 1 M KBF$_4$ in 3:7 EC/EMC (EC = ethylene carbonate, EMC = ethylmethyl carbonate).[23] At a rate of 0.1 C within *ca.* 2.6–4.1 V (voltage plateau at ~3.7 V), a specific capacity of ~78 mAh g^{-1} has been achieved and only a 12% capacity fade has been observed after 500 cycles. Afterwards, Cui's group has investigated both SIB and PIB (in 1 M NaNO$_3$ or 1 M KNO$_3$ aqueous solutions) performance by using Ni-hexacyanoferrate (HCF) and Cu-HCF electrodes.[24, 207] Ni-HCF has delivered similar capacity for SIB and PIB (~58 mAh g^{-1} @ 0.83 C and ~39 mAh g^{-1} @ 41.7 C), while

Cu-HCF has performed much better in PIB (~58 mAh g^{-1} @ 0.83 C and ~50 mAh g^{-1} @ 41.7 C) than that for SIB (~58 mAh g^{-1} @ 0.83 C and ~21 mAh g^{-1} @ 41.7 C).

To overcome the potential limitation in aqueous electrolytes, some studies have also involved organic electrolytes.[208-210] Goodenough's group has prepared KMFe(CN)$_6$ compounds (M = Mn, Fe, Co, Ni and Zn) as cathodes in EC/DEC (1/1, DEC = diethyl carbonate) with 1 M NaClO$_4$ cycling at 0.05 C.[209] KFe$_2$(CN)$_6$ has exhibited not only the largest capacity (~96 mAh g^{-1}) than other KMFe(CN)$_6$ (around 32–68 mAh g^{-1}), but also >99% capacity retention after 30 cycles. However, the initial CE has been determined to be only ~60%. The same group has further reported rhombohedral Na$_{1.72}$MnFe(CN)$_6$ cathode, which delivers a high initial CE (93.7%), a plateau voltage of ~3.3 V, as well as high reversible capacity and rate performance (130 mAh g^{-1} @ 0.05 C and 45 mAh g^{-1} @ 40 C).[208]

Aside from PB-related materials, cathodes based on other MOFs have also been sporadically investigated. For example, an iron-oxalato framework (K$_4$Na$_2$[Fe(C$_2$O$_4$)$_2$]$_3$·2H$_2$O) has been reported for reversible Na-ion intercalation/extraction, but only a low reversible capacity of 45 mAh g^{-1} at 0.02 C has been acquired.[211]

MOFs as anodes for LIBs

The MOF-based anodes have received much more attention than MOF-based cathodes. However, it needs to mention that a plateau voltage is scarcely observed. The design ideas can be classified by the engineering of metal SBUs and organic linkers, respectively.

In an early study, Li-NTC, Ni-NTC and Li/Ni-NTC (NTC = 1,4,5,8-naphthalenetetracarboxylates) have been fabricated and evaluated as LIB anodes,[212] in which it has been proposed that lithium ions can be stepwise inserted to carboxylate groups and aromatic rings. Li/Ni-NTC, which is obtained by mixing Li-NTC and Ni-NTC, has displayed the best performance (initial CE of ~55.4%, capacity ~500 mAh g^{-1} @ 0.2 C, and capacity

retention ~100% after 80 cycles) probably due to the combination of high conductivity of Ni-NTC and high structural stability of Li-NTC. Attributed to the strong affinity of the carboxyl groups (hard base) to the Ti(IV) ions (hard acid), a Ti-DOBDC MOF (DOBDC = 2,5-dioxidobenzene-1,4-dicarboxylate) has been fabricated, showing a reversible capacity of ~527 mAh g^{-1} at 0.19 C and an impressive cycling stability of 85% retention after 500 cycles.[213] Another interesting work is based on the PB compounds which are usually applied as cathodes.[214] Although the studied PB analogues (*i.e.*, Co$_3$[Co(CN)$_6$]$_2$) has been proven feasible for anodes, only a moderate capacity (299.1 mAh g^{-1} @ 0.067 C) has been observed. Compared to monometallic MOFs, bimetallic systems often show better electrochemical performance. It has been exemplified by a bimetallic coordinating polymer, which is prepared by linking Zn and Co ions with terephthalic acid (H$_2$TPA) linkers in one-pot following by water treatment (**Figure 16d-f**).[215] Despite a low initial CE of ~62%, a very high reversible capacity (1211 mAh g^{-1} @ 0.08 C) has been obtained, which can sustain 402 mAh g^{-1} at 3.3 C. Additionally, a capacity of 622 mAh g^{-1} has been retained after 500 cycles at ~1.7 C.

Apart from metal centers, organic linkers also play critical roles in determining battery performance. Considerable efforts have been focused on the incorporation of diverse and/or abundant lithium-intercalation sites to boost specific capacity.[198, 216-217] For example, Mn-based ultrathin metal−organic framework nanosheets (Mn-UMOFNs) have been prepared with BDC as linkers by ultrasonication.[216] Several energy storage mechanisms are presented in the system, including the redox reactions of Mn^{2+}/Mn^0 couple (above 0.5 V, accompanying with the insertion of Li$^+$) and the insertion/extraction of Li$^+$ on carboxylate groups as well as benzene rings (below 0.5 V, 2 Li+ per carboxylate group and up to 6 Li$^+$ per benzene ring), thus affording a high theoretical capacity of 1392 mAh g^{-1}. In this light, a large capacity (1029 mAh g^{-1} @ 0.1 C and 701 mAh g^{-1} @ 1.9 C) and a low initial CE (57%) have been obtained. Additionally, the electrode maintains 818 mAh g^{-1} after 300 cycles at ~1 C, manifesting a striking stability.

Another work concentrates on introducing more lithiation sites. To achieve this, 1,2,3,4,5,6-benzenehexacarboxylate (BHC) has been adopted as linkers to coordinate Ni SBUs.[217] Featuring six carboxylate groups, the resulting Ni-BHC can theoretically accommodate 30 Li^+ per building unit, thus giving rise to a theoretical capacity of 1570 mAh g^{-1} and an experimentally reversible capacity of ~1261.3 mAh g^{-1} at 0.06 C. However, the rate performance (~33% retention @ 3.3 C) and cycling performance (~75.8% retention after 50 cycles) are moderate.

Moreover, some efforts have also been devoted to improve the stability of MOF-based anodes by versatile ligand design.[197, 204, 218-219] It is known that the engagement of central metal ions of MOFs in the redox reaction (*i.e.*, a conversion-type energy storage) can dismantle the original MOF structure particularly upon cycling, thus leading to instability. To solve this problem, it is desirable to restrict the lithium insertion/deinsertion to only organic linkers. A Mn-BTC MOF — which featured redox-active BTC linkers — has been designed,[204] where the unfavorable Mn^{2+}/Mn^0 conversion has been excluded. In this way, a reasonable capacity (694 mAh g^{-1} @ 0.15 C) and cycling stability (83% @ 100 cycles) have been achieved. Later on, a seashell-like Co-BDC MOF (S–Co-MOF) has been developed. Li^+ ions are intercalated to the carboxyl groups and benzene rings without the participation of cobalt, as evidenced by the maintained Co 3d–O 2p orbitals and Co 4sp–O 2p orbitals during different states of charge (**Figure 16g-i**).[197] In this light, a high initial CE (80.4%), good capacity (1107 mAh g^{-1} @ 0.09 C), and long-term stability (92.2% @ 200 cycles) have been obtained. Taking advantage of the thermal/chemical stability of phenyl groups and the potential lithium binding sites provided by amine groups, a 2-aminobenzimidazole (abIM) linker has been adopted in conjunction with imidazole (IM) to coordinate Zn ions.[219] In spite of a low capacity (190 mAh g^{-1} @ 0.53 C), the resulting $Zn(IM)_{1.5}(ABIM)_{0.5}$ demonstrated a superior stability of ~100% retention after 200 cycles.

MOFs as anodes for SIBs & PIBs

In comparison with cathode materials, MOFs as anode materials have not been widely reported. For SIB anodes, the energy storage mechanism has been recently revealed, which is similar to that for LIBs. Based on Co-BDC, by analyzing ex-situ x-ray absorption fine structure (XAFS) spectra and x-ray absorption spectroscopy (sXAS), it has been proven that both central metal ions and linkers are engaged in the charge/discharge process.[199] During discharge, a reduction of Co^{2+} to Co^0 (>0.4 V *vs.* Na/Na$^+$) and the insertion of Na$^+$ to the coordinated carboxyl oxygen atoms (<0.4 V) have been sequentially appear. Considering the poor electrical conductivity of most MOFs and aiming to maximizing the binding sites for Na$^+$, it is desirable to combine both high conductivity and high-density redox-active centers in one MOF, so as to promote rate performance and fully utilize the theoretical capacity. In this basis, Bao's group has prepared Co-hexaaminobenzene MOFs, which feature a pronounced bulk conductivity of 157 S m^{-1} and high-density imine functional groups.[220] The resulting Co-HAB anode has displayed remarkable rate performance (291 mAh g^{-1} @ 0.17 C and 152 mAh g^{-1} @ 41.2 C) while a moderate stability (76% retention after 50 cycles).

The first example of using MOFs as PIB anode has been reported in 2017 based on MIL-125(Ti).[221] The as-prepared MIL-125(Ti) features microporous structures with an average pore size of 1.60 nm and a large SSA of 1103 m^2 g^{-1}. Cycling within 0.01–3V *vs.* K/K$^+$, the MIL-125(Ti) electrode has exhibited initial CE of 58.9% and specific capacity of 210 mAh g^{-1} at 0.05 C. Additionally, a high capacity retention of 90.2% has been observed after 2000 cycles at 0.95 C. In another study, a cobalt(II) terephthalate-based layered MOF (L-Co$_2$(OH)$_2$BDC) has been tested for PIB anode, delivering a much larger capacitance (352 mAh g^{-1} @ 0.14 C and 131 mAh g^{-1} @ 2.8 C) and excellent cyclability (~80% retention after 600 cycles at 2.8 C).[222]

4.1.2 Engineering of pore structures

MOFs as cathodes for MIBs

There are only a few examples capitalizing on devising MOF-based cathodes for MIBs from the viewpoint of pore structure engineering. PB compounds are a kind of widely used cathode, which can be described by a general formulate as $Na_2M^{II}[M^{II}(CN)_6]$ (M, M' = Fe, Co, Mn, *etc.*). Hence, theoretically it can undergo a two-electron redox reaction by oxidation/reduction of both M and M' and thus offer Na-storage capacity of >120 mAh g^{-1}. However, it is hard to achieve it in the aqueous electrolyte (typically < 70 mAh g^{-1}), presumably due to the block of active sites by water on the lattice vacancies of PB frameworks. To address this issue, high-quality and vacancy-free $Na_xCoFe(CN)_6$ nanocrystals have been fabricated by controlled crystallization, generating well-defined PB nanocubes.[223] The CV curves have shown two sets of reversible symmetric oxidation/reduction peaks at 0.90 V (Fe^{2+}/Fe^{3+} couple) / 0.40 V (Co^{2+}/Co^{3+} couple) *vs.* Ag/AgCl, which is in consistent with two well-defined plateaus in the charge/discharge curves. In this light, high capacity (128 mAh g^{-1} @ 1 C) and superior cyclability (90% @ 800 cycles) have been achieved.

In another study, topotactic oxidative insertion reaction in MOFs has been found for the first time by chemical oxidation of $Fe_2(DOBDC)$ with thianthrenium hexafluorophosphate, producing $Fe_2(DOBDC)(PF_6)_{0.96}$·yMeCN (y ≈ 2.6).[224] By enlargement of the pore aperture by using a larger ligand (4,4'-dioxidobiphenyl-3,3'-dicarboxylate, DOBPDC), the resulting MOF can incorporate more anions with a formulation of $Fe_2(DOBPDC)(PF_6)_{1.56}$·yMeCN (y ≈ 5.1). Being paired with a sodium anode to form a dual-ion battery and testing in 0.6 M NaPF6 electrolyte (EC/DMC = 3/7), good rate performance (108 mAh g^{-1} @ 1 C and 77 mAh g^{-1} @ 2 C) and cyclability (91% @ 50 cycles) have been achieved.

MOFs as anodes for LIBs

57

To serve as anodes for LIBs, pore structures of MOFs have been controlled via modulating their porosities, SSAs, and dimensions.

To enhance the rate performance, enlargement of the pore size beyond the microporous scale is desirable so as to accelerate mass transfer. From the viewpoint of devising intrinsically mesoporous MOF, low-cost and environmental-friendly aluminum fumarates MOF (Al-FumAs) have been prepared.[225] A moderate S_{BET} (260.1 m^2 g^{-1}) and a broad PSD centering around 12−16 nm have been obtained (**Figure 17a-b**) due to a tremella-like structure assembled from ultrathin nanosheets. This mesoporous structure can simultaneously facilitate electrolyte/lithium access and accommodate Li$^+$ ions without substantial volume change. With different aluminum salts as precursors, it has been found that AlCl$_3$-FumAs and Al(NO$_3$)$_3$ hold both high reversible capacity and excellent rate performance (*ca.* 350−250 mAh g^{-1} with a constant discharge rate at 0.09 C while charge rates from 0.45−91.7 C, see **Figure 17c**). However, the initial CE is < 46% for all Al-FumAs probably due to their large SSAs and porosities. On the other hand, it is feasible to attain large pores by growing MOFs on porous current collectors. As seen from **Figure 17d-e**, via a microwave-assisted solvothermal method, CPO-27 vertical nanowire (NW) arrays are directly grown on nickel foams by linking multiple metals (Fe, Co, Ni) with DOBDC to serve as binder-free LIB anodes.[226] Therefore, porosities generated from both the interspace between NWs and the voids in Ni foams can efficiently promote mass transfer. Annealing at 250ºC in argon can further remove the solvent molecules to reduce side reactions, eventually leading to good rate performance (~700 mAh g^{-1} @ 0.07 C and 440 mAh g^{-1} @ 2.8 C, see **Figure 17f**), excellent cyclability (93% after 500 cycles @ 1.4 C), and a moderate initial CE (67%).

Besides directly modulating porosities, efforts have also been devoted to designing microstructural dimensionality of MOFs, for that the one- or more-dimensional confinement can shorten the diffusion pathway of Li$^+$ ions and expose large reaction sites. For example, an

1D Co-MOF ($Co_5(OH)_2(O_2CCH_3)_8 \cdot 2H_2O$) of 201.2 m^2 g^{-1} and broad PSD has been applied for LIB anodes, achieving a high capacity (1107 mAh g^{-1} @ 0.02 C) and outstanding stability (negligible capacity fade after 1000 cycles @ 0.9 C).[227] In addition, 2D-structured MOFs have also been studied.[228-229] A Mn-based 2D-layered MOF ([Mn(TFBDC)(4,4'-bpy)(H_2O)$_2$], H_2TFBDC = 2,3,5,6-tetrafluoroterephthalic acid, bpy = bipyridine) has been reported for LIB anodes. However, a very low initial CE (~33%) and a moderate reversible capacity (~390 mAh g^{-1} @ 0.13 C) have been obtained.[228] Recently, 2D/3D hybrid-dimensional Co-MOF microflowers have been obtained from the assembly of 2D Co-BDC nanoflakes (thickness of ~30 nm). In spite of a relatively low SSA (49.9 m^2 g^{-1}) and pore volume (0.224 cm^3 g^{-1}), an impressive capacity (1345 mAh g^{-1} @ 0.074 C and 798 mAh g^{-1} @ 1.5 C) and cyclability (negligible loss after 100 cycles @ 0.074 C) have been delivered presumably due to the broad PSD (5−50 nm) and hierarchical structures.[230]

Although high porosities and/or SSAs are preferred for EDLCs, they may do harm to the capacity and cyclability of batteries because of the intensified side reactions due to abundant reaction sites. To address these issues, a dual-ligand design has been proposed, where dimethylammonium (DMA) cations are confined in the pores of MOFs ([DMA]$_4$[Fe$_4$(BDC)$_2$(NDC)(SO$_4$)$_4$]$_\infty$), leading to a negligible SSA and porosity.[231] As a result, a high capacity (~825 mAh g^{-1} @ 0.3 C and ~500 mAh g^{-1} @ 3.6 C) and negligible capacity fade (1000 cycles @ 2.4 C) have been observed. It is worth mentioning that the specific capacity of the Fe-MOF has increased from 600 to 825 mAh g^{-1} after 100 cycles, which is attributed to the adsorption of a large number of ions from the capacitive behavior of the porous-material-based anode.

MOFs as anodes for SIBs & PIBs

Compared to Li^+ ions, the larger sizes of Na^+ and K^+ are prone to efficient intercalation/extraction in microporous MOFs. Therefore, a larger pore size that can be realized

by a longer organic linker is favorable. The performance of Co-BDC and Co-BPDC for SIBs have been compared by use of short BDC linkers or BPDC linkers.[232] As expected, the enlarged cell volume of Co-BPDC (1359.6 $Å^3$ for Co-BPDC and 862.5 $Å^3$ for Co-BDC) resulted in a larger capacity at a given rate, presumably due to promoted insertion and extraction kinetics of large-size sodium ions (>230 mAh g^{-1} for Co-BPDC and <100 mAh g^{-1} for Co-BPDC at a rate of 0.05 A g^{-1}). However, the initial CE of Co-BPDC is very low (<50%), perhaps due to severe SEI formation resulted from the large porosity of MOFs.

Most MOFs store Na^+ ions through the C=O and C=N functional groups as well as the redox reactions of central metal ions. To introduce more active sites, it is critical to activate the sp^2-hybridized carbons in the aromatic rings as shown in the LIB anodes. However, many organic compounds containing C=O and C=N groups have layered structures, where aromatic rings are buried in those structures and are not accessible to large-size Na^+ ions. Recently, a 3D open framework has been designed made up of Zn^{2+} and planar ligand 3,4,9,10-perylenetetracarboxylate (PTCA).[233] As shown in **Figure 17g**, the resulting wavy-layered Zn-PTCA frameworks allow the access of aromatic rings for Na^+ ion storage. As a result, impressive capacities (357 mAh g^{-1} @ 0.14 C and 256 mAh g^{-1} @ 2.8 C) and excellent cyclability (75.5% after 1000 cycles) have been obtained (**Figure 17h**). However, the issue of a low initial CE (45.3%) needs to be addressed in future by balancing the substantial SEI formation and the abundant active sites.

4.2. MOFs for solid-state electrolytes

MOFs have also been investigated as solid-state electrolytes for MIBs due to their intrinsic low electrical conductivity, adjustable and abundant pores for electrolyte access, large SSAs for homogeneous metal electrodeposition at high current densities, and tunable surface chemistry for controlling the mobility of charge carriers. Recently, there are a few excellent reviews

discussing the MOF-containing SSEs,[45, 234] which consist of MOF-incorporated polymer hybrids, ionic liquid-laden MOF hybrids, and neat MOFs. In the current review, we will only capitalize on neat MOFs.

As shown in **Figure 18a**, there are two main strategies to incorporate metal cations (Li$^+$, Na$^+$, K$^+$, *etc.*) into MOFs. In the first class, open metal sites (OMSs) are introduced into MOFs by removing originally coordinated solvent molecules via an activation process (*e.g.*, vacuum drying at elevated temperatures). Upon addition of metal salts, the anions of salts will be bind to OMSs, leaving charge-balancing metal cations as mobile charge carriers in the porous channels of MOFs. In the second class, negatively-charged sites are covalently imparted in MOFs to afford intrinsically anionic frameworks (MOFs can be regarded as a kind of anionic polyelectrolytes), hence the mobile counter-cations (*i.e.*, metal ions) can directly interact with MOF backbones and serve as charge carriers. Therefore, it is essential to deeply understand and engineer the interactions between cations-anions, MOF-cations, and MOF-anions, so as to maximize the mobility of metal cations and the metal cation transference number (*i.e.*, the fraction of metal cations among the total charge carriers).

Compared to the electrode studies, the research of neat-MOF SSEs is an emerging area. Challenges remain for achieving a high ionic conductivity ($>10^{-4}$ S cm^{-1} at room temperature), a wide working potential window (> 4 V), a large transference number (> 0.5), and an unambiguous understanding of the correlation between structure/composition and performance. To promote the research in this young yet promising field, here we will attempt to concisely demonstrate the design of neat-MOF electrolytes from fresh perspectives, *i.e.*, the pore chemistry and pore structure.

4.2.1. Engineering of pore chemistry

In this section, the design of MOFs with OMSs and intrinsic anionic frameworks will be separately delineated.

Open metal sites

Removal of solvent molecules or other substances from the as-obtained MOFs can release coordinatively-unsaturated metal sites, thus allowing for the immobilization of nucleophilic anions and leaving mobile metal cations upon soaking in the corresponding electrolyte solutions. This notion has been pioneered by Long *et al.* by using MOF-177, Cu-BTTri (BTTri^{3-} =1,3,5-tris(1*H*-1,2,3-triazol-5-yl)benzene)), and Mg$_2$(DOBDC) as SSEs.[235] Particularly, it has been found that the ionic conductivity is highly dependent on the specific metal salts. Grafting LiBF$_4$ and lithium isopropoxide (Li^{i}OPr) to Mg$_2$(DOBDC) by soaking MOFs in the corresponding solution has generated conductivities of 1.8×10^{-6} and 1.2×10^{-5} S cm^{-1}, respectively. The conductivity enhancement for Li^{i}OPr impregnation has been attributed to the screening of the negative charge of anions (*i.e.*, ^{i}OPr$^-$) with their large aliphatic groups, thus reducing the binding energies between anions and Li$^+$ cations and allowing for freely movement of the latter. By further optimization of lithium salts, the resulting Mg$_2$(DOBDC)·0.35Li^{i}OPr·0.25Li-BF$_4$·EC·DEC has gained a conductivity of as high as 3.1×10^{-4} S cm^{-1}. Based on the same idea (**Figure 18b**), a moderate ionic conductivity (1.8×10^{-5} S cm^{-1}) has been reported for the LiOtBu-grafted UiO-66 sample by sequentially dehydration of the cluster core of UiO-66 and subsequent grafting of lithium tert-butoxide (LiOtBu).[236]

In addition to the anions of metal salts, the metal centers of MOFs also play crucial roles in determining the performance. By use of MIL-100 series with identical pore structures but different metal sites (M-BTC, M = Al, Cr, or Fe) to incorporate LiClO$_4$, ionic conductivities have been found to increase with the order of Cr, Fe, and Al, where MIL-100-Al has exhibited a very high value of $>10^{-3}$ S cm^{-1} at room temperature.[237] This order is in line with the Lewis acidity of OMSs (Al^{3+} > Fe^{3+} > Cr^{3+}), which is attributed to that the ion-pairing between Li$^+$

and ClO_4^- are considerably weakened with stronger acid and thus enhance the transport of Li^+ ions.

To eliminate the polarization effects and avoid the parasitic reactions on electrodes, it is beneficial to increase the cation transference number. To realize this, it is required to enhance the binding energies between salt anions and MOFs. In this way, the anion-cation interactions can be reduced and thus generate more free cations as charge carriers, eventually producing single-ion SSEs (cation transfer number approaching 1). As reported by Dincă *et al.*, by utilizing the reversible transition of anionic $(CH_3)_2NH_2)[Cu_2Cl_3BTDD]\cdot(DMF)_4(H_2O)_{4.5}$ (MIT-20, H_2BTDD = bis(1H-1,2,3-triazolo[4,5-b],[4',5'-i])dibenzo-[1,4]dioxin) and neutral Cu_2Cl_2BTDD (MIT-20d) via removal of one-equivalent dimethylammonium chloride, metal salts (LiCl, NaSCN, and $MgBr_2$) can be stoichiometric incorporated to produce single-ion SSEs.[238] Particularly, a high Li^+ transference number (t_{Li+}) of 0.66 and a moderate ionic conductivity of 1.3×10^{-5} S cm^{-1} have been observed for MIT-20-LiCl ($Li[Cu_2Cl_3BTDD]\cdot10(PC)$, PC = propylene carbonate), suggesting Li^+-dominated ionic conduction. In the framework of this notion, the same group has introduced $Cu_4(TTPM)_2$ (H_4TTPM = tetrakis(4-tetrazolylphenyl)methane) as a new kind of MOF host that feature five possible halide binding sites per SBU, aiming to further increase the loading of mobile metal cations (Li^+, Mg^{2+}, and Al^{3+}).[239] For example, 1.8 equivalent LiCl has been uptaken per SBU as seen from the formula $Cu_4(TTPM)_2(CuCl_2)_{0.6}(LiCl)_{1.8}\cdot19PC$, resulting in a promoted ionic conductivity and t_{Li+} (2.4×10^{-5} S cm^{-1} and 0.69) compared to the previous study.

Intrinsic anionic frameworks

As schemed in **Figure 18a**, aside from incorporation of metal ions mediated by the coordination between OMSs and anions, it is feasible to directly bind metal ions to intrinsically anionic MOFs.

The first attempt might be the substitution of trivalent Sc^{3+} ions in MOF SBUs by a combination of monovalent (*e.g.*, Li^+ and Na^+) and divalent ions (*e.g.*, Cd^{2+} and Mn^{2+}), where the latter support the framework structure while the former serve as free charge carriers to balance the negatively-charged MOF frameworks.[240] However, the ionic conductivities (10^{-7}–10^{-6} S cm^{-1}) are quite low. Afterwards, an anionic Al-MOFs based on negatively-charged tetrahedral AlO_4 units have been fabricated from 1,4-dihydroxybenzene and lithium aluminum hydride, where Li^+ ions have been in situ incorporated in the anionic frameworks with a loading of as high as 2.50 wt.%.[241] Consequently, a reasonable ionic conductivity of 5.7×10^{-5} S cm^{-1} has been acquired. To facilitate Li^+ loading, $[(MnMo_6)_2(TFPM)]_{imine}$ (*i.e.*, MOF-688, TFPM = tetrakis(4-formylphenyl)methane) carrying three negative charges per $MnMo_6$ (balanced by tetrabutylammonium (TBA) cations) has been fabricated as schemed in **Figure 18c**.[242] After exchange of TBA^+ with lithium bis(trifluoromethanesulfonyl)imide (LiTFSI), both high ionic conductivity and extraordinary t_{Li+} have been obtained (3.4×10^{-4} S cm^{-1} at 20 °C and 0.87).

Besides bottom-up synthesis, an anionic trifluoromethanesulfonyl group (*i.e.*, NSO_2CF_3K) has been anchored on the backbone of UiO-66 by post covalent grafting, leading to an anionic UiO-66 MOF (**Figure 18d**).[243] Attributed to the enhanced delocalization of negative charge on nitrogen resulted from the strong electron-absorbing effect of O=S=O group, the interactions of Li^+-anion pairing has been reduced, thus realizing a high ionic conductivity and t_{Li+} (2.07×10^{-4} S cm^{-1} at 25 °C and 0.84).

4.2.2. Engineering of pore structures

Compared to pore chemistry, less attention has been paid to tailoring pore structures of MOFs to optimize the performance of SSEs. Current efforts mostly focus on the pore size modulation of MOFs. In a probably first report by Long *et al.*, Mg_2(DOBPDC) and Mg_2(DOBDC) with a similar topology but different pore sizes (diameter of 2.1 and 1.3 nm, respectively) are

employed to host Mg^{2+} ions.[244] The former can accommodate more Mg^{2+} ions, leading to 100-fold increase in ionic conductivity (10^{-4} *vs.* 10^{-6} S cm^{-1}). In another study, the SSE properties of Zr-BDC (UiO-66) and Zr-BPDC (UiO-67) are compared using $LiClO_4$ as the electrolyte.[237] The larger pore size in UiO-67 leads to a higher Li^+ conductivity (6.5×10^{-4} *vs.* 1.8×10^{-6} S cm^{-1}) as a result of a higher level of Li^+ ion solvation and a higher mobility.

4.3. MOF-derivatives for electrodes

As aforementioned, a wide range of MOF-derivatives have been created in the last decade, while the application of them for MIBs is exclusively concentrating on the anode materials (particularly for carbons, MO_x, and MO_x/carbon), although rare examples have been also demonstrated for cathode materials.[245] In the following, different kinds of MOF-derivatives for MIB anodes will be summarized in the two subsections, *i.e.*, the engineering of pore chemistry and pore structures.

4.3.1 Engineering of pore chemistry

MOF-derived carbon

Depending on MOF precursors and processing conditions, hieratically-structured pristine carbons or heteroatom-doped carbons can be obtained for MIB anodes. Particularly, nitrogen-doped carbons have attracted tremendous interest because of their enhanced electrical conductivity and emerging reaction sites that are associated with the specific nitrogen species. To enhance the anodic performance of LIBs, nitrogen-doped porous carbons have been synthesized by annealing ZIF-8 which features nitrogen-abundant ligands (34 wt.% N in 2-MIM).[140] Pyrolysis at 800ºC has generated nitrogen-doped carbon with both high total nitrogen content (17.72 wt.%) as well as substantial pyrrolic N (N-5) and pyridonic N (N-6).

The presence of abundant electrochemical active N-5 and N-6 sites as well as nanopores largely promote lithium storage, thus affording outstanding specific capacitance (2037 mAh g^{-1} @ 0.05 C and ~780 mAh g^{-1} @ 2.5 C, see **Figures 19a-b**).

Recently, MOF-derived carbons have also been explored as anodes for SIBs and PIBs.[132, 134, 246] A low-cost [Cu(HMT)$_2$(NO$_3$)$_2$]$_n$ MOF (HMT = hexamine) has been adopted as precursors for preparing nitrogen-doped carbons as SIB anodes.[246] The nitrogen content (13.32–29.42 at.%) and the type of nitrogen species (marked by the ratio of pyridonic-N/graphitic-N, $i.e.$, N-6/N-Q) have been found to be negatively-correlated to the pyrolysis temperatures (600–900ºC). In contrast with the previously reported LIB anodes where N-5 and N-6 are claimed critical for lithium storage, this study shows that graphitic-N and N-oxide (N-O) are more favored. The reversible capacity, the cycling capacity retention, and the rate capacity retention have been found to be linearly correlated to the fraction of N-Q, N-6/N-Q, and (N-6/N-Q)^2, respectively. Balancing above factors, the sample pyrolyzed at 800ºC (N-Q/C = 6.35 and N-6/N-Q = 2.86) has given rise to an overall best performance, with reversible capacity of 254 mAh g^{-1} @ 0.39 C (sustain 142 mAh g^{-1} @ 19.7 C), initial CE of 58%, and capacity retention of ~80.7% after 100 cycles at 0.39 C. In another study, by annealing of 2D Mn-BDC in ammonia atmosphere following by acid cleaning, nitrogen-doped carbon foils have been derived.[134] Featuring multiscale pores and a large SSA (417.8 m^2 g^{-1}), an enhanced capacity (306 mAh g^{-1} @ 0.16 C and 150 mAh g^{-1} @ 32.7 C) and moderate cyclability (72.8% after 1000 cycles) are resulted, while a quite low initial CE (~34%) has been observed due to their large SSAs. PIB anodes are reported recently, where nitrogen-doped carbons have been derived from ZIF-67.[132] An optimized annealing temperature at 600ºC can produce the largest fraction of pyridinic N, strongly promoting the adsorption/desorption of K$^+$ ions ($i.e.$, the pseudocapacitance effect) and affording a high reversible capacity (587.6 mAh g^{-1} @ 0.085 C and 186.2 mAh g^{-1} @ 3.4 C) yet a low initial CE (~31.5%).

MOF-derived MO$_x$

In comparison with pure carbons, metal oxides can offer much larger capacity due to the potential conversion reactions with alkaline metals during charge/discharge process.

Based on MOFs with different metal centers, metal oxides of versatile chemical compositions can be acquired after annealing in air. In this light, MOF-derived MO$_x$ such as ZnO, Fe$_2$O$_3$, CuO, TiO$_2$, and Mn$_2$O$_3$ have been acquired for LIB anodes, holding diverse features marked by their chemical nature. For example, hierarchical porous anatase TiO$_2$-based anodes derived from MIL-125 (Ti) enjoy excellent rate performance (53.6–65.2% retention at 10 C with respect to the capacity at 0.1 C), cyclability (>93.5% after 200 cycles), and high initial CE (72–86%), while the reversible capacity is quite low (210–240 mAh g^{-1} @ 0.1 C).[247-248] In comparison, ZnO and α-Fe$_2$O$_3$ based electrodes display much higher capacity (805.4 and ~1000 mAh g^{-1} for ZnO and α-Fe$_2$O$_3$, respectively) due to the conversion reactions, while <50% capacity retention has been found at high charge/discharge rate (6–10 C).[126, 249] From an economic viewpoint, Mn-based MOF-derived materials show impressive performance-to-price ratio. Porous Mn$_2$O$_3$ derived from [Mn(Br$_4$-BDC)(4,4'-bpy)(H$_2$O)$_2$]$_n$ delivers both high capacity (917 mAh g^{-1} @ 0.22 C and 450 mAh g^{-1} @ 4.4 C) and good cyclability (88.1% after 250 cycles).[121] Additionally, its initial CE of 73.7% is also higher than that of most MOF-derivatives, highlighting their practical values. It needs to mention that the valence of metals in the oxides can play a vital role. For instance, Co$_3$O$_4$ nanocages and microframes show similar capacities as LIB anodes (1069 & 1092 mAh g^{-1} @ ~0.09 C),[250-251] which these values are much smaller compared to that for CoO NPs (1383 mAh g^{-1} @ 0.1 C).[252]

Apart from single-metallic metal oxides, porous multimetallic metal oxides have also been acquired from the corresponding MOFs which are synthesized *in situ* or by post treatment. The synergy of multiple metal oxides may bring additional advantages (*e.g.*, a higher electrical

conductivity) to boost the battery performance.[253] In a study, Zn-ZIF-67 and Ni-ZIF-67 have been prepared as precursors from post metal-ion exchangewith ZIF-67, which are then annealed to yield the corresponding Zn- and Ni-doped Co_3O_4.[254] Both bimetallic oxides (Zn-Co-oxide and Ni-Co-oxide) exhibit considerably higher capacity than that for pristine Co_3O_4 as LIB anodes (~1300 *vs.* ~1100 mAh g^{-1} @ 1 A g^{-1}). Particularly, the Zn-Co-oxide maintain the same high capacity even after 700 cycles at 1 A g^{-1}, suggesting its outstanding stability. Another study has adopted bimetallic Co-Zn-2-MIM MOF nanosheets as precursors, where the derived Co_3O_4/ZnO NSs manifest both high capacity and high cyclability for LIBs (851 mAh g^{-1} @ 0.12 C, 95.6% retention after 1000 cycles at 3.5 C) and SIBs (437 mAh g^{-1} @ 0.23 C, 91% retention after 1000 cycles at 4.6 C).[255]

MOF-derived MO_x/C

Instead of calcination in air, pyrolysis of MOFs in an inert atmosphere can produce MO_x/C composites that combine the high capacity of MO_x and high electrical conductivity of carbon, thus enabling the delivery of both high capacity and rate performance.

Similar to the pure metal oxides, the type of metals in the composites can be controlled by selecting desirable MOF precursors. Over the years, various MO_x/C have been prepared, delivering diverse capacities (750, 966, and 1191.2 mAh g^{-1} @ ~0.1 C for ZnO/C, CoO/C, and MnO/C, respectively) and cyclability (74.3%, 110%, and 157% capacity retention after 100, 300, and 1000 cycles, respectively).[144, 256-257] The >100% retention can be attributed to an electrode activation process. In addition to modulation of the chemical compositions of single metallic oxides/carbon, multimetallic oxides/carbon have also been investigated. A systematic research has studied diverse MOF-derived MFe_2O_4/carbon (M = Zn, Mn, Co, Ni) spindles for LIB anodes.[28] As shown in **Figures 19c-f**, the four samples show similar reversible capacity (*ca.* 750–950 mAh g^{-1} @ 0.2 C), while $MnFe_2O_4$/carbon possess better rate performance of ~470 mAh g^{-1} @ 6.4 C.

Besides LIBs, MO$_x$/C have also been adopted for constructing SIB anodes. Both rutile TiO$_2$/C and MnO/C have been fabricated as electrode materials, displaying moderate capacities (160–250 mAh g^{-1} @ ~0.5 C) and excellent cyclability (no obvious capacity fade after >2000 cycles @ 10–20 C).[142-143] Note the performance of them is much better than that of the corresponding pure metal oxides, suggesting critical roles played by carbons. In another study, ZnO/amorphous carbon nitride has been prepared by pyrolyzing ZIF-8 at 700ºC, where a remarkable nitrogen (20.4 wt.%) has been included.[258] As a result, a high reversible capacity of 430 mAh g^{-1} at 0.2 C and a reasonable cyclability (~65% retention after 2000 cycles at 3.9 C) are obtained.

Other MOF-derivatives

In addition to carbon, metal oxides, and metal oxides/carbon, various MOF-derivatives including metal/carbon, MS$_x$/C, MSe$_x$/C, MN$_x$/C and MP$_x$/C have also been probed for MIBs.[29-31, 149, 153, 156, 259-260] For example, micro/mesoporous Bi@C nanoplates have been fabricated by pyrolyzing Bi-BTC MOFs under N$_2$ atmosphere, which deliver a good capacity of 676 mAh g^{-1} @ 0.074 C and excellent cyclability (~104.2% of initial capacity after 200 cycles) as LIB anodes.[149] To create high-performance SIB anodes, CoS$_2$/N-doped carbon spheres have been fabricated by pyrolysis of Co-BTC with sulfur powder at 550ºC.[29] Featuring hierarchical pores (<2 nm & 5–10 nm) and a special architecture (CoS$_2$ nanoparticles have been embedded in a 2 nm-thick amorphous carbon layer), the resulting composite displays an extraordinary capacity and rate performance (782.3 mAh g^{-1} @ 0.13 C and 637.4 mAh g^{-1} @ 13 C). Additionally, a high initial CE (82.1%) and excellent cyclability (no obvious decrease after 100 cycles) are obtained. In a very recent study as shown in **Figure 19g**, CoP polyhedral have been confined in nitrogen-doped porous carbon (NC@CoP/NC) by sequentially carbonization and phosphatization of ZIF-8@ZIF-67 precursors.[153] As seen from **Figures 19h-i**, due to the

lowest charge-transfer resistance, NC@CoP/NC displays a better specific capacity compared to nitrogen-doped carbon and CoP/carbon composites.

4.3.2 Engineering of pore structures

MOF-derived carbon

Several studies have shown that BET surface areas and pore sizes of MOF-derived carbons can be feasibly modulated by altering pyrolysis temperatures, thereby controlling their LIB performance.[157, 161, 261] For example, porous carbon NSs have been prepared by sequentially pyrolysis and acid etching of Al-MOFs (denoted as PCNS-*n*, *n* represents the pyrolysis temperature).[157] With raising temperature, both the S_{BET} and total volume (V_{tot}) increased and then decreased (reaching the maximum value for PCNS-700, *i.e.*, 1571.4 m^2 g^{-1} and 1.78 cm^3 g^{-1}). As a result, the PCNS-700 manifests the best performance with both high capacity (1126 mAh g^{-1} @ 0.09 C and 244 mAh g^{-1} @ 17.8 C) and ~100% capacity retention after 100 cycles, which can be attributed to its abundant accessible reaction sites and mass-transfer highways. By use of Zn-PBAI (H_2PBAI = 5-(4-pyridin-4-yl-benzoylamino)isophthalic acid) as precursors, the resulting porous carbon polyhedron reaches the highest S_{BET}, V_{tot}, and electrical conductivity (1254 m^2 g^{-1}, 0.52 cm^3 g^{-1}, and 18.4 S cm^{-1}) at pyrolysis temperature of 1000ºC (PCP-1000).[261] Consequently, the highest reversible capacity (1125 mAh g^{-1} @ 0.44 C) is obtained with it.

Besides SSAs and pore volumes, devising special architectures can serve as another route to manipulate pore structures and battery performance. Monocrystalline hollow carbon nanobubbles have been fabricated by pyrolysis of tannic-acid-etching-derived hollow ZIF-8 with subsequent HCl etching.[262] The average size of carbon nanobubbles is around 60 nm and the shell thickness is about 10 nm, thus featuring macropores. Compared to the non-hollow carbon NPs derived from solid ZIF-8, hollow carbon nanobubbles exhibit a much better rate

performance as SIB anodes (~100 *vs.* ~0 mAh g^{-1} @ 42.4 C) due to the existence of both battery-type and pseudocapacitance-type energy storage mechanisms. Another interesting work is demonstrated by Xiong *et al.*, where the annealing of ZIF-67 under Ar/H$_2$ (95%/5%) has given rise to nitrogen-doped multi-walled carbon nanotubes (NCNTs) due to the cobalt-assist catalysis (**Figure 20a-c**).[263] The resulting NCNTs possess an outer diameter of ~20 nm, showing S_{BET} = 126 m^2 g^{-1} and V_{tot} = 0.412 cm^3 g^{-1}. Due to the highly efficient electron transfer and the deformable graphitic layer in 1D NCNTs, they deliver a reversible capacity of as high as ~270 mAh g^{-1} at ~0.07 C for PIB storage. However, the very low CE (24.45% and 88.65% for the 1st and 10th cycle, respectively) poses a large barrier for their commercialization. In a recent study, nitrogen-doped hierarchical porous carbon (N-HPC) has been created by carbonization of 3D ordered macroporous ZIF-8, which features large SSA (820 m^2 g^{-1}), large pore volume (~0.8 cm^3 g^{-1}), and micro-meso-macroporous structures.[159] Attributed to the 3D bicontinuous porous frameworks and enhanced electronic conductivity, the N-HPC shows high reversible capacity (292 mAh g^{-1} @ 0.34 C and 94 mAh g^{-1} @ 34.2 C), long cycle life (157 mAh g^{-1} for 12000 cycles @ 6.8 C), and a moderate initial CE (~59%) as PIB anodes.

MOF-derived MO$_x$

In an early study, several-type Sn$_{1-x}$Fe$_x$O$_2$ microspheres with different pore parameters have been obtained by calcinating Sn$_m$[Fe(CN)$_6$]$_n$ precursors at different temperatures.[123] With increase of temperature from 350 to 650ºC, SSA decreases from 108.6 to 51.6 m^2 g^{-1} and the average pore size (determined by BJH method) increases from 4 to 9 nm. The resulting capacity as LIB anodes has been found to decrease with increasing temperature, showing the optimized value of 870 mAh g^{-1} at ~0.23 C for the sample pyrolyzed at 350ºC. Note that the cyclability is quite low, which is ~47.5% retention after 100 cycles.

On the other hand, engineering dimensions of MO_x provides another route to modulate their pore structure and thus the performance for LIB anodes.[264-266] Taking advantage of mesoporous nanorod architecture resulting from calcination of Co/Ni-MOF-74 nanorods, a broad PSD (2.2–2.5 & 10–30 nm) is presented for the obtained 1D mesoporous Co–Ni–O nanorods which are assembled from interconnected nanoparticles ($\approx$ 20–40 nm in diameter).[265] Thanks to such unique structures as well as the large theoretical capacity of metal oxides, an impressive capacity (~1189 mAh g^{-1} @ 0.084 C), excellent rate performance (65.6% capacity retention @ 4.2 C), and long cycling life (negligible capacity fade after 500 cycles @ 2C) have been acquired. In another study, 2D porous ZnO/ZnCo$_2$O$_4$ NSs assembled from interconnected NPs (diameter ~30 nm) have been fabricated by calcination of Zn-Co-MOFs with terephthalic acid as linkers.[266] Such hierarchical structure can not only provide rich reaction sites and facilitate mass transfer, but also accommodate large volume expansions upon lithium insertion. In this light, impressive capacities (1173 mAh g^{-1} @ 0.17 C and 824 mAh g^{-1} @ 4.3 C) and long-term stability (1016 mAh g^{-1} after 250 cycles @ 1.7 C) have been realized.

To boost the LIB performance, various complex microstructures have also been designed. Highly symmetric porous Zn$_x$Co$_{3-x}$O$_4$ hollow polyhedra have been obtained from Zn-Co-ZIFs-0.33 by sequentially annealing in nitrogen and air at 400ºC so as to preserve the ZIF framework (**Figure 20d**).[127] The hollow framework featuring both macropores and bimodal mesopores (centering at 4 & 9 nm) offers substantial reaction sites (S_{BET} = 65.6 m^2 g^{-1}) and channels accessible to electrolytes and reactants, affording outstanding reversible capacity (1020 mAh g^{-1} @ 1 C) and excellent rate performance (56.3% capacity retention @ 10 C, see **Figure 20e**). In a recent study, by controlled calcination of Ni-Co-BTC, multi-shelled Ni$_x$Co$_{3-x}$O$_4$-0.1 hollow microspheres (MSs) assembled from small NPs have been derived due to the heterogeneous heat-induced contraction process, showing a high SSA of 96.7 m^2 g^{-1}.[267] Such a unique structure can not only shorten the Li$^+$ diffusion distance, but also provide large voids for

accessing to electrolytes and accommodating volume change during charge/discharge. In this regard, a high reversible capacity of 1104 mAh g^{-1} has been achieved at ~0.09 C.

MOF-derived MO$_x$/C

To attain high-performance LIB anodes, diverse-morphological metal oxides/carbon derived from MOFs have been designed.[144, 257, 268-269] For example, dandelion-like CoO@C has been synthesized by pyrolysis of 2D Kagóme metal organic layers ([Co$_3$(μ-OH)$_2$(*o*-benzenedicarboxylate)$_2$]$_n$ MOLs).[257] Each dandelion is made up of many 1D NWs with lengths of 0.5−1 μm, where open space between adjacent nanowires can facilitate the diffusion of electrolytes and tolerate the volume change during lithium insertion/desertion. With such design, a reversible capacity of 866 mAh g^{-1} @ ~0.12 C and an excellent cyclability (no visible capacity fade after 300 cycles) have been obtained. A similar capacity (860 mAh g^{-1} @ ~0.12 C) has been achieved by ZnO-MoO$_2$/C (ZMO/C-600), which shows a high SSA and pore volume (167 m^2 g^{-1} and 0.39 cm^3 g^{-1}).[269] Recently, well-defined MnO/C MSs assembled from radial-aligned rods (width ~200 nm) have been obtained by pyrolyzing Mn-BTC, where rods comprise of MnO NPs that are wrapped with a thin carbon layer (thickness of 5−8 nm).[144] Based on this 3D hierarchical structure, a reversible capacity of up to 1191.2 mAh g^{-1} at 0.1 C has been achieved, and a continuous increase of capacity to around 600 mAh g^{-1} has been observed along 1000 cycling at 5 C.

MOF-derived metal oxides/carbon have also been applied for SIBs. CuO/Cu$_2$O composite hollow octahedrons have been obtained by pyrolyzing Cu-BTC at 300–400ºC.[129] The optimized sample, although with a low SSA of 10.65 m^2 g^{-1}, exhibits a high capacity of 440 mAh g^{-1} @ 0.11 C. In another study, Co$_3$O$_4$@NC core-shell NPs derived from ZIF-67 has been prepared.[270] Featuring a large SSA (101 m^2 g^{-1}) and broad PSD, a high capacity of 506 mAh g^{-1} @ 0.2 C is acquired while a moderate cycling performance (87% capacity retention after 60

cycles @ 0.4 C) is observed. In a recent work, unique vanadium oxide/porous carbon nanorods (VO_x/PCs) with perpendicularly-distributed slit-like 2D pores have been synthesized, showing a high SSA of 84.9 m^2 g^{-1}.[271] Attributed to such rarely-observed porous structure which allows fast ion transport and intercalation, a high reversible capacity (481.5 mAh g^{-1} @ 0.083 C) and a reasonable cycling performance (~75% capacity retention after 2000 cycles) are accordingly derived (**Figure 20f-h**).

5. Conclusions

The last decade has witnessed an extensive development of MOFs and their derivatives for applications in electrochemical energy storage, particularly for supercapacitors and metal-ion batteries. At the molecular level, by subtly devising bonding interactions and molecular symmetry, highly-tailorable MOFs with long-range-ordered, molecular-accurate, and size- and chemistry-tunable porous structures have been synthesized. At material design level, versatile macroporous MOFs and MOF-derivatives have been obtained with more "material-style" approaches, *e.g.*, controlled assembly, templating, high-temperature annealing, and other chemical/physical treatment. At application level, formulating the active MOF-based materials with other additives (*e.g.*, binders and conductive carbons), optimizing the device assembly techniques, and exploring the upscale production have been extensively attempted. Considering the highly-tunable pores of MOFs, this review has summarized the state-of-the-art synthesis strategies and application efforts of MOF-based materials from the viewpoints of pore chemistry and pore structure design, aiming to systematically demonstrate maneuvers for tailoring porosities of MOF-based materials for devising high-performance EES devices.

Generally speaking, synthesis strategies are quite mature for both MOFs and their derivatives, while there are big gaps between the MOF and the EES communities. Firstly, quite a few subtly designed MOFs and their derivatives have not been adopted for energy storage, although their

pore chemistry and structure are envisioned to be promising for optimizing the performance or investigating the design guidelines for energy storage devices. Secondly, a deep cooperation between experts in MOF fields and in EES is lacking. While a vast amount of MOF-based materials with accurate structures at molecular level have been elegantly synthesized, their application efforts are mostly restricted to less-important anode materials for MIBs without given the "C" rate and to less-practical measurement conditions for supercapacitors (*e.g.*, three-electrode tests in aqueous solutions). In contrast, despite many MOF-based materials have been optimized for energy storage with impressive performance, only few of these studies touch upon the molecular basis and thus discourage on-target design. Thirdly, certain innovative designs combining the knowledge of MOFs, energy storage and system requirements can be quite beneficial. For example, regarding the requirement for extracting less-abundant metals on the earth from seawater as well as the adjustable pores and the alkaline-metal insertion capacity of MOFs, it might be possible to selectively collecting Li^+, Na^+, K^+, and so on by a battery-like insertion/desertion process as reported for TiO_2-coated $FePO_4$ electrodes.[272] Therefore, in-depth communications of interdisciplinary-background researchers are urgently needed. In the following, the challenges and potential opportunities for MOF-based materials are detailed from synthesis and EES application aspects.

5.1 Synthesis

In the last few decades, the synthesis methodology for MOFs and their derivatives have been thoroughly investigated, generating countless MOFs and their derivatives. To tailor specific functions, both pore structures (*e.g.*, PSD, pore volumes, SSAs, and topologies) and pore chemistry of these MOF-based materials have been elegantly designed. However, there are some concerns need to be addressed to further promote their practical use.

Firstly, to extract the relationship between structure/composition and their performance for energy applications, it is desirable to develop creative tactics to decouple different parameters, so as to unambiguously figure out the contribution of each factor. For instance, many studies have succeeded in systematically modulating the SSA of MOF-based materials by design the length of organic linkers or by post treatment. However, the pore volumes and the pore size have also been altered accordingly, posing difficulties to discern the contribution of respective parameter.

Secondly, multiscale precise modulation needs to be further addressed. The precise construction and characterization of MOF-based materials with spatial-resolved metal distribution (particularly for MTV-MOFs), multiscale tunable pores, and well-defined dimensions/morphologies is still challenging. A very recent work delivered by Yaghi's group has shed light on this issue.[273] Briefly, atom probe tomography technique — in which sample are sequentially evaporated from the surface by laser pulsing and identified by time-of-flight mass spectrometry — has been used for unveiling metal sequences in bimetallic MTV-MOFs at molecular level. By adjusting the mixing enthalpy (lattice matching of two metals) and configurational entropy (the number of ways for metal arrangement) via controlling the kinds of metals as well as the reaction temperature, diverse metal sequences including randomly distribution, short/long duplicates, and insertions have been observed. However, considering materials for practical use, in addition to molecular-level composition/structure manipulation, the simultaneous control at meso- and macroscale is far from satisfactory and thus calls for efforts from interdisciplinary researchers.

Thirdly, aside from academic innovation, the research needs to consider the industrial needs for energy storage, such as the high conductivity, high chemical/thermal/water stability, low cost, scalable production capacity, and so on. Despite some efforts made, generally those attempts are at the infant stage and require unremitted efforts. For example, certain high-performance

MOF-based electrodes are prepared from conductive MOFs, which suffer from costly ligands adopted. MOF derivatives, which require additional procedures apart from MOF production can further raise the cost and thus limit mass production for practical use. Particularly, during the process of large-scale production, the intrinsically excellent pore properties of single-crystalline MOFs (*e.g.*, high SSA) might be compromised and more factors need to be considered such as crystalline boundaries, defects, and packing styles. Therefore, bearing industrial need in mind during material design is essential for the future design of MOF-based energy storage devices.

5.2 Energy storage applications

Conventionally, MOFs are not suitable for energy storage because of their intrinsic low electrical conductivity, low chemical stability, and dominant micropores. Along with more than ten-year efforts, most issues have been solved in various ways. In spite of profound progress, several critical challenges remain. For supercapacitors, although very high specific capacitances can be attained with electrodes based on MOFs and their derivatives (*e.g.*, >1000 F g^{-1}), currently the majority of studies are performed with three-electrode tests in narrow-voltage-window aqueous solutions, which is not compatible with the practical devices and can lead to a reduced energy density. For MIBs, both MOFs and their derivatives have been widely explored as the electrode materials particularly for anodes. Here, the key issues are the low average initial Coulomb efficiency (<75%) and the lack of stable voltage plateau, thus resulting in higher cost as well as lower energy and power density. Moreover, there is lack of study on the redox stability of MOFs as both supercapacitor and battery electrode materials and its effect on device performance, particularly at high-voltage ranges where high energy/power densities are favourably expected. Additionally, MOFs have also been studied as key components of

solid-state electrolytes, while this direction is only emerging in last few years and is still at its infant stage.

Although a substantial amount studies on MOF- and their derivatives have been presented, due to the huge versatility of MOF-based materials, so far, the relationship between the structure/chemistry and the device performance has not been discerned. In this regard, data from typical literature are summarized so as to provide potential direction for future design (**Figure 21**). It needs to mention that because of the extremely versatile and complicated structural and compositional parameters of MOF-based materials as well as the limited data reported in literature, the current summarization is only a tentative attempt. In-depth analysis by machine learning might be needed in future. Here, the application performance (*e.g.*, specific capacitance, specific capacity, and initial CE) has been correlated to both pore structures (*e.g.*, SSAs and V_{tot}) and pore chemistry. Surprisingly, the specific capacitance for supercapacitors is negatively correlated to the SSAs and V_{tot} (**Figures 21a-b**), which might be attributed to the presence of a large fraction of micropores which are not accessible to electrolyte ions. From the viewpoint of chemical composition, Co-based MOFs, Ni-based MOFs, and MOF-derived metal hydroxides usually feature large specific capacitances. These results suggest that EDL mechanism is less important for supercapacitor electrodes for MOF-based materials, hence the delicate design of the pore chemistry might be more rewarded.

For LIB anodes, the correlation is much less pronounced. From the structure aspect, the initial CE is negatively related to the V_{tot} for neat MOF-based materials, which can be associated with the lithium salt and electrolyte decomposition in the pores of MOFs (**Figures 21c**). However, no obvious correlation with SSA is observed (**Figures 21d**). For MOF-derivatives, the structure-performance of MOF-derivatives are not clear by analysis from SSA and V_{tot} (**Figures 21e-f**). From the chemistry aspect, Co- and Mn-based neat MOFs often deliver large specific capacities, while no obvious composition-dependent performance change is found for MOF-

derivatives. Overall, it is hard to extract a very clear design principles particularly for MOF-derivatives from current reports, and systematic studies are urgently desired.

Finally, targeting commercialization in future, much more technical issues need to be taken into consideration. For both MIBs and supercapacitors, most MOF-based materials frequently suffer from low stability (particularly for neat MOFs) and high production cost. Especially, regarding MOF-derivatives, additional fabrication procedures are required compared to neat MOFs, further decreasing the yield and raising the cost. Moreover, most current studies are only limited to lab-level research (*e.g.*, three-electrode tests for supercapacitors and coin cells for MIBs), while the prototype devices (*e.g.*, pouch cells for MIBs) are rarely studied. Note that for prototypes, more factors need to be considered (*e.g.*, low-CE-induced cost increase and gas generation), which in turn pose additional requirements for material design. Therefore, a long journey remains for the exploration of MOF-based materials for energy storage.

Figures and Tables

Figure 1. Number of Publications on the topic of MOFs for electrochemical energy storage. The data has been obtained by searching the subjects of (a) "metal organic frameworks", and (b) "metal organic frameworks" & "supercapacitors" as well as "metal organic frameworks" & "batteries" from web of science on December 2, 2020.
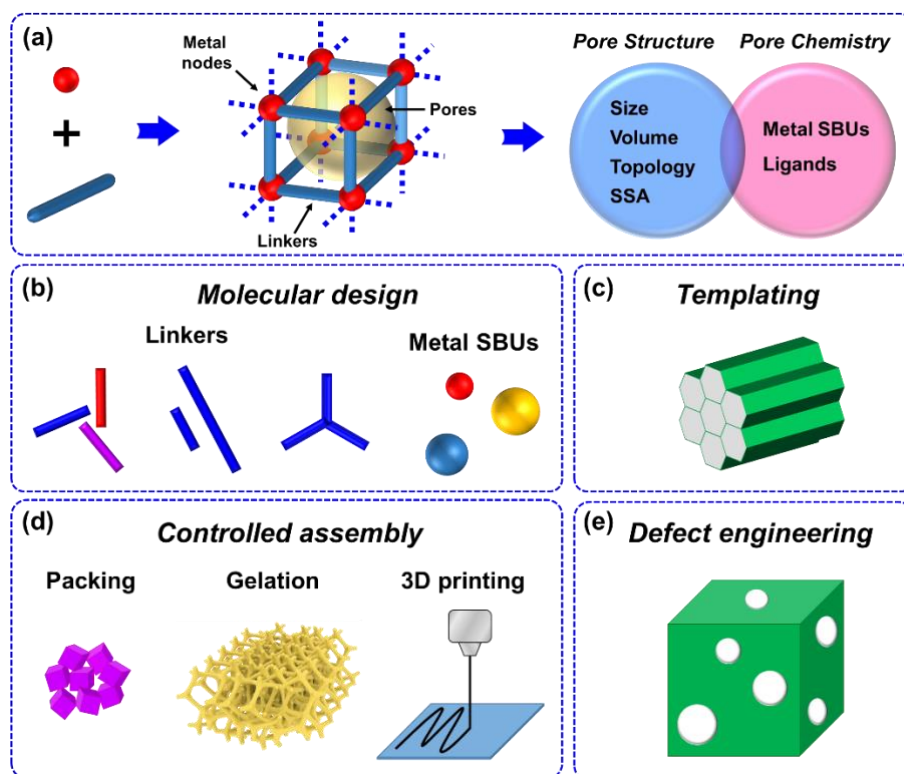

Figure 2. An overview of pore architecturing strategies for MOFs.

(a) Structural features and design directions of MOFs. (b-e) General strategies for manipulating pores, including (b) molecular design, (c) templating, (d) controlled assembly, and (e) effect engineering.
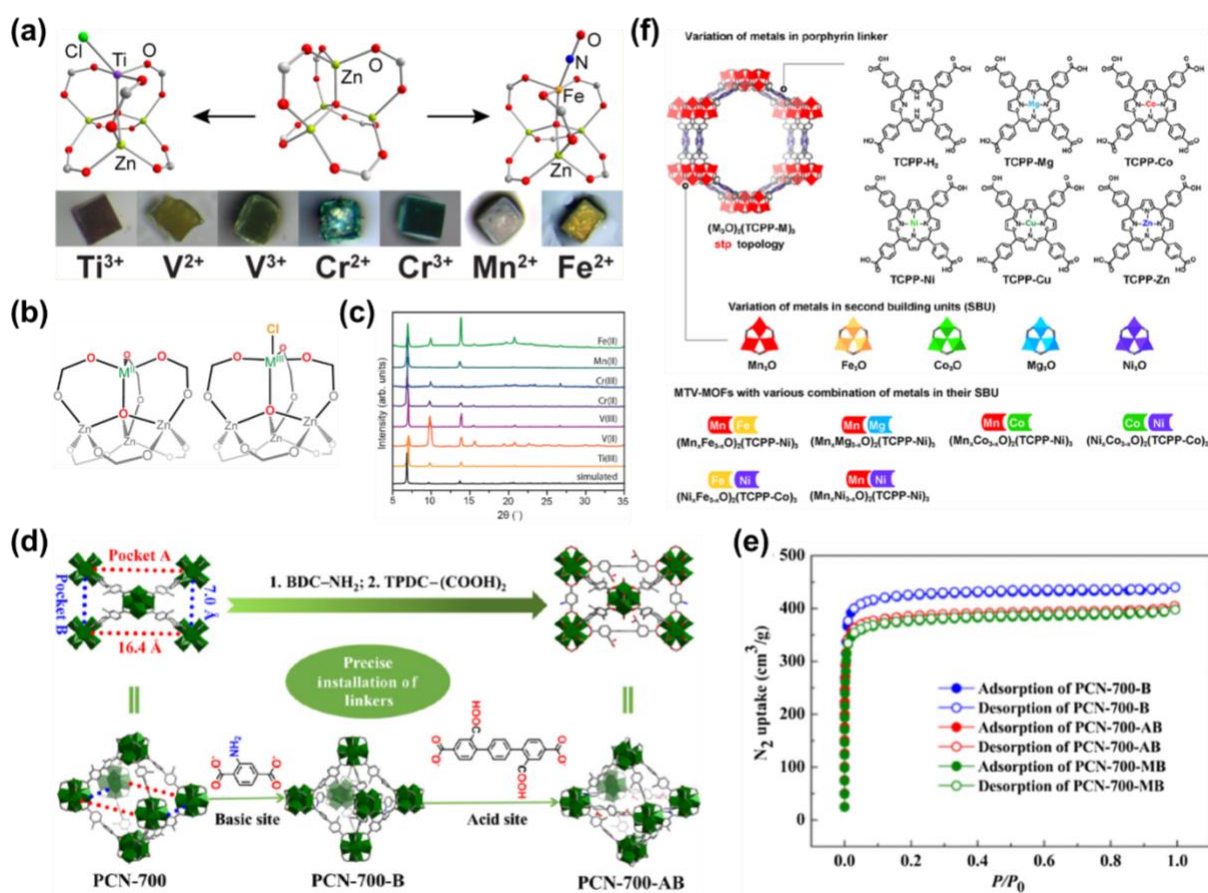
Figure 3. Pore chemistry design for MOFs.

(a-c) Design of metal SBUs by postsynthetic ion metathesis (PSIM). (a-b) Demonstration of the incorporation of various divalent- and trivalent metal ions into the metal SBUs of MOF-5, as well as the photographs of the corresponding materials. (c) Powder X-ray diffraction patterns of MOF-5 exchanged with indicated metal ions juxtaposed with the calculated pattern of MOF-5. Adapted with permission.[62] Copyright 2013, American Chemical Society.

(d-e) Design of linkers by stepwise chemical functionalization. (d) Illustration of transformation from PCN-700 to PCN-700-AB by sequential installation of Brønsted acid- and base-based linkers. (e) Nitrogen isotherms of PCN-700-B, PCN-700-AB, and PCN-700-MB (M = H_2TPDC-Me$_2$, 2′,5 -dimethylterphenyl-4,4′-dicarboxylate). Adapted with permission.[68] Copyright 2019, Chinese Chemical Society.

(f) Design of metal sites by precursor selection. Illustrations of diverse single component MOF series, $(M_3O)_2(TCPP-M)_3$, constructed by mixing five different SBUs and six different porphyrin linkers, as well as multivariate MOFs (MTV-MOFs) with mixed-metal SBUs. Adapted with permission.[71] Copyright 2016, American Chemical Society.
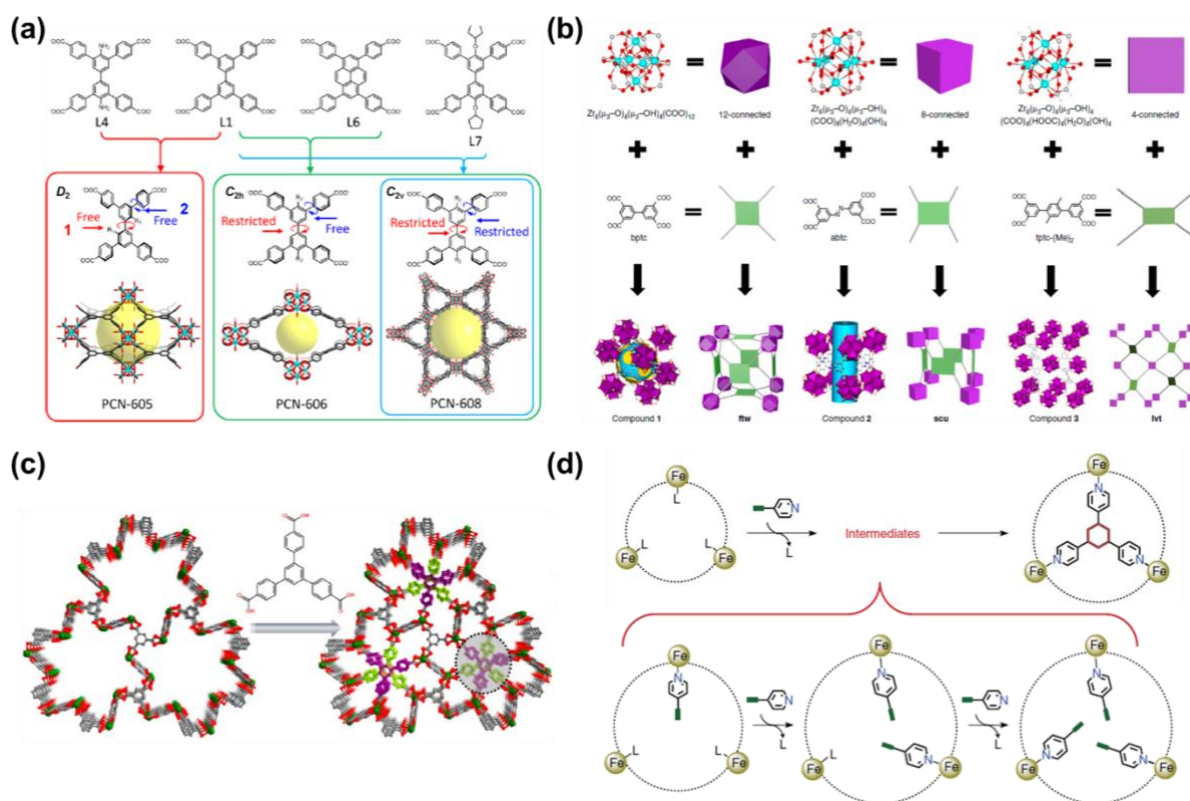
Figure 4. Micropores design for MOFs.

(a) Design of the conformations of linkers. Construction of specific topology MOFs by imparting substituents in the linkers at specific positions. Black: C; Red: O; Blue: Zr. Adapted with permission.[75] Copyright 2017, American Chemical Society.

(b) Control of the aspect ratio of linkers. Schematic demonstration of building Zr-MOFs with various topologies by connecting Zr_6 clusters with tetratopic organic ligands of different aspect ratios. Adapted with permission.[76] Copyright 2018, Nature Publishing Group.

(c) Pore space partition. Fabrication of CPM-12 by using size-complementary BTB and BTC ligands by one-pot synthesis. Adapted with permission.[78] Copyright 2017, American Chemical Society.

(d) Modification of metal SBUs. The proposed selective [2+2+2] coordination templated cyclotrimerization (CTC) reaction mechanism, where monomer molecules stepwise replace the terminal ligands (L) and are forced to gather in a close configuration suitable for the cyclotrimerization reaction. Adapted with permission.[81] Copyright 2015, Nature Publishing Group.
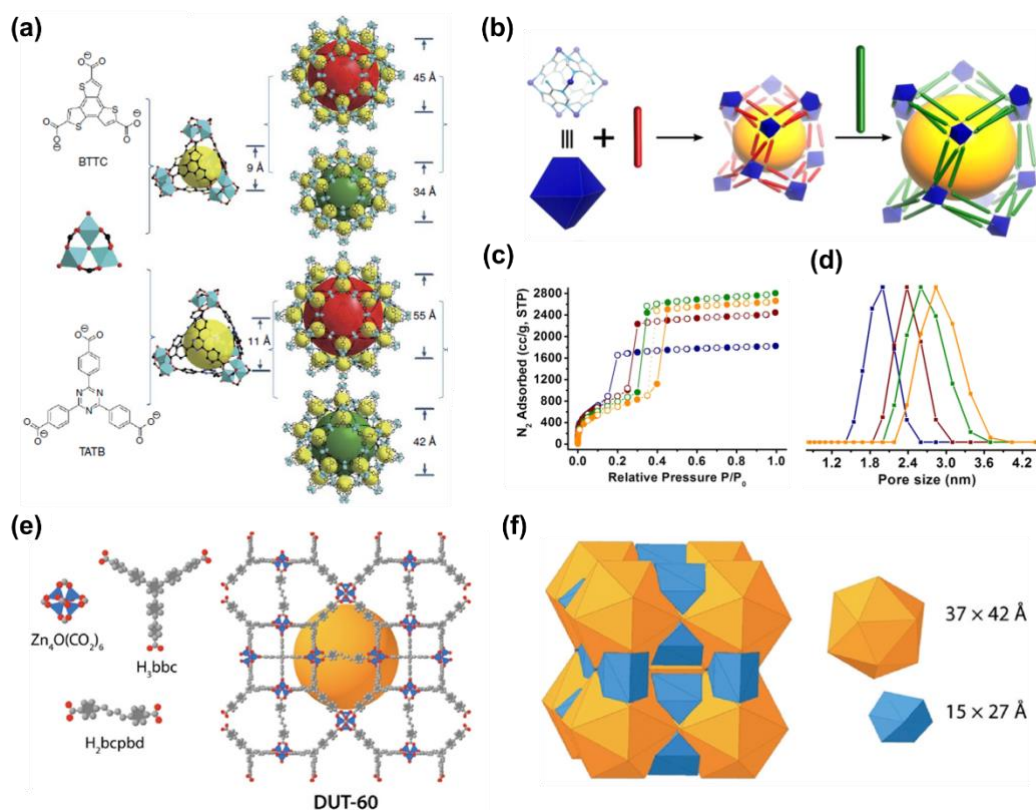
Figure 5. Mesopores design for MOFs by linker design.

(a) Linker elongation. Structure illustrations of PCN-332 and PCN-333, by linking trivalent metal species (Al, Fe, V, Sc, In) with ligands of BTTC (C_{3h} symmetry) and TATB (D_{3h} symmetry). Adapted with permission.[85]Copyright 2015, Nature Publishing Group.

(b-d) Linker exchange. (b) Scheme of pore expansion, where the synthesized Bio-MOF-101 is converted to bio-MOF-100 via ligand exchange with BPDC. (c-d) Nitrogen adsorption isotherms and normalized pore size distribution of bio-MOF-101 (navy), bio-MOF-100 (red), bio-MOF-102 (green), and bio-MOF-103 (orange) at 77 K. Adapted with permission.[88] Copyright 2013, American Chemical Society.

(e-f) Mixed linkers design. Mesoporous DUT-60 framework is fabricated by linking $Zn_4O(CO_2)_6$ clusters with mixed ditopic ligands (bcpbd) and tritopic ligands (bbc). Adapted with permission.[11] Copyright 2018, Wiley-VCH.
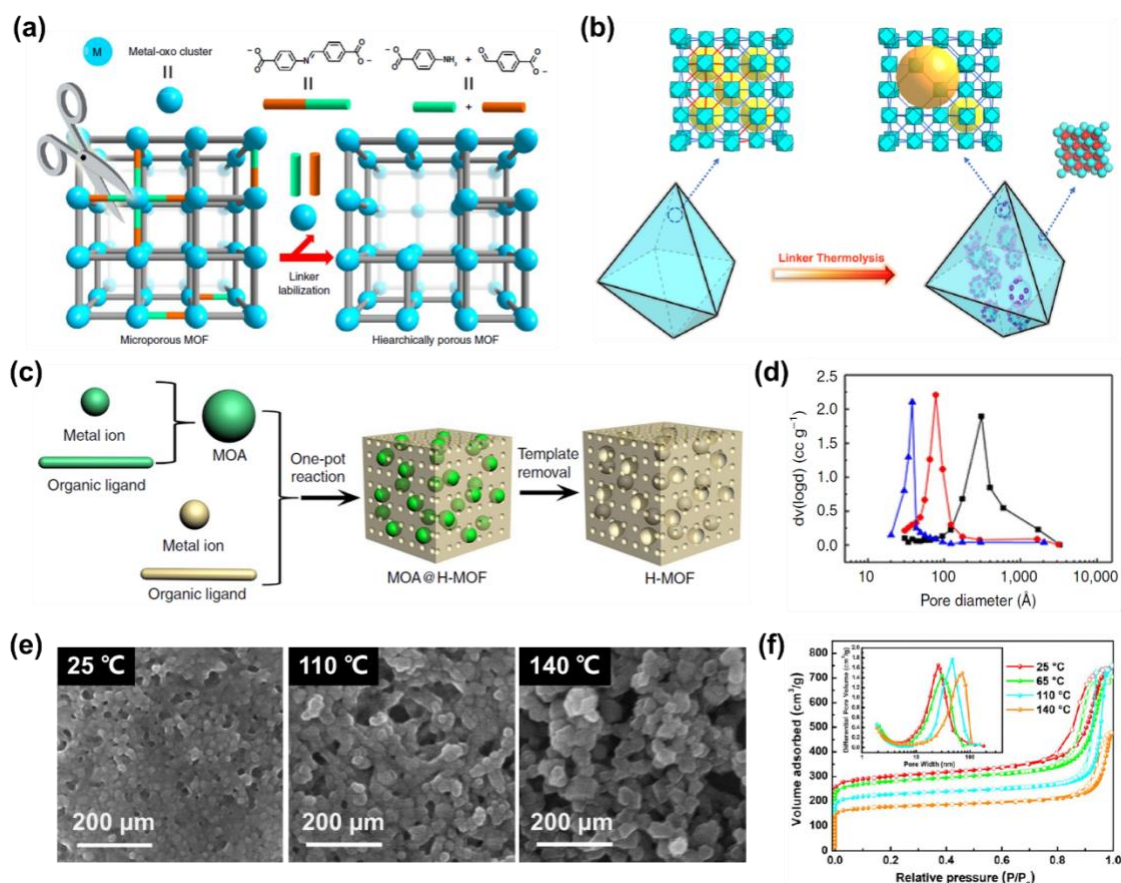
Figure 6. Mesopores design for MOFs by defect engineering, templating, and controlled assembly.

(a) Defect engineering by chemical labilization. Hierarchically porous MOFs have been developed by creating original MOFs with pro-labile linkers, then those linkers have been removed by acid treatment to introduce defects. Adapted with permission.[93] Copyright 2017, Nature Publishing Group.

(b) Defect engineering by controlled thermolysis. Demonstration of a multivariate MOF, which is built from ordinary and thermal-sensitive linkers, is converted into metal oxides@hierarchically porous MOFs through controlled linker thermolysis. Adapted with permission.[92] Copyright 2018, American Chemical Society.

(c-d) Templating methods. (a) Schematic representation of creating hierarchically-structured MOFs (UiO-66 (Zr)) by using an unstable MOF (MOF-5) as dynamic chemical template. (b) Pore size distribution of resulting MOFs, with addition of different amount of template precursors (*i.e.*, nanosized MOF-5), 1 ml (black curve), 2 ml (red curve) and 3 ml (blue curve). Adapted with permission.[97] Copyright 2015, Nature Publishing Group.

(e-f) Controlled assembly methods. (a) SEM images and (b) nitrogen adsorption isotherms (inset are pore size distribution) of the mesoporous Cu-BTC-n MOFs prepared at indicated temperatures. Adapted with permission.[99] Copyright 2016, American Chemical Society.
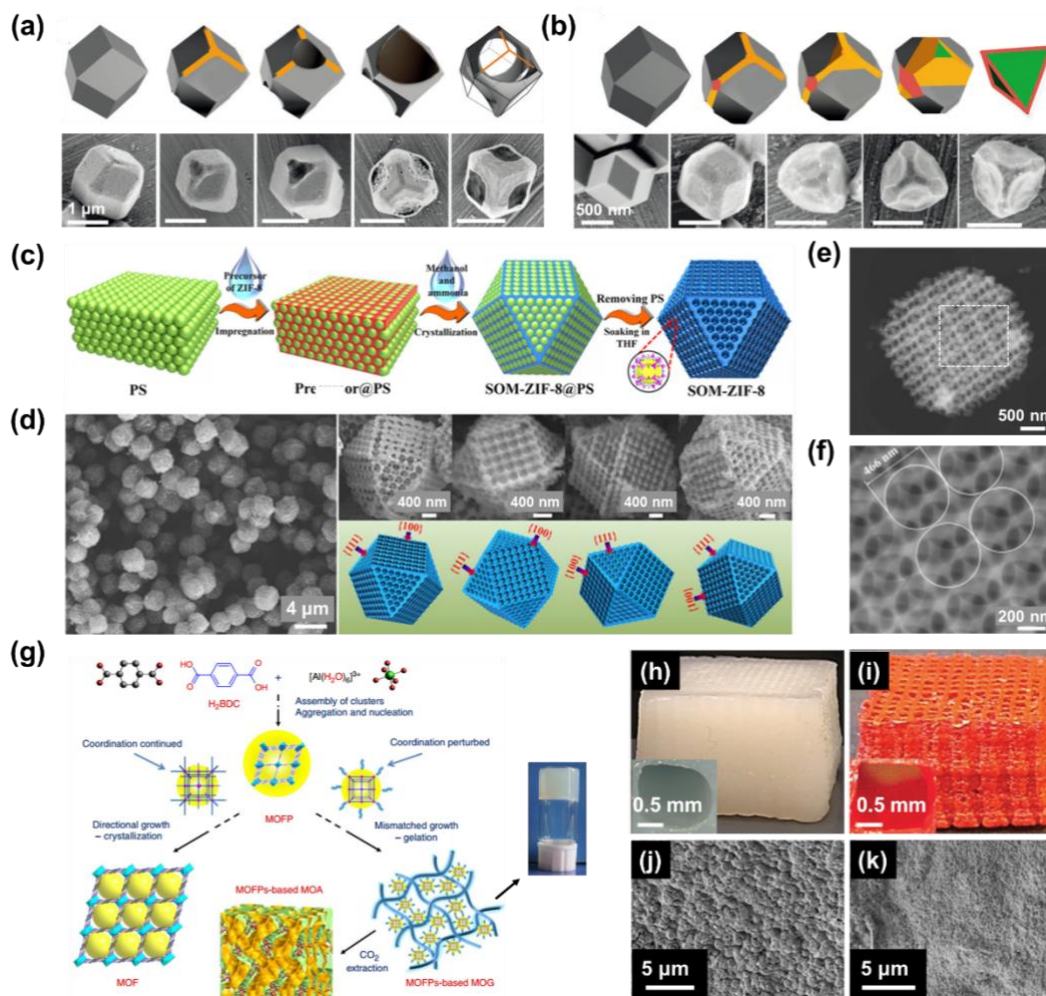
Figure 7. Macropores design for MOFs.

(a-b) Defect engineering method. Illustration and corresponding FE-SEM images (ZIF-67 for (a) and ZIF-8 for (b)) of the change in crystal morphology during the etching of rhombic dodecahedral crystals, where etchant solutions at (e) pH = 2.5 and (f) pH = 2.5 have been used. Adapted with permission.[100] Copyright 2015, Wiley-VCH.

(c-f) Templating method by using polystyrene (PS) spheres as templates. (c) Schematic representation of the PS-templating synthesis of single-crystal ordered macropore ZIF-8 (SOM-ZIF-8) crystals. (d) SEM images of SOM-ZIF-8 crystals, and (e-f) HAADF-STEM images of a SOM-ZIF-8 crystal with a macropore size of 470 nm. Adapted with permission.[106] Copyright 2018, American Association for the Advancement of Science.

(g) Controlled assembling to yield aerogels. Schematic illustration of synthesis of different-form MIL-53(Al) MOFs by using microporous MOF particles (MOFPs) at different reaction conditions, as well as a photograph of the resulting aerogel. Adapted with permission.[116] Copyright 2013, Nature Publishing Group.

(h-k) 3D printing method. (h-i) Digital photograph and (j-k) SEM images of 3D-printed ZIF-8@TOCNF (CelloZIF8)) and Curcumin-ZIF-8@TOCNF (CelloZIF8-Cur), respectively. Adapted with permission.[118] Copyright 2018, Wiley-VCH.
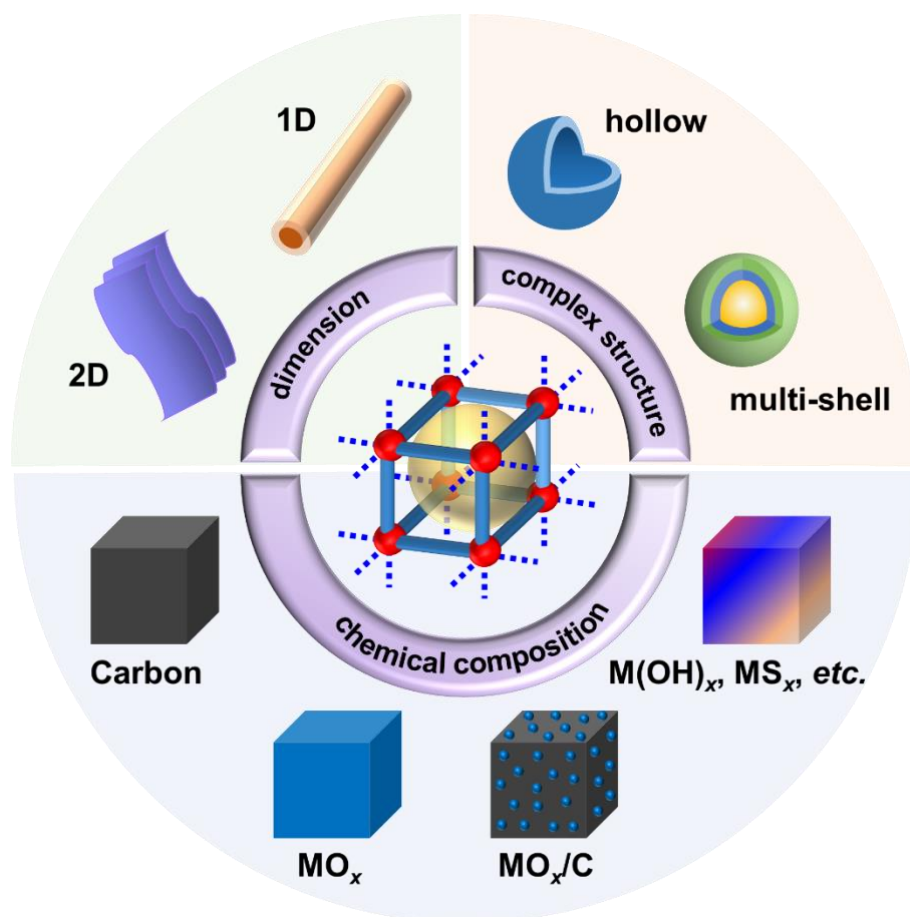
Figure 8. An overview of pore architecturing strategies for MOF-derived materials.
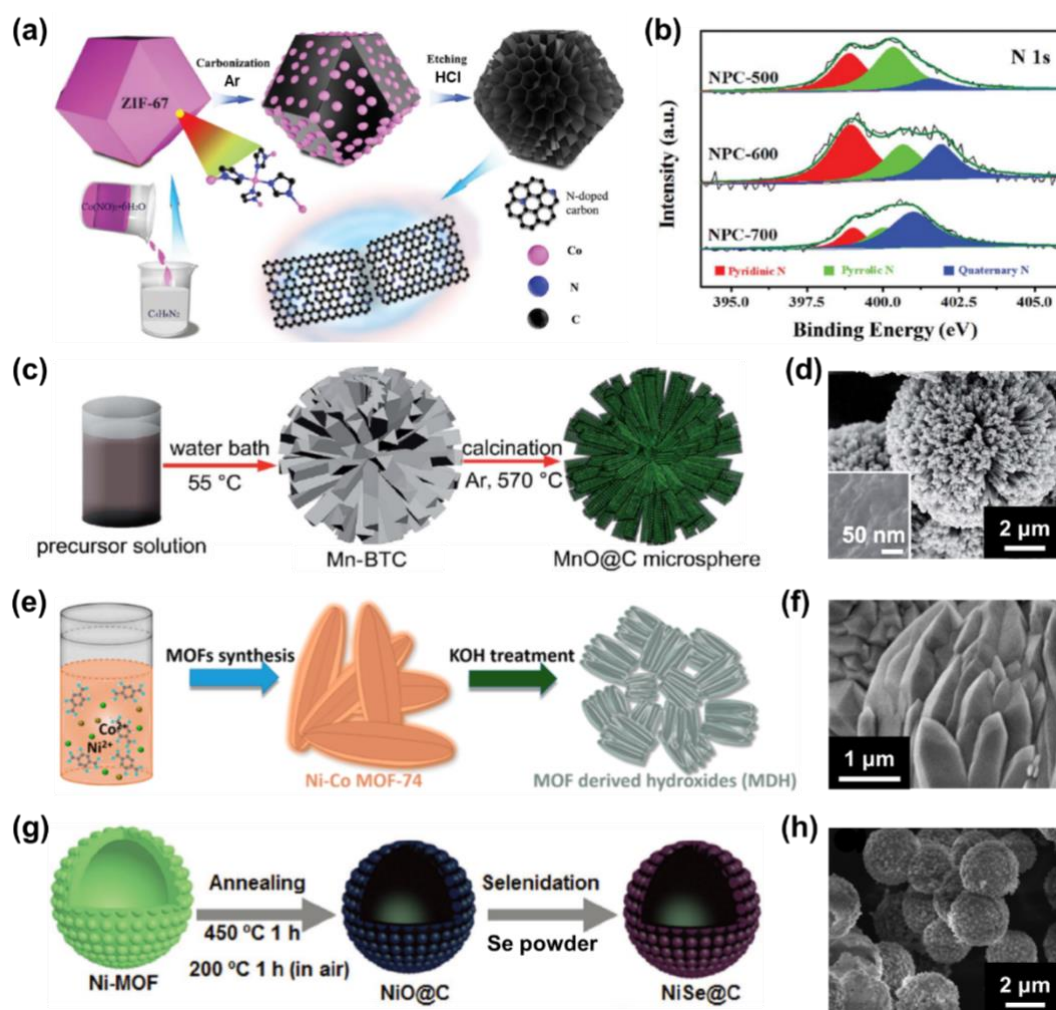
Figure 9. Pore chemistry design of MOF-derived materials.

(a-b) N-doped porous carbon (NPC). (a) Schematic illustration of the synthesis process and (b) the XPS N 1s spectra of NPC-500, NPC-600 and NPC-700. Adapted with permission.[132] Copyright 2018, Royal Society of Chemistry.

(c-d) MnO@C hierarchical microspheres. (c) Schematic illustration of the synthesis process and (d) the corresponding SEM images. Adapted with permission.[144] Copyright 2017, Royal Society of Chemistry.

(e-f) Ni-Co-based double hydroxide (Ni−Co MDH). (e) Schematic illustration of the synthesis process and (f) the corresponding SEM images of 65Ni-MDH. Adapted with permission.[150] Copyright 2017, American Chemical Society.

(g-h) NiSe@C hollow microspheres. (g) Schematic illustration of the synthesis process and (h) the corresponding SEM image. Adapted with permission.[30] Copyright 2018, Wiley-VCH.
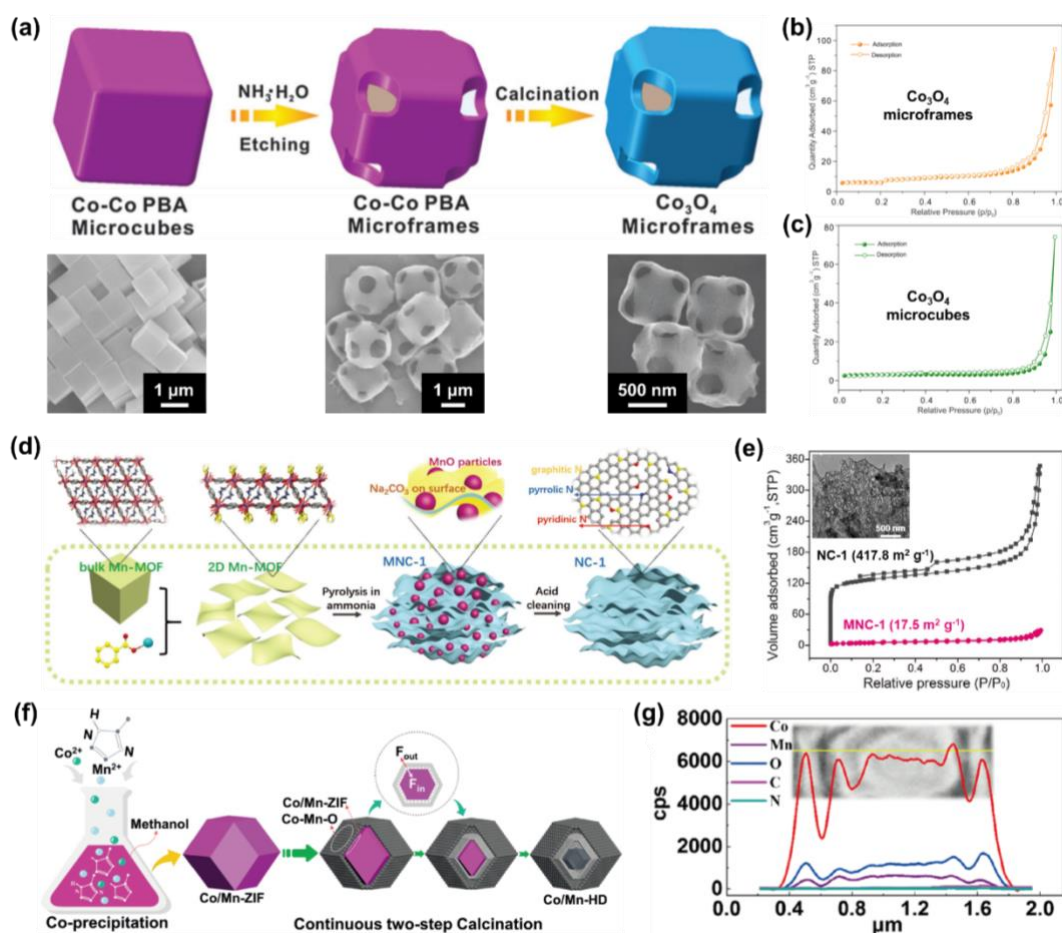
Figure 10. Pore structure design for MOF-derived materials.

(a-c) Macroporous Co_3O_4 microframes. (a) Schematic illustration of the synthesis process and the corresponding SEM images. Nitrogen adsorption isotherms of (b) Co_3O_4 microframes and (c) microcubes. Adapted with permission.[251] Copyright 2016, Royal Society of Chemistry.

(d-e) N-doped wrinkled carbon foils (NC-1). (d) The schematic fabrication process, where 2D Mn-MOF has been pyrolyzed in ammonia atmosphere to yield Na and Mn components/N-rich carbon foil (MNC-1), then has been transformed to NC-1 by has beenhing with acid solution. (e) Nitrogen adsorption–desorption isotherms of NC-1 and MNC-1. Inset shows the TEM image of NC-1. Adapted with permission.[134] Copyright 2018, Wiley-VCH.

(f-g) Triple-shelled manganese-cobalt oxide hollow dodecahedra (Co/Mn-HD). (f) The synthesis mechanism and (g) the line scanning of the Co/Mn-HD (inset shows the STEM image). Adapted with permission.[120] Copyright 2019, Wiley-VCH.
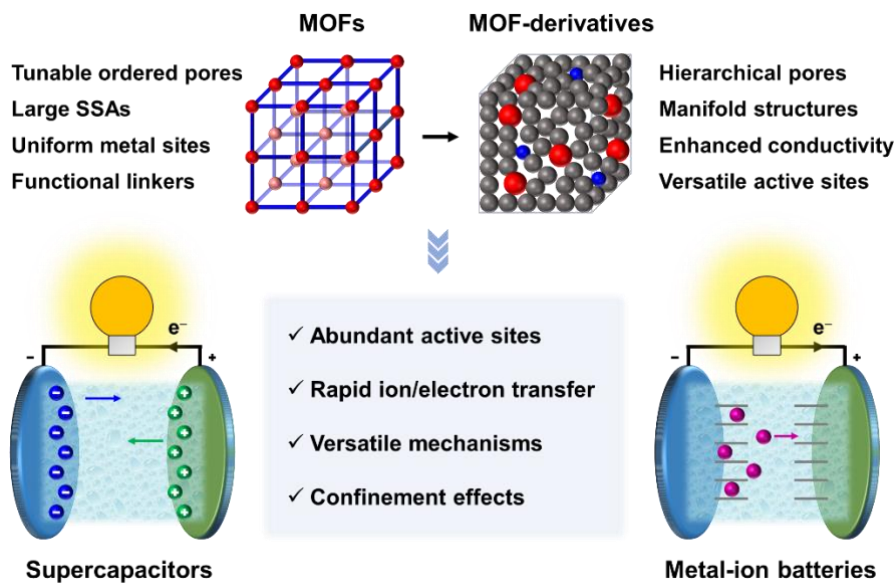
Figure 11. Advantages of MOF-based materials for supercapacitors and metal-ion batteries.
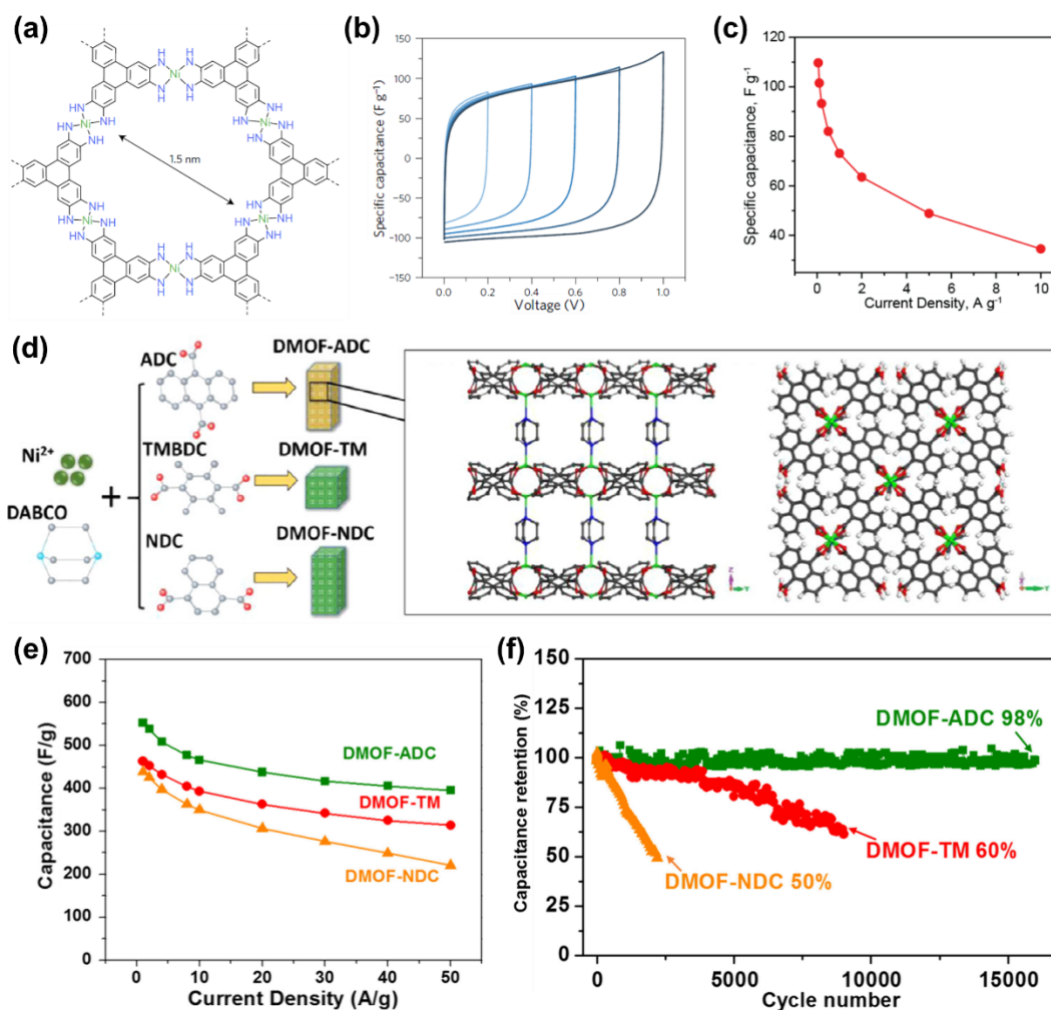
Figure 12. Tailoring pore chemistry of MOFs for supercapacitors.

(a-c) Increasing the conductivity with highly-conjugated backbones. (a) The molecular structure of Ni$_3$(HITP)$_2$, (b) Cyclic voltammetry (scan rate of 10mV s-1) and (c) rate performance of Ni$_3$(HITP)$_2$-based electrodes performed in a symmetrical supercapacitor. Adapted with permission.[54] Copyright 2017, Nature Publishing Group.

(d-f) Enhancing the stability by tuning the polarity of groups on linkers. (d) Schematic illustration of the fabrication process of pillared Ni-DMOFs and the corresponding wireframe views. (e) Rate performance of the discharge capacity and (f) cycling stability (at 10 A g^{-1}) of various Ni-DMOF electrodes based on indicated linkers (*i.e.*, ADC, TM, and NDC). Adapted with permission.[172] Copyright 2016, Elsevier.
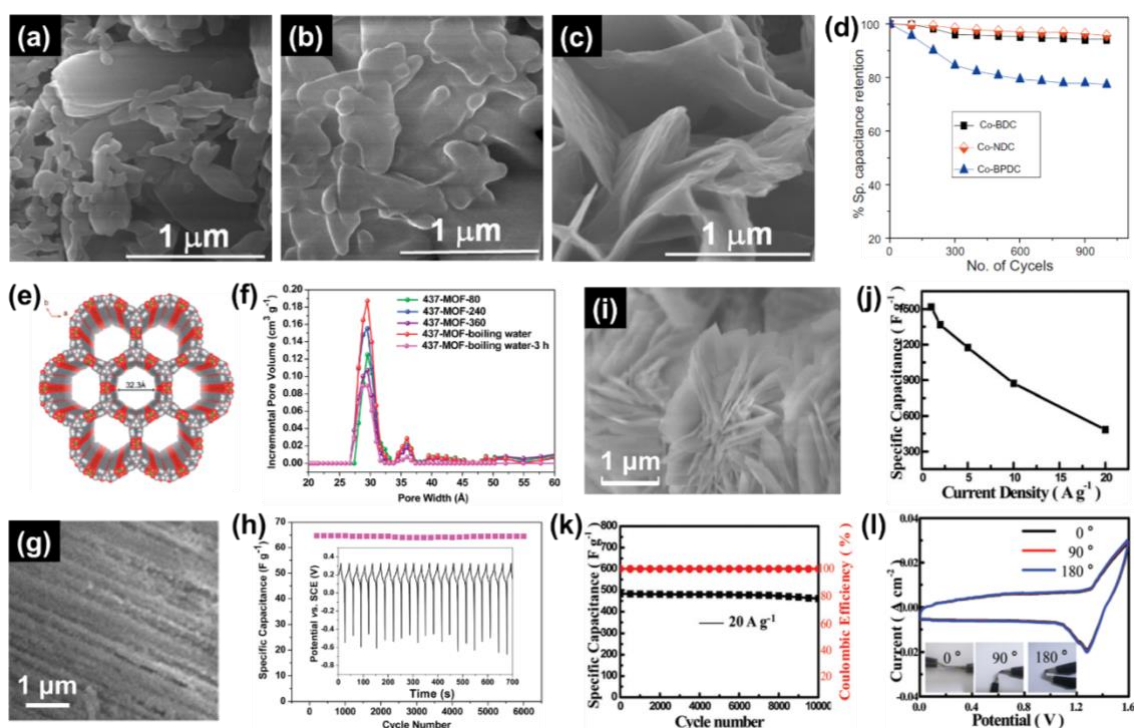
Figure 13. Tailoring pore structure of MOFs for supercapacitors.

(a-d) Tuning the pore structures by adjusting the length of linkers. (a-c) SEM images of (a) Co-BDC, (b) Co-NDC, and (c) Co-BPDC. (d) Cycling performance supercapacitor electrodes based on indicated MOFs at 100 mV-1 in 0.5 M LiOH aqueous solutions. Adapted with permission.[174] Copyright 2013, Elsevier.

(e-h) Utilizing mesoporous MOFs. (e) Molecular structure of {[In(BTTB)$_{2/3}$(OH)](NMF)$_5$(H$_2$O)$_4$}$_n$ (437-MOF) with 1-D hexagonal channels (diameter of *ca.* 3 nm). (f) Pore size distribution plots of 437-MOFs activated at different conditions. (g) The SEM image of 437-MOF-boiling water. (h) (a) Charge/discharge cycling test of 437-MOF electrode at 4 A g-1 (inset: charge/discharge cycles of the first and last 20 cycles). Adapted with permission.[176] Copyright 2014, Royal Society of Chemistry.

(i-l) MOFs with hybrid-dimensional structures. (i) The SEM image of a layered gear-like Ni-TDA MOF. (j) Rate performance and (k) charge/discharge cycling performance (20 A g^{-1}) of Ni-TDA MOF electrodes. (l) CV curves of a flexible solid-state asymmetric supercapacitor

assembled from Ni-TDA MOF and activated carbon under different bending modes at 10 mA cm^{-2}. Adapted with permission.[51] Copyright 2020, Royal Society of Chemistry.
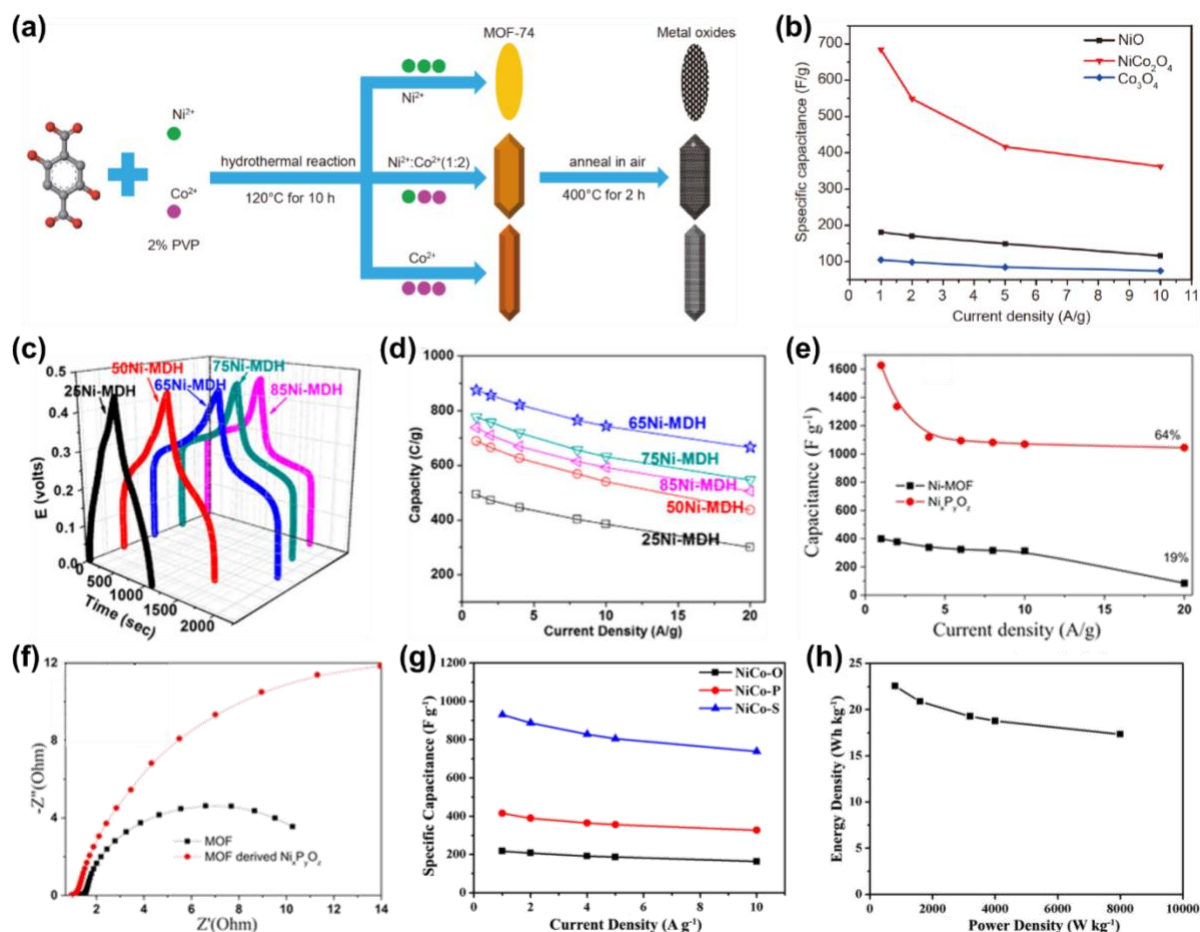
Figure 14. Tailoring pore chemistry of MOF-derived materials for supercapacitors.

(a-b) Schematic illustration for synthesizing the MOF-74 precursors and the corresponding derived metal oxides (NiO, NiCo$_2$O$_4$, and Co$_3$O$_4$) and their rate performance. Adapted with permission.[186] Copyright 2020, Springer.

(c-d) Galvanostatic charge–discharge curves (at 1 A g^{-1}) and rate performance of MDH electrodes with different initial Ni(II) to Co(II) ratios (25%, 50%, 65%, 75%, and 85% Ni). Adapted with permission.[150] Copyright 2017, American Chemical Society.

(e-f) Rate performance and the Nyquist plots of pristine Ni-MOF and MOF-derived Ni$_x$P$_y$O$_z$ electrodes. Adapted with permission.[188] Copyright 2016, Wiely-VCH.

(g) Rate performance of NiCo-O, NiCo-P and NiCo-S electrodes, and (h) Ragone plots of the NiCo-S //activated carbon hybrid supercapacitor. Adapted with permission.[152] Copyright 2019, Wiely-VCH.
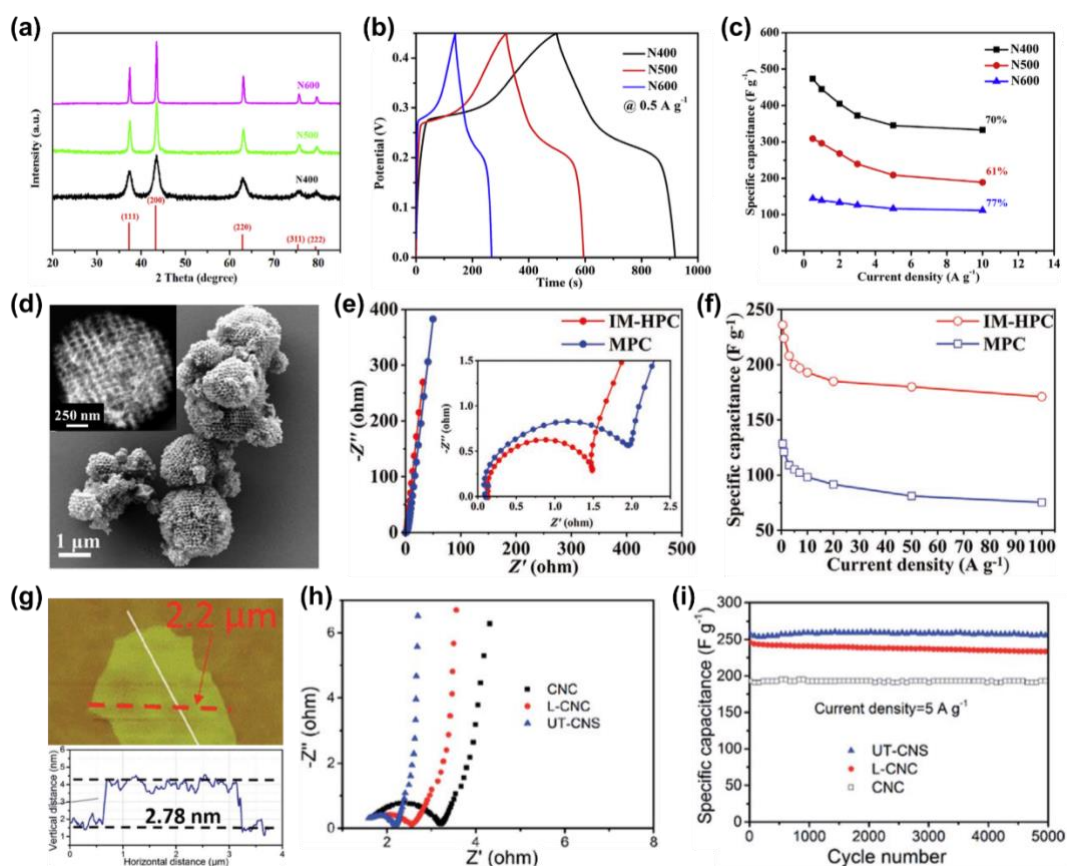
Figure 15. Tailoring pore structures of MOF-derived materials for supercapacitors.

(a-c) XRD patterns, charge-discharge curves, and rate performance of NiO nanospheres synthesized at different temperatures (400, 500, and 600°C). Adapted with permission.[189] Copyright 2018, Elsevier.

(d) SEM image and HAADF-STEM image (inset) of IM-HPC. (e-f) Nyquist plots and rate performance of IM-HPC and MPC. Adapted with permission.[160] Copyright 2020, Wiley-VCH.

(g) AFM image of the UT-CNSs. (h-i) Nyquist plots and long-term cycling performance of the UT-CNS, L-CNC, and CNC electrodes at the current density of 5 A g^{-1}. Adapted with permission.[161] Copyright 2018, Royal Society of Chemistry.
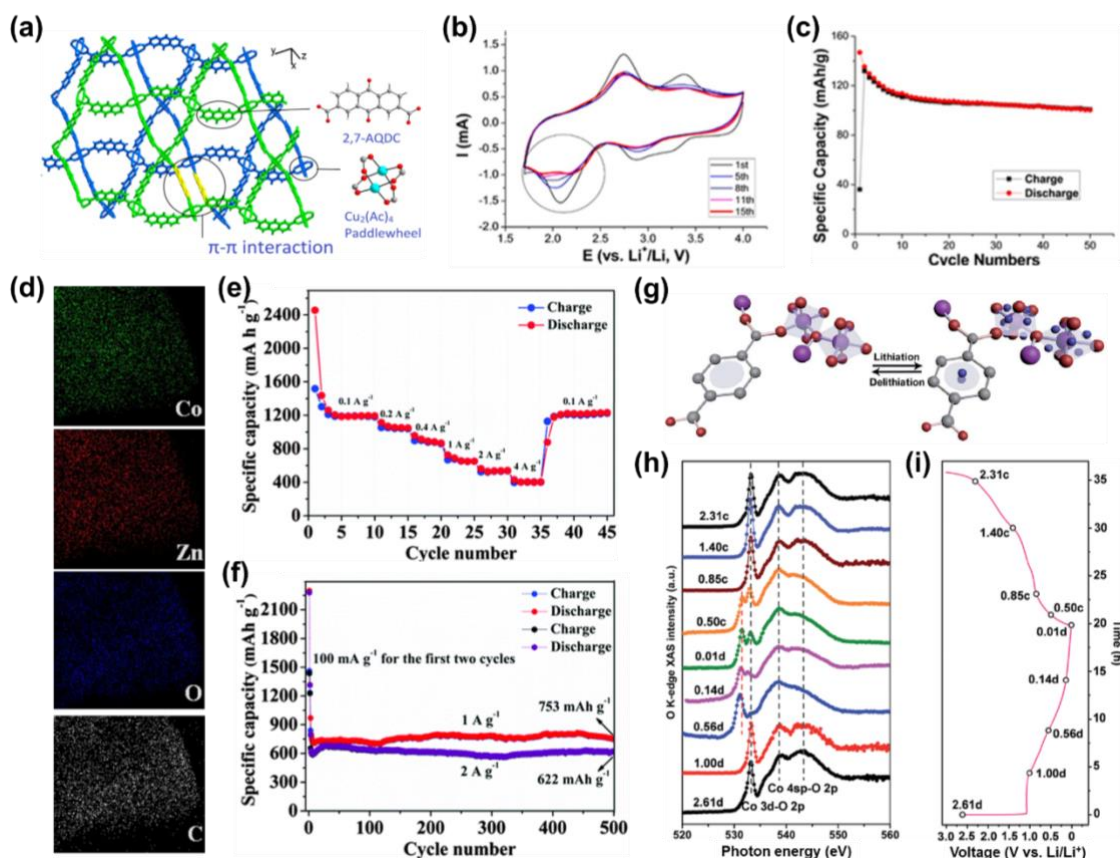
Figure 16. Tailoring pore chemistry of MOFs for metal-ion batteries.

(a-c) MOFs featuring both reversibly redox-active metal clusters and ligands for LIB cathodes. (a) Top view of Kagome lattice type structure of Cu (2,7-AQDC) (2,7-H_2AQDC = 2,7-anthraquinonedicarboxylic acid). (b) CV curves of the Cu (2,7-AQDC) electrode. Two isolated reversible peaks at 3.1 and 2.4 V indicated the redox reactions of metal clusters (Cu(I)/Cu(II)) and anthraquinone groups, respectively. (c) Charge/discharge cycling stability of Cu (2,7-AQDC) electrode. Adapted with permission.[195] Copyright 2014, American Chemical Society.

(d-f) Bimetallic MOFs for LIB anodes. (d) EDX mappings of Co-Zn-MOFs. (e) Rate performance and (f) cycling performance of the electrode. Adapted with permission.[215] Copyright 2016, Royal Society of Chemistry.

(g-j) Organic-moiety-dominated Li$^+$ intercalation for LIB anodes. (g) Conceptual scheme of the intercalation/deintercalation mechanism of the S–Co-MOF. Color scheme: Co-purple; O-claret-red; C-gray; Li-blue. (h) Ex situ O K-edge soft X-ray absorption spectroscopy spectra of the S–Co-MOF electrodes cycled to different states-of-charge. (i) The electrochemical profile of S–Co-MOF/Li cycled at 0.1 A g^{-1}. Adapted with permission.[197] Copyright 2016, Royal Society of Chemistry.
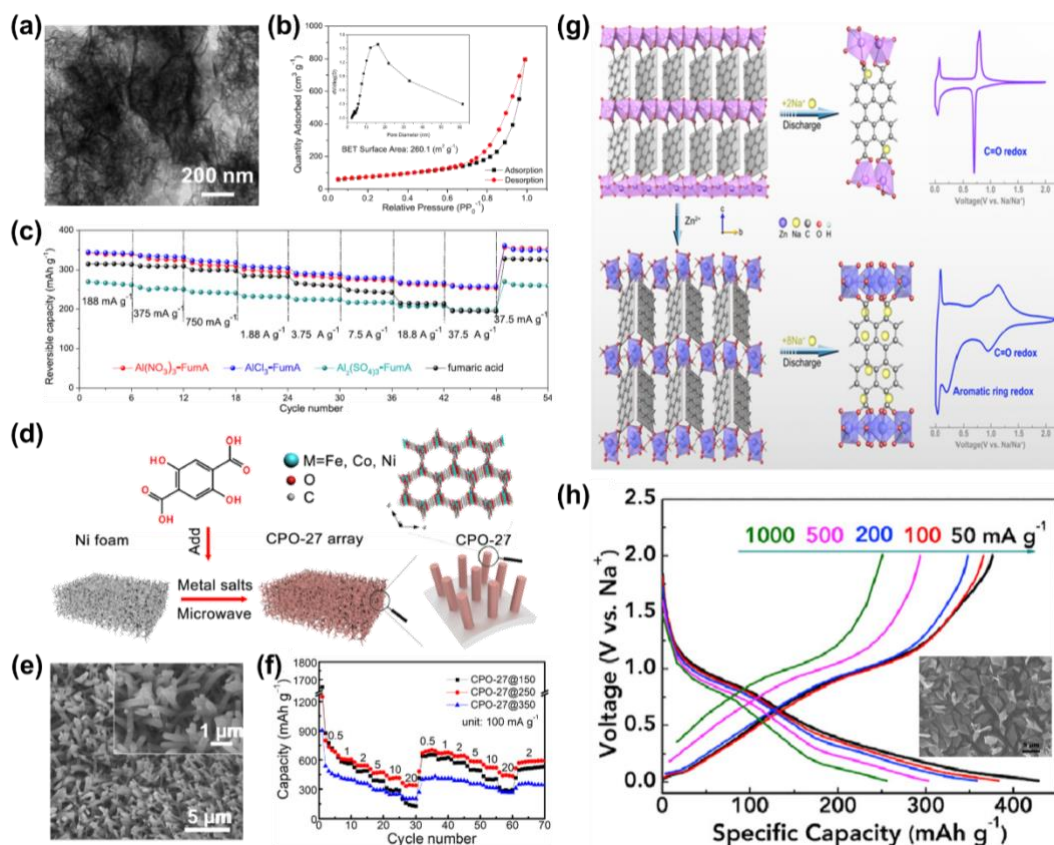
Figure 17. Tailoring pore structures of MOFs for metal-ion batteries.

(a-c) MOFs with abundant mesopores for LIB anodes. (a) TEM image and (b) Nitrogen sorption isotherms (the inset shows the PSD curve) of $AlCl_3$-FumA. (c) Rate performance of various Al-FumA as anodes, with a discharge at 37.5 mA g^{-1} and various charge current densities. Adapted with permission.[225] Copyright 2017, Elsevier.

(d-f) Decorating MOFs on metal foams for LIB anodes. (d) Schematic illustration for the preparation of CPO-27 arrays on nickel foams. (e) The SEM image of CPO-27 grown on the Ni foam substrate annealed at 250 °C (CPO-27@250). (f) Rate performance of various Ni-foam-supported CPO-27 annealed at different temperatures. Adapted with permission.[226] Copyright 2019, Elsevier.

(g-h) Design of 3D wavy-layered MOFs for SIB anodes. (g) Schematic representation of exposing aromatic rings as additional active sites accessible to Na^+ by designing a MOF (*i.e.*, Zn-PTCA) with wavy-layered 3D framework structure. (h) Charge–discharge profiles of Zn-PTCA electrode at different current densities. Adapted with permission.[233] Copyright 2018, Elsevier.
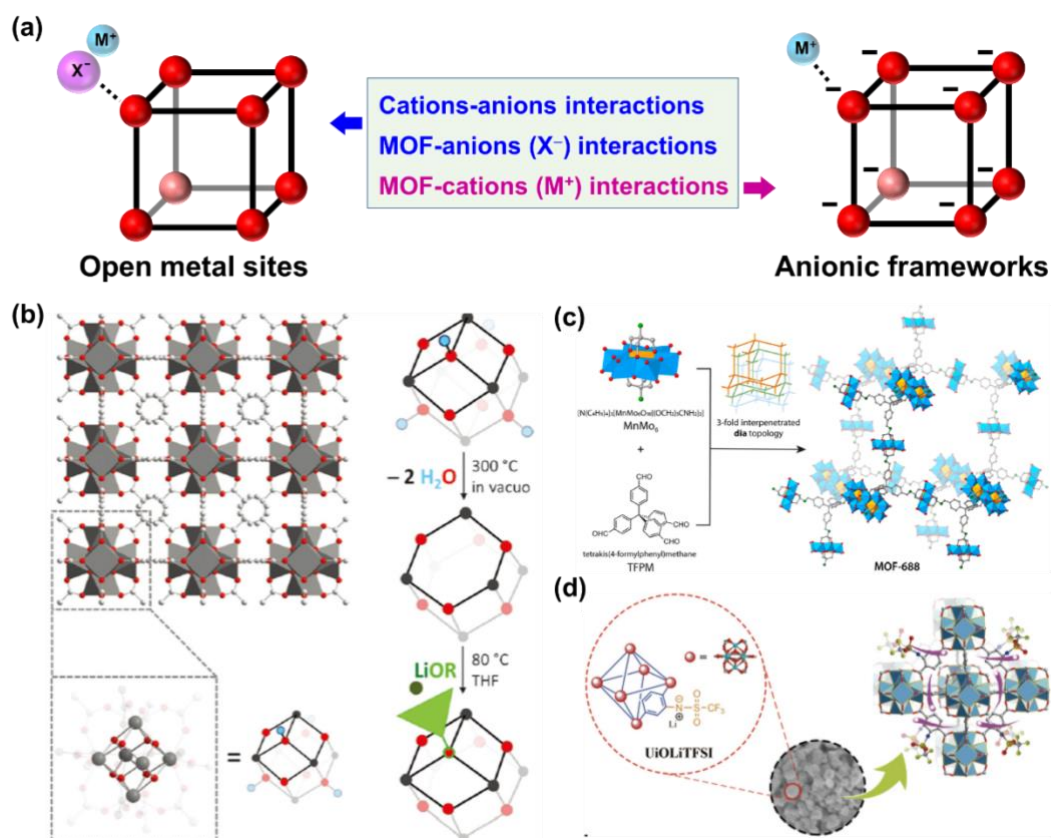
Figure 18. Neat MOFs for solid-state electrolytes.

(a) Schematic demonstration of two main strategies for design MOF-based solid-state electrolytes. M+ and X- denote metal cations and counter-anions, respectively.

(b) Crystal structure of UiO-66 (left) and the schematic insertion process (right), which involves sequential dehydration of the cluster core and subsequent grafting of lithium tert-butoxide. Adapted with permission.[236] Copyright 2013, Wiley-VCH.

(c) Synthetic strategy and structure illustration of MOF-688. Adapted with permission.[242] Copyright 2019, American Chemical Society.

(d) Schematic illustration of the structure and ion transport mechanism of UiO-66-NSO2CF3Li. Adapted with permission.[243] Copyright 2019, American Chemical Society.
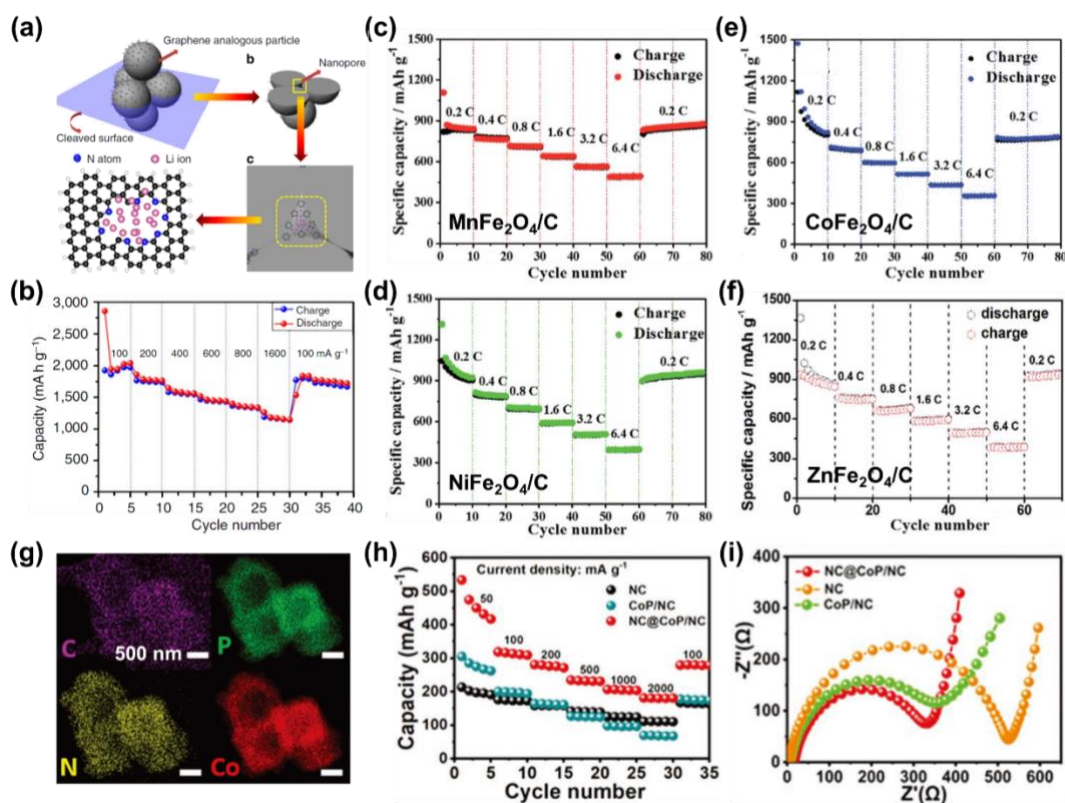
Figure 19. Tailoring pore chemistry of MOF-derived materials for metal-ion batteries.

(a-b) Nitrogen-doped porous carbons for LIB anodes. (a) Schematic representation of extra Li storage in N-doped graphene analogous particles. (b) Rate performance of a N-C-800 electrode. Adapted with permission.[140] Copyright 2014, Nature Publishing Group.

(c-f) Bimetal oxides/carbon for LIB anodes. Rate performance of (c) $MnFe_2O_4/C$, (d) $NiFe_2O_4/C$, (e) $CoFe_2O_4/C$, and (f) $ZnFe_2O_4/C$ spindles. Adapted with permission.[28] Copyright 2017, Royal Society of Chemistry.

(g-i) Metal phosphides/carbon for PIB anodes. (g) Elemental mappings of nitrogen-doped porous carbon confined CoP polyhedron (NC@CoP/NC). (h) Rate performance and (i) EIS spectra of NC, CoP/NC, and NC@CoP/NC electrodes. Adapted with permission.[153] Copyright 2020, Wiley-VCH.
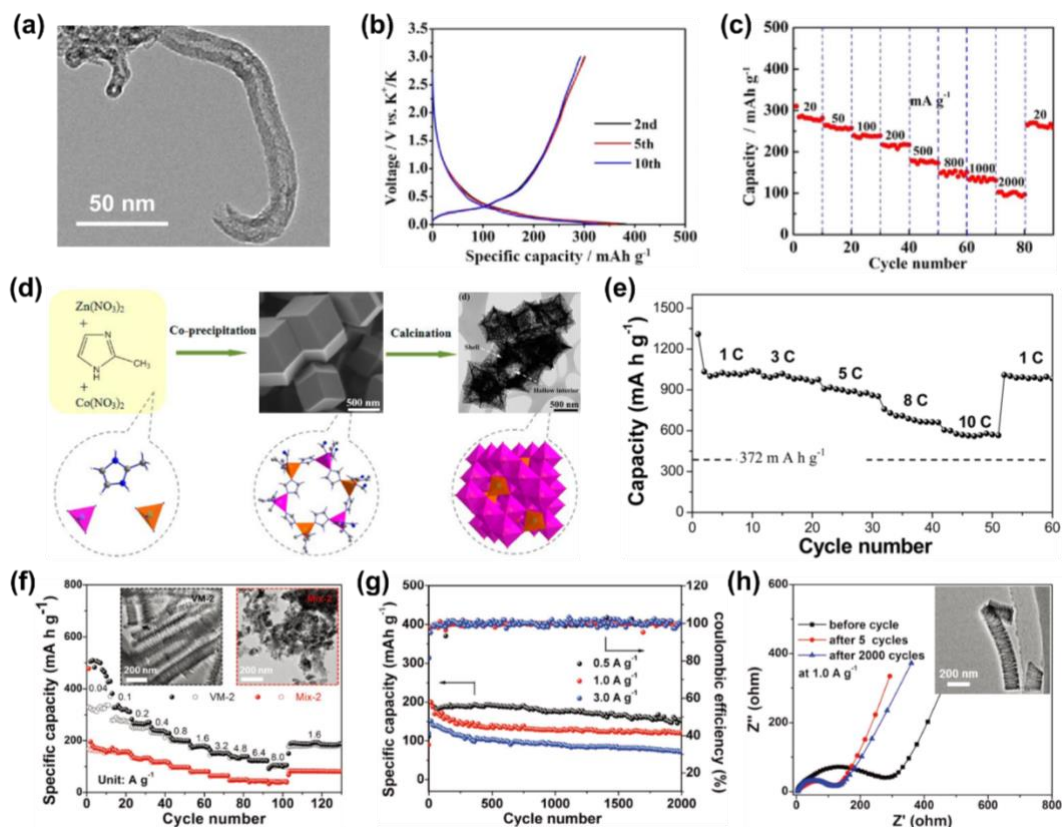
Figure 20. Tailoring pore structures of MOF-derived materials for metal-ion batteries.

(a-c) Nitrogen-doped carbon nanotubes (NCNTs) for PIB anodes. (a) TEM images of NCNTs. (b) Galvanostatic charge/discharge profiles (at 50 mA g-1) and (c) rate performance of NCNT electrodes for potassium ions. Adapted with permission.[263] Copyright 2018, Wiley-VCH.

(d-e) Hollow-structured metal oxides for LIB anodes. (d) Schematic illustration for preparing bimetallic ZIFs and their conversion to spinel $Zn_xCo_{3-x}O_4$ hollow polyhedra. (e) Rate performance of $Zn_xCo_{3-x}O_4$ hollow polyhedra as electrodes. Adapted with permission.[127] Copyright 2014, American Chemical Society.

(f-h) Vanadium oxide/porous carbon nanorods with oriented slit-like 2D pores for SIB anodes. (f) Rate performance and TEM images (inset) of VM-2 and Mix-2. (g) Cycling performance and (h) EIS spectra of VM-2 samples before cycle, after 5 and 2000 cycles at 1.0 A g−1. Inset shows TEM image of VM-2 after 2000 cycles. Adapted with permission.[271] Copyright 2018, Wiley-VCH.
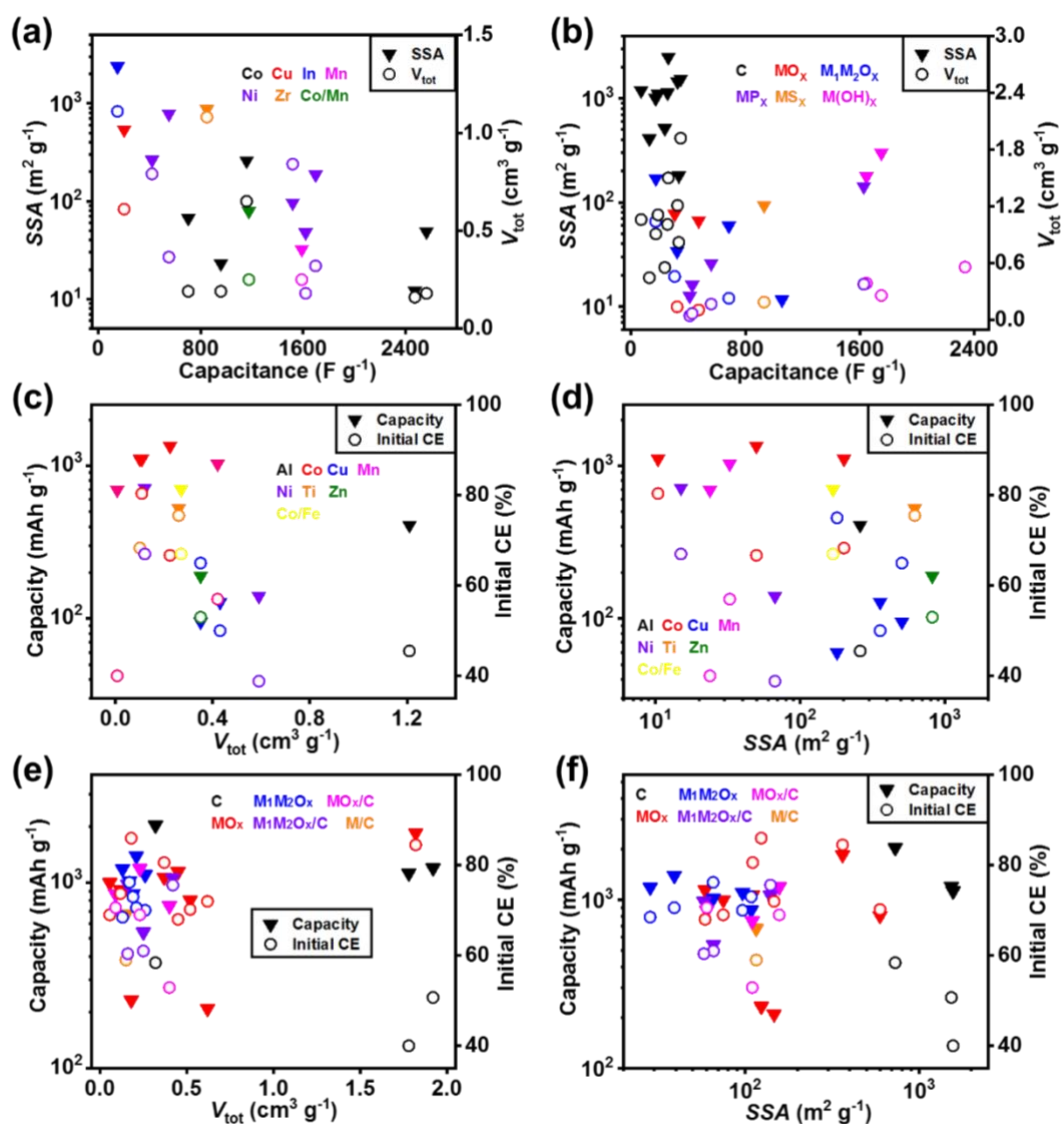
Figure 21. The correlations of structure/composition of (a,c,d) MOFs and (b,e,f) their derivatives to their performance for (a-b) supercapacitor electrodes and (c-f) LIB anodes. In figure a, c, and d, different colors denote MOFs bearing various metals. In figure b, e, and f, different colors denote MOF-derivatives of different kinds (C-carbon, M-metal, MO_x-single-metallic oxides, $M_1M_2O_x$-bimetallic oxides).

Table 1. Summary of pore structure engineering for MOFs.

Pore types	Methods	Ref
Micropores	*Linker design* (aspect ratios, substitution, linker exchange)	[75-76, 79]
	Metal center design	[80-81]
	Pore partition	[77]
Mesopores	*Linker design* (linker elongation, mixed linkers, linker exchange)	[11, 85, 87-89]
	Templating (surfactants, block copolymers, self-template)	[95, 97, 99]
	Defect engineering (chemical etching, thermolysis)	[90-93]
	Controlled assembly (assembly of nanosized MOFs, assembly in mixed solvents)	[94, 98]
Macropores	*Templating* (Ni foams, Cu foams, polymer sponges)	[102-105]
	Templating-etching (polystyrene nanospheres)	[106]
	Defect engineering (acid etching)	[100-101]
	Assemble to aerogels	[113-116]
	3D printing	[117-119]

Table 2. Summary of synthesis strategies for MOF-derivatives.

MOF-derivatives	Methods	Ref
Carbon	*Annealing* (550−1000ºC in N_2, Ar or vacuum)	[135-137]
	Annealing-etching (800ºC in Ar; HCl as etchant)	[138]
Doped Carbon	*Annealing* (1000ºC in H_2/Ar)	[133]
	Annealing-etching: Atmosphere (ammonia, H_2/Ar, Ar, Ar/ H_2O, or N_2), temperatures (600−1000ºC), etchants (HCl, HNO_3, or H_2SO_4)	[26, 139-141]
Metal oxides	*Annealing* (350−650ºC in air)	[120-125]
	Two-step annealing (300−500ºC in N_2 → 300−400ºC in air)	[126-130]
Metal hydroxide	*Hydrolysis* (in KOH or NaOH solutions)	[150]
Metal sulfide	*Annealing* (in air) → *Solvothermal reaction* (with thiourea)	[152]
Metal nitride	*Two-step annealing* (350−400ºC in air → 250−500ºC in NH_3)	[32-33]
Metal phosphide	*Two-step annealing* (300ºC in air → 300ºC in N_2 with NaH_2PO_2)	[154]
Metal / carbon	*Annealing* (600−800ºC in N_2)	[31, 149]
Metal oxides / carbon	*Annealing* (250−900ºC in air, N_2 or Ar)	[142, 145-148]
Metal sulfides / carbon	*Annealing* (550ºC in N_2 with sulfur powder)	[29]
Metal selenides / carbon	*Annealing* (600ºC in vacuum with Se powder)	[156]
Metal nitrides / carbon	*Annealing* (450ºC in N_2/NH_3)	[34]
Metal phosphides / carbon	*Two-step annealing* (500ºC in Ar → 350ºC in Ar with NaH_2PO_2)	[155]

Table 3. Summary of material parameters of MOF-based materials and their performance as supercapacitor electrodes.

Materials	V_{tot} (cm^3 g^{-1}) ^{a}	Pore size (nm)	SSA (m^2 g^{-1})	Electrolyte	Specific capacitance (F g^{-1})^b	Retention (%) / cycles	Ref
MOF Supercapacitors							
Co(μ-ox)(H$_2$O)$_2$	~0.19	3.6 & >10	67.2	2 M KOH	703 @ 1 A g^{-1}, 612 @ 10 A g^{-1}	94.3 / 1000	[52]
Co$_2$(OH)$_2$C$_8$H$_4$O$_4$	~0.18	broad	48.9	5 M KOH	2564 @ 1 A g^{-1}, 1164 @ 20 A g^{-1}	95.8 / 3000	[181]
Layered {[Co(HMT)(TFBDC)(H$_2$O)$_2$]·(H$_2$O)$_2$}$_n$	~0.16	<50	12.2	1 M KOH	2474 @ 0.5 A g^{-1}, 1024 @ 20 A g^{-1}	94.3 / 2000	[182]
Co-BDC NSs	~0.65	broad	260	3 M KOH	1159 @ 0.5 A g^{-1}, 1052 @ 5 A g^{-1}	96.7 / 6000	[180]
Co-BTC/D-E	0.19	broad	23.1	3 M KOH	958.1 @ 2 A g^{-1}, 627.6 @ 30 A g^{-1}	92.3 / 3000	[173]
Pillared Ni-DMOF-ADC	~0.365	–	783	2 M KOH	552 @ 1 A g^{-1}, 395 @ 50 A g^{-1}	>98 / 16000	[172]
Ni(HOC$_6$H$_4$COO)$_{1.48}$(OH)$_{0.52}$·1.1 H$_2$O NRs	~0.32	~3.2	186.8	6 M KOH	1698 @ 1 A g^{-1}, 838 @ 10 A g^{-1}	94.8 / 1000	[178]
2D Ni-HAB MOFs	~0.79	0.87 & >15	180–350	1 M KOH	420 @ 1 mV s^{-1}, 273 @ 100 mV s^{-1}	>90 / 12000	[53]
Zn-doped Ni-PTA (MOF-2)	~0.18	broad	47.9	6 M KOH	1620 @ 0.25 A g^{-1}, 854 @ 10 A g^{-1}	91 / 3000	[177]
Layered gear-like Ni-TDA	~0.84	~15	96.3	2 M KOH	1518.8 @ 1 A g^{-1}, 483.3 @ 20 A g^{-1}	95.5 / 10000	[51]
Cu–HHTP NW arrays on carbon fiber papers	~0.61	~1.8	540	3 M KCl	202 @ 0.5 A g^{-1}, 134 @ 10 A g^{-1}	80 / 5000	[171]
Mn-BDC	0.25	broad	32.3	1 M Na$_2$SO$_4$ 0.2 M K$_3$[Fe(CN)$_6$]	1590 @ 3 A g^{-1}	>82 / 3000	[175]
437-MOF (In)	1.11	2.8 & 3.6	2379	6 M KOH	150.2 @ 0.2 A g^{-1}, 56 @ 8 A g^{-1}	~100 / 6000	[176]
Co/Mn-ATPA	~0.25	<30	79.3	1 M KOH	1176.6 @ 3 mA cm^{-2}	85.3 / 5000	[274]
Hierarchical porous UiO-66 (Zr)	1.08	1–40	874	6 M KOH	849 @ 0.2 A g^{-1}, 237 @ 10 A g^{-1}	/	[170]
MOF-derivatives Supercapacitors							
NiO nanospheres N-400 (Ni-BDC)^c	~0.108	broad	66.8	3 M KOH	473 @ 0.5A g^{-1}, 332.8 @ 10 A g^{-1}	94 / 3000	[189]
NiO NPs (Ni$_3$(HCOO)$_6$)	~0.14	broad	34	6 M KOH	322 @ 1 A g^{-1}, 149 @ 40 A g^{-1}	~100 / 1000	[131]
Hollow NiCo$_2$O$_4$ nanowall arrays on carbon cloth CC@NiCo$_2$O$_4$ (NiCo-2-MIM)	–	–	11.6	2 M KOH	1055.3 @ 2.5 mA cm^{-2}, 483.3 @ 60 mA cm^{-2}	86.7 / 20000	[27]
ZnO/NiO MSs (ZnNi-BTC)	~0.91	7.5-25	170	3 M KOH	172.9 @ 0.5 A g^{-1}, 107.8 @ 3 A g^{-1}	97.4 / 2000	[187]
NiCo$_2$O$_4$ NPs (NiCo$_2$-MOF-74)	~0.23	2–20	59.6	1 M KOH	684 @ 0.5 A g^{-1}, 362.4 @ 10 A g^{-1}	86 / 3000	[186]
Co/Ni(OH)$_2$-3:1 NSs (CoNi-BTC)	~0.56	<5	–	6 M KOH	2335 @ 0.5 A g^{-1}, 1413 @ 20 A g^{-1}	52 / 2000	[190]

NiCo$_2$O$_4$/β-Ni$_x$Co$_{1-x}$(OH)$_2$/α-Ni$_x$Co$_{1-x}$(OH)$_2$ (CoNi-BTC)	~0.39	~12	178.3	6 M KOH	1646 @ 0.5 A g^{-1} 896 @ 20 A g^{-1}	90.7 / 10000	[190]
Ni$_{65}$Co$_{35}$-double hydroxides (NiCo-MOF-74)	~0.26	<10	299	2 M KOH	1750 @ 1 A g^{-1} 1332 @ 20 A g^{-1}	90.1 / 5000	[150]
NiCo-O (CoNi- MOF-74)	~0.46	broad	77.3	2 M KOH	305 @ 1 A g^{-1} 218 @ 10 A g^{-1}	90.5 / 10000	[152]
NiCo-P (NiCo-MOF-74)	~0.046	broad	12.6	2 M KOH	410 @ 1 A g^{-1} 323 @ 10 A g^{-1}	64.3 / 10000	[152]
NiCo-S (NiCo-MOF-74)	~0.19	broad	94.1	2 M KOH	930.4 @ 1 A g^{-1} 738.2 @ 10 A g^{-1}	70.5 / 10000	[152]
Single-shelled Zn-Co-S RDCs (CoZn-ZIF-8)	–	–	–	6 M KOH	685 @ 1 A g^{-1} 445 @ 1 A g^{-1}	81 / 10000	[193]
Double-shelled Zn-Co-S RDCs (CoZn-ZIF-8)	–	–	–	6 M KOH	1266 @ 1 A g^{-1} 720 @ 20 A g^{-1}	91 / 10000	[193]
Hollow CoP microcubes ([CH$_3$NH$_3$][Co(HCOO)$_3$])	~0.17	–	25.9	6 M KOH	560 @ 1 A g^{-1} 324 @ 20 A g^{-1}	91.2 / 10000	[194]
Solid CoP microcube ([CH$_3$NH$_3$][Co(HCOO)$_3$])	~0.07	–	16.1	6 M KOH	427.6 @ 1 A g^{-1} ~175 @ 20 A g^{-1}	80.2 / 10000	[194]
Hollow porous Ni$_x$P$_y$O$_z$ (Ni-BTC)	0.379	broad	142.2	2 M KOH	1627 @ 1 A g^{-1} 1044.4@ 20 A g^{-1}	76.8 / 2000	[188]
Carbon polyhedrons-ZDCP-900^d (ZIF-8 50nm)	1.04	< 3	1000	6 M KOH	~172 @ 0.5 A g^{-1} ~111 @ 15 A g^{-1}	/	[135]
Carbon polyhedrons-ZDCP-1000^d (ZIF-8 50nm)	1.11	< 3	1100	6 M KOH	~188 @ 0.5 A g^{-1} ~152 @ 15 A g^{-1}	/	[135]
Hierarchically porous carbon IM-HPC (Cu-HKUST-1)	~0.556	broad	516	1 M Na$_2$SO$_4$	236 @ 0.5 A g^{-1} 171 @ 100 A g^{-1}	~105 / 10000	[160]
Microporous carbon MPC (Cu-HKUST-1)	~0.448	broad	410	1 M Na$_2$SO$_4$	128 @ 0.5 A g^{-1} 75 @ 100 A g^{-1}	/	[160]
Activated porous carbon NSs APC (Cu-BIB)	1.5	< 6	2491	6 M KOH	260.5 @ 0.5 A g^{-1} 165 @ 10 A g^{-1}	91.1 / 5000	[158]
Conductive carbon nitride (Ni-HNCN)	~0.82	~37.6	181.3	6 M KOH	333.8 @ 5 mV s^{-1} 235.8 @ 100 mV s^{-1}	88.1 / 12000	[191]
Porous carbon NSs NPS-800^d (K-BTC)	1.06	broad	1192	1 M H$_2$SO$_4$	70 @ 0.7 A g^{-1} 40 @ 3.3 A g^{-1}	92 / 5000	[192]
Carbon nanocubes CNC (Zn-BIM)	1.01	broad	1132	6 M KOH	~255 @ 0.5 A g^{-1} ~130 @ 20 A g^{-1}	98.2 / 5000	[161]
Layered carbon nanocubes L-CNC (Zn(BIM)(OAc))	1.21	broad	1453	6 M KOH	~325 @ 0.5 A g^{-1} ~200 @ 20 A g^{-1}	97.5 / 5000	[161]
Ultrathin carbon NSs UT-CNC (UT-Zn(BIM)(OAc))	1.92	broad	1535	6 M KOH	347 @ 0.5 A g^{-1} 283 @ 20 A g^{-1}	98.8 / 5000	[161]

[a] V_{tot} denotes the total volume of materials, which is obtained either from the main text or is estimated from the nitrogen adsorption curves of the literature.

[b] The value is obtained by a three-electrode test if not specified.

[c] For MOF-derived materials, the MOF precursors used are shown in the bracket.

[d] The supercapacitor performance is tested by a two-electrode method.

Table 4. Summary of material parameters of MOF-based materials and their performance as electrodes for lithium-ion batteries.

Materials	V_{tot} (cm^3 g^{-1})	Pore size (nm)	SSA (m^2 g^{-1})	Testing potential *vs.* Li/Li$^+$ (V)	Reversible capacity (mA h g^{-1})	Initial CE / Cycled CE (%)[a]	Retention (%) / cycles[b]	Ref
MOFs as Cathodes								
MIL-101(Fe)	–	–	–	2.2−4.4	110 @ 0.02 C ~27 @ 20 C	82.3 / 98	~120 / 100	[202]
Cu$_3$(HHTP)$_2$	~0.35	~1.9	506.1	1.7−3.5	~95 @ 1 C ~86 @ 20 C	~65 / ~100	~50 / 500	[206]
Cu-CuPc	0.43	1.4 & 11	358	2.0−4.4	~60 @ 0.4 C	~51 / >98	~87 / 200	[205]
Cu-TCA	–	–	180	1.4−4.3	~60 @ 0.5 C ~55 @ 2 C	~75 / 97.2	~54.2 / 200	[203]
MOFs as Anodes								
Ni–Me4BPZ	~0.59	broad	67	0.01−3.0	140 @ 0.05 A g^{-1} (0.36 C)	~38.8 / 98	85.7 / 100	[218]
Li-NTC	–	–	–	0.01−3.0	~450 @ 0.1 A g^{-1} (0.22 C)	53.6 / 97.9	187 / 80	[212]
Ni-NTC	–	–	–	0.01−3.0	~490 @ 0.1 A g^{-1} (0.18 C)	53.9 / 99.1	33 / 80	[212]
Li/Ni-NTC	–	–	–	0.01−3.0	~500 @ 0.1 A g^{-1} (0.20 C)	55.4 / 98.5	~100 / 80	[212]
H-Co-BDC microflowers	0.224	5−50	49.9	0.01−3.0	1345 @ 0.1 A g^{-1} (0.074 C) 798 @ 2 A g^{-1} (1.5 C)	66.7 / 100	98.8 / 100	[230]
CoCOP NWs	0.10	broad	201.2	0.005−3.0	1107 @ 0.02 A g^{-1} (0.020 C) 154 @ 10 A g^{-1} (9 C)	68.3 / 100	~100 / 1000	[204]
Seashell-like Co-BDC	0.108	broad	10.4	0.01−3.0	1107 @ 0.1 A g^{-1} (0.09 C) 604 @ 1 A g^{-1} (0.90 C)	80.4 / 100	92.2 / 200	[197]
CPO-27@250 NR arrays (Fe, Co)	0.27	broad	168.9	0.01−3.0	~700 @ 0.05 A g^{-1} (0.07 C) 440 @ 2 A g^{-1} (2.8 C)	67 / 100	93 / 500	[226]
Mn-BTC	0.0065	broad	23.8	0.01−2.0	694 @ 0.103 A g^{-1} (0.15 C) 250 @ 2.06 A g^{-1} (2.9 C)	40 / 97	83 / 100	[204]
Mn-UMOF NSs	~0.42	3−25	32.6	0.01−3.0	1029 @ 0.1 A g^{-1} (0.10 C) 701 @ 2 A g^{-1} (1.9 C)	57 / 100	115 / 100	[216]
Ni-UMOF NSs	~0.12	3−25	15.0	0.01−3.0	717 @ 0.1 A g^{-1} (0.14 C) 229 @ 2 A g^{-1} (2.8 C)	67 / 100	76.7 / 100	[216]
Zn(IM)$_{1.5}$(ABIM)$_{0.5}$	~0.35	–	821	0.01−3.0	190 @ 0.1 A g^{-1} (0.53 C)	~53 / 97	~100 / 200	[219]

				78 @ 0.4 A g^{-1} (2.1 C)			
AlCl$_3$-FumA	1.21	broad	260.1	0.01−3.0	409 @ 0.0375 A g^{-1} (0.096 C) 258 @ 37.5 A g^{-1} (95.7 C)	45.5 / 95	93.8 / 100	[225]
Ti-DOBDC	~0.26	–	621	0.01−3.0	~527 @ 0.1 A g^{-1} (0.19 C) 120 @ 0.8 A g^{-1} (1.5 C)	75.5 / 100	~85 / 500	[213]
MOF-derivatives as Cathodes								
CoF$_2$/Fe$_2$O$_3$ NPs (FeCo-2-MIM)	~0.54	broad	58.7	1.2−4.5	198.1 @ 0.05 A g^{-1} (0.25 C) 90 @ 1 A g^{-1} (5 C)	~90 / 100	69.8 / 100	[245]
MOF-derivatives as Anodes								
CoO NP cookies (ZIF-67)	~1.82	2−18	364	0.01−3.0	1383 @ 0.1 C 382 @ 10 C	84.5 / 99	99 / 200	[252]
Co$_3$O$_4$ NCs (ZIF-67)	~0.37	10 & 40−80	110.6	0.005−3.0	1069 @ 0.1 A g^{-1} (0.094 C) 712 @ 1 A g^{-1} (0.94 C)	~80.6 / 97.6	100.6 / 100	[250]
Mesoporous Co$_3$O$_4$ MOF-71@300N (MOF-71)	0.45	~30.4	59.0	0.001−3.0	1146 @ 0.05 A g^{-1} (0.044 C) ~140 @ 2 A g^{-1} (1.7 C)	~68 / 97.5	107.4 / 60	[275]
Porous Mn$_2$O$_3$ ([Mn(Br$_4$-BDC)(4,4'-bpy)(H$_2$O)$_2$]$_n$)	~0.118	broad	15.3	0.01−3.0	917 @ 0.2 A g^{-1} (0.22 C) 450 @ 4 A g^{-1} (4.4 C)	73.7 / 99	88.1 / 250	[276]
h-ZIF-8@ZnO (ZIF-8)	~0.52	~1 & 5−8	596.6	0.001−3.0	805.4 @ 0.2 A g^{-1} (0.25 C) 388.6 @ 5 A g^{-1} (6.2 C)	70.2 / 100	92.7 / 100	[249]
Spindle-like α−Fe$_2$O$_3$ (MIL-88-Fe)	~0.056	broad	75	0.01−3.0	~1000 @ 0.1 C 424 @ 10 C	69 / 97	96.9 / 50	[126]
Hierarchical anatase TiO$_2$ (MIL-125 (Ti))	0.62	broad	147	1.0−3.0	~210 @ 0.1 C ~137 @ 10 C	~72 / 99.7	93.5 / 200	[247]
TiO$_2$ microdiscs (MIL-125 (Ti))	0.18	broad	124	1.0−3.0	~233 @ 0.1 C 125 @ 10 C	86 / 100	~101.6 / 1100	[248]
Spinel Zn$_x$Co$_{3-x}$O$_4$ hollow polyhedra (Zn-Co-ZIFs-0.33)	~0.17	broad	65.6	0.01−3.0	1020 @ 1 C 575 @ 10 C	76.2 / 96.6	~100.7 / 50	[127]
Ni$_{0.3}$Co$_{2.7}$O$_4$ NRs (Co/Ni-MOF-74-A)	~0.13	2.2−2.5 & 10−30	28.5	0.005−3.0	~1189 @ 0.1 A g^{-1} (0.084 C) ~780 @ 5 A g^{-1} (4.2 C)	68.5 / 99.3	~118.6 / 200	[265]
Multishelled Ni$_x$Co$_{3-x}$O$_4$-0.1 hollow MSs (Ni-Co-BTC)	~0.26	<10	96.7	0.005−3.0	1104 @ 0.1 A g^{-1} (0.091 C) 546 @ 5 A g^{-1} (4.5 C)	70 / 97	94.1 / 100	[267]
NiFe$_2$O$_4$/Fe$_2$O$_3$ NTs (Fe$_2$Ni MIL-88 / Fe MIL-88)	0.21	~17.7	39.2	0.01−3.0	1392.9 @ 0.1 A g^{-1} (0.072 C) 193.2 @ 5 A g^{-1} (3.6 C)	70.6 / 98	~85 / 100	[264]
Flower-like Sn$_{0.72}$Fe$_{0.28}$O$_2$ (Sn$_m$[Fe(CN)$_6$]$_n$)	~0.19	~4	108.6	0.001−3.0	~870 @ 0.2 A g^{-1} (0.23 C) ~455 @ 4 A g^{-1} (4.6 C)	73 / 99	~47.5 / 100	[123]
Bi@C nanoplates (Bi-BTC)	~0.15	9.7	116	0.01−3	676 @ 0.05 A g^{-1} (0.074 C) 308 @ 1 A g^{-1} (4.4 C)	59 / 98.6	~104.2 / 200	[149]
CoO@C dandelions (Co-BDC)	~0.090	~4 & ~14	60.3	0.01−3	866 @ 0.1 A g^{-1} (0.12 C) 400 @ 5 A g^{-1} (5.8 C)	70.6 / 100	~110 / 300	[257]
MnO@C microspheres (Mn-BTC)	~0.23	~5.7	157.4	0.01−3.0	1191.2 @ 0.1 C 380.1 @ 10 C	~69.0 / 99.6	~157 / 1000	[144]
ZnO/C NCs (Zn-BDC)	~0.40	broad	110	0.01−3.0	750 @ 0.1 A g^{-1} (0.12 C) 351 @ 2 A g^{-1} (2.3 C)	52.9 / 99	~74.3 / 100	[256]

Hollow ZnO/ZnFe$_2$O$_4$/C octahydra (Fe^{III}-MOF-5)	~0.42	~7	140	0.005−3	1060 @ 0.5 A g^{-1} (0.47 C) 762 @ 10 A g^{-1} (9.4 C)	75.6 / 100	~131 / 100	[268]
Fe−Ti−O@C nanotablets (0.6) (MIL-125@FeOOH)	~0.25	~3.46	65.8	0.01−3.0	542 @ 0.1 A g^{-1} (0.18 C) 322 @ 2 A g^{-1} (3.7 C)	61 / ~99	~170 / 160	[147]
Mo$_{0.8}$W$_{0.2}$O$_2$-Cu@P-doped carbon (NENU-5)	~0.16	~10.9	58	0.01−3.0	~980 @ 0.1 A g^{-1} (0.10 C) 521 @ 10 A g^{-1} (10.2 C)	60.4 / 99	106.8 / 250	[146]
PCNS-700 NSs (Al-BPDC)	1.78	~4.54	1571.4	0.01−3	1126 @ 0.1 A g^{-1} (0.089 C) 244 @ 20 A g^{-1} (17.8 C)	~40 / 100	~100 / 100	[157]
N-C-800 (ZIF-8)	0.32	2.0	730.1	0.01−3.0	2037 @ 0.1 A g^{-1} (0.049 C) ~780 @ 5 A g^{-1} (2.5 C)	58.4 / 98	99.2 / 50	[140]
UT-CNSs (Zn(BIM)(OAc))	1.92	broad	1535.2	0.001−3.0	~1200 @ 0.1 A g^{-1} (0.082 C) 553 @ 10 A g^{-1} (8.2 C)	~50.7 / 100	110.1 / 1000	[161]

[a] CE: coulomb efficiency.

[b] An activation access appears for certain materials, hence some retention values are larger than 100%.

Table 5. Summary of material parameters of MOF-based materials and their performance as electrodes for SIBs and PIBs.

Materials	V_{tot} (cm^3 g^{-1})	Pore size (nm)	SSA (m^2 g^{-1})	Testing potential *vs.* Na/Na$^+$ or K/K$^+$ (V)	Reversible capacity (mA h g^{-1})	Initial / cycled CE (%)	Retention (%) / cycles	Ref
				MOFs as SIBs Cathodes				
Fe$_2$(DOBPDC)	–	2.1	–	2.0-3.65	108 @ 0.05 C 77 @ 2 C	~98 / >99	91 / 50	[224]
K$_4$Na$_2$[Fe(C$_2$O$_4$)$_2$]$_3$·2H$_2$O	–	–	–	1.6-4.0	45 @ 0.02 C	–	91 / 10	[211]
FeFe(CN)$_6$ / carbon cloth	–	–	–	*ca.* 2.0-4.0	82 @ 0.2 C ~50 @ 10 C	98.7 / ~100	75 / 200	[210]
				MOFs as SIBs Anodes				
Co-HAB	~0.33	–	240	0.5-3.0	291 @ 0.05 A g^{-1} (0.17 C) 152 @ 12 A g^{-1} (41.2 C)	– / ~100	76 / 50	[220]
u-CoOHtp	~0.11	–	11.5	0.01-3.0	450 @ 0.05 A g^{-1} (0.11 C) 215 @ 2 A g^{-1} (4.44 C)	~75.3 / ~100	82.4 / 50	[199]
Zn-PTCA	–	–	–	0.01-2.0	357 @ 0.05 A g^{-1} (0.14 C) 256 @ 1 A g^{-1} (2.8 C)	45.3 / ~100	75.5 / 1000	[233]
				MOFs as PIBs Cathodes				
CuHCF	–	–	–	0.6-1.4 *vs.* SHE	~59 @ 0.83 C ~50 @ 41.7 C	–	99 / 500	[207]
NiHCF	–	–	–	0.4-1.0 *vs.* SHE	~58 @ 0.83 C ~39 @ 41.7 C	–	~100 / 500	[207]
				MOFs as PIBs Anodes				
MIL-125(Ti)	~0.43	1.6	1103	0.1-3.0	210 @ 0.01 A g^{-1} (0.05 C) 56 @ 0.2 A g^{-1} (0.95 C)	58.9 / ~100	90.2 / 2000	[221]
Layered Co$_2$(OH)$_2$BDC	~0.02	–	5.83	0.2-3.0	352 @ 0.05 A g^{-1} (0.14 C) 131 @ 1 A g^{-1} (2.8 C)	60.6 / ~100	~80 / 600	[222]
				MOF-derivatives as SIB Anodes				
Hollow carbon nanobubbles (ZIF-8)	~1.8	broad	700	0.01−3.0	~236 @ 0.05 A g^{-1} (0.21 C) 90 @ 15 A g^{-1} (63.6 C)	~68.4 / 99	98.1 / 1000	[262]
NC-1 foils (2D Mn-BDC)	~0.54	broad	417.8	0.01−3.0	306 @ 0.05 A g^{-1} (0.16 C) 150 @ 10 A g^{-1} (32.7 C)	~34 / 100	72.8 / 1000	[134]
HNC-800 (Cu-HMT)	0.13	~3.6	35	0.01−3.0	254 @ 0.1 A g^{-1} (0.39 C) 142 @ 5 A g^{-1} (19.7 C)	58 / 99	80.7 / 100	[246]
CUB-600 (Cu/PTA-MOPFs)	~0.005	2−10	6.5	0.01−3.0	236.2 @ 0.1 A g^{-1} (0.42 C) 107.7 @ 5 A g^{-1} (21.2 C)	59.9 / 100	85.5 / 100	[31]
Co$_3$O$_4$/ZnO NSs (ZnCo-2-MIM)	0.42	broad	38.6	0.01−3.0	437 @ 0.1 A g^{-1} (0.23 C) ~220 @ 2 A g^{-1} (4.6 C)	61.2 / 99	87.5 / 100	[255]
Hollow core-shell Zn-doped CoO$_x$	~0.30	2−20	73	0.01−3.0	300 @ 0.05 A g^{-1} (0.17 C) ~170 @ 0.5 A g^{-1} (1.7 C)	~84 / ~96	~73.3 / 110	[254]

(Zn-ZIF-67)							
CuO/Cu$_2$O hollow octahedra (Cu-BTC)	1.45	broad	10.65	0.005−3.0	440 @ 0.05 A g^{-1} (0.11 C) 153.8 @ 2.5 A g^{-1} (5.7 C)	45 / 98	~101.2 / 50	[129]
VO$_x$/PCs NRs ([V(OH)(NDC)·xG]$_n$)	~0.17	broad	84.9	0.01−3.0	481.5 @ 0.04 A g^{-1} (0.083 C) 90 @ 10 A g^{-1} (20.8 C)	~36.7 / 100	75 / 2000	[271]
Co$_3$O$_4$@NC NPs (ZIF-67)	~0.17	~5 & 20−60	101	0.01−3.0	506 @ 0.1 A g^{-1} (0.2 C) 263 @ 1 A g^{-1} (2 C)	63.5 / 100	87 / 60	[270]
Ni-doped Co/CoO/NC (NiCo-2-MIM)	0.28	~0.5 & 2−10	552	0.01−3.0	307 @ 0.1 A g^{-1} (0.33 C) 110 @ 5 A g^{-1} (16 C)	54 / 98	87.5 / 100	[277]
CoS$_2$/NC spheres (Co-BTC)	~0.10	<2 & 5-10	116.8	0.01−3.0	782.3 @ 0.1 A g^{-1} (0.13 C) 637.4 @ 10 A g^{-1} (13 C)	~82.1 / 99	~106 / 100	[29]
Cu$_2$Se@C porous octahedra (Cu-BTC)	0.15	38.0	68.9	0.5−3.0	272.1 @ 0.05 A g^{-1} (0.18 C) 166.3 @ 3 A g^{-1} (11.0 C)	95.2 / 100	~94.0 / 100	[30]
Fe$_7$Se$_8$@C NRs (Fe-TPA)	0.084	broad	42.7	0.5−3.0	378 @ 0.1 A g^{-1} (0.26 C) 150 @ 5 A g^{-1} (13.2 C)	~85 / 100	~96.9 / 100	[30]
NiSe@C hollow MSs (Ni-BTC)	0.2	~46.3	64.8	0.5−3.0	440 @ 0.1 A g^{-1} (0.23 C) 153 @ 5 A g^{-1} (11.4 C)	~88 / 99	~74.7 / 100	[30]
MOF-derivatives as PIB Anodes							
NPC-600 (ZIF-67)	~1.4	broad	908.2	0.01−3.0	587.6 @ 0.05 A g^{-1} (0.085 C) 186.2 @ 2 A g^{-1} (3.4 C)	31.5 / 100	81.8 / 50	[132]
N-HPC (ZIF-8)	~0.80	broad	820	0.01−3.0	292 @ 0.1 A g^{-1} (0.34 C) 94 @ 10 A g^{-1} (34.2 C)	13.9 / 99	70.2 / 400	[159]
NC@CoP/NC polyhedron (ZIF-8@ZIF-67)	~0.25	broad	39	0.01−2.5	479 @ 0.05 A g^{-1} (0.1 C) 200 @ 2 A g^{-1} (4.2 C)	27.7 / 99	93 / 100	[153]

Table 6. List of MOFs and organic ligands mentioned in the current review.

MOFs			
bio-MOF-100	Zn-BPDC	MOF-71	Co-BDC
bio-MOF-101	Zn-NDC	MOF-177	Zn-BTB
bio-MOF-102	Zn-ABDC	MOF-180	Zn-BTE
bio-MOF-103	Zn-NH$_2$-TPDC	MOF-200	Zn-BBC
DUT-5	Al(OH)BPDC	MOF-210	Zn-BTE/BPDC
DUT-60	Zn$_4$O-BBC/BCPBD	MOF-867	Zr-BPYDC
HKUST-1 (= MOF-199)	Cu$_3$(BTC)$_2$	NU-110	Cu-LH$_6$-2
MIL-53 (Fe)	Fe(OH)$_{0.8}$F$_{0.2}$(BDC) (*C2/c* group)	CPM-12	Zr-BTB/BTC
MIL-68 (Fe)	FeOH(BDC) (*Cmcm* group)	PCN-332	M-BTTC (M = Al, Fe, Sc, V, In)
MIL-88 (Fe)	Fe-BDC (*P−62C* group)	PCN-333	M-TATB (M = Al, Fe, Sc)
MIL-100 (Cr)	Cr-BTC	UiO-66	Zr-BDC

MIL-101(Fe)	Fe-BDC (*Fd−3m* group)	UiO-67	Zr-BPDC
MIL-125 (Ti)	Ti-TPA	ZIF-8	Zn-2-MIM
MIT-20 (Cu)	(CH$_3$)$_2$NH$_2$)[Cu$_2$Cl$_3$BTDD]·(DMF)$_4$(H$_2$O)$_{4.5}$	ZIF-67	Zn-2-MIM
MIT-20d (Cu)	Cu$_2$Cl$_2$BTDD	437-MOF	In-BTTB
MOF-5	Zn-BDC	CPO-27 (MOF-74)	M-DOBDC (M = Fe, Co, *etc.*)

| Ligands			
ABIM	2-aminobenzimidazole	H$_2$BCPBD	bis-pcarboxyphenylbuta-1,3-diene
ABTC	5,5′-azobenzene-tetracarboxylate	H$_2$BTDD	bis(1H-1,2,3-triazolo[4,5-b],[4′,5′-i])dibenzo-[1,4]dioxin
ADC	9,10-anthracenedicarboxylate	H$_3$BTTB	4,4′,4′′-[benzene-1,3,5-triyl-tris(oxy)]tribenzoic acid
AQDC	anthraquinone dicarboxylate	HITB	2,3,6,7,10,11-hexaiminotriphenylene
AZDC	azobenzene-4,4′-dicarboxylate	HHTP	2,3,6,7,10,11-hexahydroxytriphenylene
BBC	1,3,5-tris(4′-carboxy[1,1′-biphenyl]-4-yl)benzene	H$_2$Me$_4$BPZ	3,3′,5,5′-tetramethyl-4,4′-bipyrazole
BDC	1,4-benzenedicarboxylate (terephthalate)	HMT	hexamine
BHC	1,2,3,4,5,6-benzenehexacarboxylate	H$_3$TCA	tricarboxytriphenyl amine
BIB	1,4-bis(2-methyl-imidazol-1-yl)butane	H$_3$TCBPB	tris(4′-carboxy[1,1′-biphenyl]-4-yl)benzene
BIM	benzimidazole	H$_2$TFBDC	2,3,5,6-tetrafluoroterephthalic acid
BPDC	4,4′-biphenyldicarboxylate	H$_2$TPA	terephthalic acid
BPTC	3,3′,5,5′-biphenyltetracarboxylate	H$_4$TPCB	3,3′,5,5′-tetra(phenyl-4-carboxylic acid)
BPY	4,4′ -bipyridine	H$_4$TPDC	[(1,1′:4′,1′′-terphenyl)-2,2′′,4,4′′-tetracarboxylic acid
BPYDC	BPYDC = 2,2′-bipyridine-5,5′-dicarboxylate	H$_4$TTPM	tetrakis(4-tetrazolylphenyl)methane
Br$_4$-BDC	tetrabromoterephthalate	IM	Imidazole
BTE	4,4′,4′′-[benzene-1,3,5-triyl-tris(ethyne-2,1-diyl)]tribenzoate	LCP	2,3,5,6-tetrafluoroterephthalatic 4,4′-bipyridine
BTB	1,3,5-tri(4-carboxyphenyl)benzene	LH$_6$-2	1,3,5-tris[((1,3-carboxylic acid-5-(4-(ethynyl)phenyl))ethynyl)phenyl]-benzene
BTC	1,3,5-benzenetricarboxylate	2-MIM	methylimidazole
BTE	4,4′,4′′-[benzene-1,3,5-triyl-tris(ethyne-2,1-diyl)]tribenzoate	NDC	1,4-naphthalene dicarboxylates
BTTC	benzo-tris-thiophene carboxylate	NTC	1,4,5,8-naphthalenetetracarboxylates
BTTri	1,3,5-tris(1*H*-1,2,3-triazol-5-yl)benzene	OBA	4,49-oxybisbenzoic
CBAB	4-carboxybenzylidene-4-aminobenzate	PTA	p-benzenedicarboxylate
CuPcOH	copper(II) 2,3,9,10,16,17,23,24-octahydroxy-29H,31H-phthalocyanine	PTCA	3,4,9,10-perylenetetracarboxylate
DABCO	1,4-diazabicyclo[2.2.2]octane	TATB	4,4′,4′′-s-triazine-2,4,6-triyl-tribenzoate
DMOF	DABCO MOFs	TCNQ	7,7,8,8-tetracyanoquinodimethane
DOBDC	2,5-dioxidobenzene-1,4-dicarboxylate	TCPP	tetrakis (4-carboxyphenyl) porphyrin
DOBPDC	4,4′-dioxidobiphenyl-3,3′-dicarboxylate	TDA	2,5-thiophenedicarboxylate
DOT	2,5-dihydroxy-1,4-benzenedicarboxylate	TP	terephthalate
FumA	1,4-dicarboxylate	TPT	2,4,6-tri(pyridin-4-yl)-1,3,5-triazine
HAB	hexaaminobenzene	TPTC	(Me)$_2$ 2′,5′-dimethyl-[1,1′:4′,1′′-terphenyl]-3,3′′,5,5′′-tetracarboxylate
H$_2$ATPA	aminoterephthalic acid		

Biographies

Ran Du received his B.E. in 2011 from Beijing Institute of Technology and PhD degree in 2016 from Peking University (Advisor: Prof. J. Zhang). Afterwards, he has worked as postdoc researcher successively in Nanyang Technological University (Advisor: Prof. X.D. Chen), TU Dresden (Advisor: Prof. A. Eychmüller), and currently the University of Hong Kong (Advisor: Prof. Z.X. Guo). His main research interest lies in the development of fabrication methodologies of versatile gel materials based on metals, nanocarbons, metal-organic frameworks, and polymers for applications in electrocatalysis, oil/water separation, smart materials, and so on.

Zhengxiao Guo is a Professor of Chemistry and Mechanical Engineering at the University of Hong Kong, and an Honorary Professor of University College London (UCL) since 2018. He was a Professor of Chemistry at UCL (2007-2018), a Lecturer/Professor at Queen Mary University of London (1995-2007), and a research fellow respectively at the University of Oxford (1990-1995) and of Strathclyde (1988-1990). He obtained his PhD from the University of Manchester in1988. His research focuses on functional nanomaterials for energy and environmental applications, including imbedded atoms, molecules, clusters, 2D structures, COFs, MOFs and hierarchically porous structures.

Table of contents

Metal-Organic Frameworks (MOFs) and their derivatives have been extensively investigated for energy storage devices in the last decade. This overview examines structural and chemical components and coordination from the porosity point of view, emphasizing the state-of-the-art synthesis strategies and applications in supercapacitors and metal-ion batteries. Opportunities and challenges are highlighted for future development in the subject area.
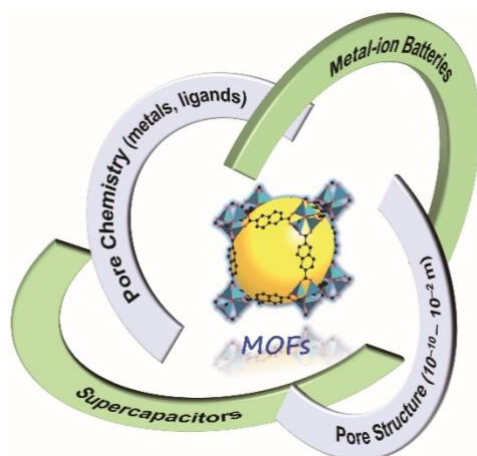
R. Du, Y. Wu, Y. Yang, T. Zhai, T. Zhou, Q. Shang, L. Zhu, C. Shang, and Z. Guo.

Porosity engineering of MOF-based materials for electrochemical energy storage

References

[1]   X.-B. Cheng, C.-Z. Zhao, Y.-X. Yao, H. Liu, Q. Zhang, *Chem* **2019**, *5*, 74-96.

[2]   C. Choi, D. S. Ashby, D. M. Butts, R. H. DeBlock, Q. Wei, J. Lau, B. Dunn, *Nat. Rev. Mater.* **2020**, *5*, 5-19.

[3]   F. Wang, X. Wu, X. Yuan, Z. Liu, Y. Zhang, L. Fu, Y. Zhu, Q. Zhou, Y. Wu, W. Huang, *Chem. Soc. Rev.* **2017**, *46*, 6816-6854.

[4]   Y. Yang, X. Liu, Z. Zhu, Y. Zhong, Y. Bando, D. Golberg, J. Yao, X. Wang, *Joule* **2018**, *2*, 1075-1094.

[5]   F. Wu, J. Maier, Y. Yu, *Chem. Soc. Rev.* **2020**, *49*, 1569-1614.

[6]   M. Armand, J. M. Tarascon, *Nature* **2008**, *451*, 652-657.

[7]   O. M. Yaghi, G. Li, H. Li, *Nature* **1995**, *378*, 703-706.

[8]   M. J. Kalmutzki, N. Hanikel, O. M. Yaghi, *Sci. Adv.* **2018**, *4*, eaat9180.

[9]   M. O'Keeffe, M. A. Peskov, S. J. Ramsden, O. M. Yaghi, *Acc. Chem. Res.* **2008**, *41*, 1782-1789.

[10]   O. K. Farha, I. Eryazici, N. C. Jeong, B. G. Hauser, C. E. Wilmer, A. A. Sarjeant, R. Q. Snurr, S. T. Nguyen, A. Ö. Yazaydın, J. T. Hupp, *J. Am. Chem. Soc.* **2012**, *134*, 15016-15021.

[11]   I. M. Hönicke, I. Senkovska, V. Bon, I. A. Baburin, N. Bönisch, S. Raschke, J. D. Evans, S. Kaskel, *Angew. Chem. Int. Ed.* **2018**, *57*, 13780-13783.

[12]   X. Zhang, X. Wang, W. Fan, D. Sun, *Chem. Commun.* **2020**, *38*, 509-524.

[13]   Z. Ji, H. Wang, S. Canossa, S. Wuttke, O. M. Yaghi, *Adv. Funct. Mater.* **2020**, *n/a*, 2000238.

[14]   X. Chen, Q. Zhang, *Particuology* **2019**, *45*, 20-34.

[15]   H. V. Doan, H. Amer Hamzah, P. Karikkethu Prabhakaran, C. Petrillo, V. P. Ting, *Nano-Micro Letters* **2019**, *11*, 54.

[16]   A. E. Baumann, D. A. Burns, B. Liu, V. S. Thoi, *Communications Chemistry* **2019**, *2*, 86.

[17]   M. Hmadeh, Z. Lu, Z. Liu, F. Gándara, H. Furukawa, S. Wan, V. Augustyn, R. Chang, L. Liao, F. Zhou, E. Perre, V. Ozolins, K. Suenaga, X. Duan, B. Dunn, Y. Yamamto, O. Terasaki, O. M. Yaghi, *Chem. Mater.* **2012**, *24*, 3511-3513.

[18]   D. Sheberla, L. Sun, M. A. Blood-Forsythe, S. Er, C. R. Wade, C. K. Brozek, A. Aspuru-Guzik, M. Dincă, *J. Am. Chem. Soc.* **2014**, *136*, 8859-8862.

[19]   A. A. Talin, A. Centrone, A. C. Ford, M. E. Foster, V. Stavila, P. Haney, R. A. Kinney, V. Szalai, F. El Gabaly, H. P. Yoon, F. Léonard, M. D. Allendorf, *Science* **2014**, *343*, 66-69.

[20]   R. Díaz, M. G. Orcajo, J. A. Botas, G. Calleja, J. Palma, *Mater. Lett.* **2012**, *68*, 126-128.

[21]   X. Li, F. Cheng, S. Zhang, J. Chen, *J. Power Sources* **2006**, *160*, 542-547.

[22]   G. Férey, F. Millange, M. Morcrette, C. Serre, M.-L. Doublet, J.-M. Grenèche, J.-M. Tarascon, *Angew. Chem. Int. Ed.* **2007**, *46*, 3259-3263.

[23]   A. Eftekhari, *J. Power Sources* **2004**, *126*, 221-228.

[24]   C. D. Wessells, S. V. Peddada, R. A. Huggins, Y. Cui, *Nano Lett.* **2011**, *11*, 5421-5425.

[25]   S. Gadipelli, Z. Guo, *Chem. Mater.* **2014**, *26*, 6333-6338.

[26]   B. Y. Xia, Y. Yan, N. Li, H. B. Wu, X. W. Lou, X. Wang, *Nat. Energy* **2016**, *1*, 15006.

[27]   C. Guan, X. Liu, W. Ren, X. Li, C. Cheng, J. Wang, *Adv. Energy Mater.* **2017**, *7*, 1602391.

[28]   Z.-J. Jiang, S. Cheng, H. Rong, Z. Jiang, J. Huang, *J. Mater. Chem. A* **2017**, *5*, 23641-23650.

[29]   L. Chen, N. Luo, S. Huang, Y. Li, M. Wei, *Chem. Commun.* **2020**, *2020 v.56 no.28*, pp. 3951-3954.

[30]   X. Xu, J. Liu, J. Liu, L. Ouyang, R. Hu, H. Wang, L. Yang, M. Zhu, *Adv. Funct. Mater.* **2018**, *28*, 1707573.

[31]   Y. Li, M. Kong, J. Hu, J. Zhou, *Adv. Energy Mater.* **2020**, *10*, 2000400.

[32]   X. Liu, W. Zang, C. Guan, L. Zhang, Y. Qian, A. M. Elshahawy, D. Zhao, S. J. Pennycook, J. Wang, *ACS Energy Lett.* **2018**, *3*, 2462-2469.

[33]   X. Feng, H. Wang, X. Bo, L. Guo, *ACS Appl. Mater. Interfaces* **2019**, *11*, 8018-8024.

[34]   B. K. Kang, S. Y. Im, J. Lee, S. H. Kwag, S. B. Kwon, S. Tiruneh, M.-J. Kim, J. H. Kim, W. S. Yang, B. Lim, D. H. Yoon, *Nano Res.* **2019**, *12*, 1605-1611.

[35]   M. Zhong, L. Kong, N. Li, Y.-Y. Liu, J. Zhu, X.-H. Bu, *Coord. Chem. Rev.* **2019**, *388*, 172-201.

[36]   C. Wang, J. Kim, J. Tang, M. Kim, H. Lim, V. Malgras, J. You, Q. Xu, J. Li, Y. Yamauchi, *Chem* **2020**, *6*, 19-40.

[37]   H. B. Wu, X. W. Lou, *Sci. Adv.* **2017**, *3*, eaap9252.

[38]   X. Cao, C. Tan, M. Sindoro, H. Zhang, *Chem. Soc. Rev.* **2017**, *46*, 2660-2677.

[39]   B. Y. Guan, X. Y. Yu, H. B. Wu, X. W. Lou, *Adv. Mater.* **2017**, *29*, 1703614.

[40]   W. Du, Y.-L. Bai, J. Xu, H. Zhao, L. Zhang, X. Li, J. Zhang, *J. Power Sources* **2018**, *402*, 281-295.

[41]   R. Zhao, Z. Liang, R. Zou, Q. Xu, *Joule* **2018**, *2*, 2235-2259.

[42]   X. Li, S. Zheng, L. Jin, Y. Li, P. Geng, H. Xue, H. Pang, Q. Xu, *Adv. Energy Mater.* **2018**, *8*, 1800716.

[43]   M. Du, Q. Li, Y. Zhao, C.-S. Liu, H. Pang, *Coord. Chem. Rev.* **2020**, *416*, 213341.

[44]   X. Zhang, A. Chen, M. Zhong, Z. Zhang, X. Zhang, Z. Zhou, X.-H. Bu, *Electrochemical Energy Reviews* **2019**, *2*, 29-104.

[45]   R. Zhao, Y. Wu, Z. Liang, L. Gao, W. Xia, Y. Zhao, R. Zou, *Energy Environ. Sci.* **2020**, *13*, 2386-2403.

[46]   A. G. Slater, A. I. Cooper, *Science* **2015**, *348*, aaa8075.

[47]   L. L. Zhang, X. S. Zhao, *Chem. Soc. Rev.* **2009**, *38*, 2520-2531.

[48]   Z. Li, S. Gadipelli, H. Li, C. A. Howard, D. J. L. Brett, P. R. Shearing, Z. Guo, I. P. Parkin, F. Li, *Nat. Energy* **2020**, *5*, 160-168.

[49]   P. Simon, Y. Gogotsi, *Nat. Mater.* **2020**.

[50]   N.-S. Choi, Z. Chen, S. A. Freunberger, X. Ji, Y.-K. Sun, K. Amine, G. Yushin, L. F. Nazar, J. Cho, P. G. Bruce, *Angew. Chem. Int. Ed.* **2012**, *51*, 9994-10024.

[51]   C. Yang, X. Li, L. Yu, X. Liu, J. Yang, M. Wei, *Chem. Commun.* **2020**, *56*, 1803-1806.

[52]   L. Chen, Q. Zhang, H. Xu, X. Hou, L. Xuan, Y. Jiang, Y. Yuan, *J. Mater. Chem. A* **2015**, *3*, 1847-1852.

[53]   D. Feng, T. Lei, M. R. Lukatskaya, J. Park, Z. Huang, M. Lee, L. Shaw, S. Chen, A. A. Yakovenko, A. Kulkarni, J. Xiao, K. Fredrickson, J. B. Tok, X. Zou, Y. Cui, Z. Bao, *Nat. Energy* **2018**, *3*, 30-36.

[54]   D. Sheberla, J. C. Bachman, J. S. Elias, C.-J. Sun, Y. Shao-Horn, M. Dincă, *Nat. Mater.* **2017**, *16*, 220-224.

[55]   S. Gadipelli, Z. X. Guo, *ChemSusChem* **2015**, *8*, 2123-2132.

[56]   S. Gadipelli, T. Zhao, S. A. Shevlin, Z. Guo, *Energy Environ. Sci.* **2016**, *9*, 1661-1667.

[57]   J. Guo, S. Gadipelli, Y. Yang, Z. Li, Y. Lu, D. J. L. Brett, Z. Guo, *J. Mater. Chem. A* **2019**, *7*, 3544-3551.

[58]   U. Lee, A. Valekar, Y. Hwang, J. Chang, *The Chemistry of Metal–Organic Frameworks*, Wiley-VCH Verlag GmbH & Co. KGaA New York, **2016**.

[59]   A. J. Rieth, A. M. Wright, M. Dincă, *Nat. Rev. Mater.* **2019**, *4*, 708-725.

[60]   N. Huang, S. Yuan, H. Drake, X. Yang, J. Pang, J. Qin, J. Li, Y. Zhang, Q. Wang, D. Jiang, H.-C. Zhou, *J. Am. Chem. Soc.* **2017**, *139*, 18590-18597.

[61]   M. Meilikhov, K. Yusenko, R. A. Fischer, *J. Am. Chem. Soc.* **2009**, *131*, 9644-9645.

[62]   C. K. Brozek, M. Dincă, *J. Am. Chem. Soc.* **2013**, *135*, 12886-12891.

[63]   Z. Wei, W. Lu, H.-L. Jiang, H.-C. Zhou, *Inorg. Chem.* **2013**, *52*, 1164-1166.

[64]   P. Deria, J. E. Mondloch, O. Karagiaridi, W. Bury, J. T. Hupp, O. K. Farha, *Chem. Soc. Rev.* **2014**, *43*, 5896-5912.

[65]   V. Colombo, C. Montoro, A. Maspero, G. Palmisano, N. Masciocchi, S. Galli, E. Barea, J. A. R. Navarro, *J. Am. Chem. Soc.* **2012**, *134*, 12830-12843.

[66]   H. Deng, C. J. Doonan, H. Furukawa, R. B. Ferreira, J. Towne, C. B. Knobler, B. Wang, O. M. Yaghi, *Science* **2010**, *327*, 846-850.

[67]   S. Bernt, V. Guillerm, C. Serre, N. Stock, *Chem. Commun.* **2011**, *47*, 2838-2840.

[68]   X.-J. Hu, Z.-X. Li, H. Xue, X. Huang, R. Cao, T.-F. Liu, *CCS Chemistry* **2020**, *2*, 616-622.

[69]   M. Kim, J. F. Cahill, Y. Su, K. A. Prather, S. M. Cohen, *Chem. Sci.* **2012**, *3*, 126-130.

[70]   M. Kim, J. F. Cahill, H. Fei, K. A. Prather, S. M. Cohen, *J. Am. Chem. Soc.* **2012**, *134*, 18082-18088.

[71]   Q. Liu, H. Cong, H. Deng, *J. Am. Chem. Soc.* **2016**, *138*, 13822-13825.

[72]   R. Du, Q. Zhao, Z. Zheng, W. Hu, J. Zhang, *Adv. Energy Mater.* **2016**, *6*, 1600473.

[73]   C. Yu, P. Zhang, J. Wang, L. Jiang, *Adv. Mater.* **2017**, *29*, 1703053.

[74]   B. Su, Y. Tian, L. Jiang, *J. Am. Chem. Soc.* **2016**, *138*, 1727-1748.

[75]   J. Pang, S. Yuan, J. Qin, C. Liu, C. Lollar, M. Wu, D. Yuan, H.-C. Zhou, M. Hong, *J. Am. Chem. Soc.* **2017**, *139*, 16939-16945.

[76]   H. Wang, X. Dong, J. Lin, S. J. Teat, S. Jensen, J. Cure, E. V. Alexandrov, Q. Xia, K. Tan, Q. Wang, D. H. Olson, D. M. Proserpio, Y. J. Chabal, T. Thonhauser, J. Sun, Y. Han, J. Li, *Nat. Commun.* **2018**, *9*, 1745.

[77]   S.-T. Zheng, J. J. Bu, T. Wu, C. Chou, P. Feng, X. Bu, *Angew. Chem. Int. Ed.* **2011**, *50*, 8858-8862.

[78]   Q.-G. Zhai, X. Bu, X. Zhao, D.-S. Li, P. Feng, *Acc. Chem. Res.* **2017**, *50*, 407-417.

[79]   O. Karagiaridi, W. Bury, E. Tylianakis, A. A. Sarjeant, J. T. Hupp, O. K. Farha, *Chem. Mater.* **2013**, *25*, 3499-3503.

[80]   W. Fan, X. Wang, X. Liu, B. Xu, X. Zhang, W. Wang, X. Wang, Y. Wang, F. Dai, D. Yuan, D. Sun, *ACS Sustain. Chem. Eng.* **2019**, *7*, 2134-2140.

[81]   Y.-S. Wei, M. Zhang, P.-Q. Liao, R.-B. Lin, T.-Y. Li, G. Shao, J.-P. Zhang, X.-M. Chen, *Nat. Commun.* **2015**, *6*, 8348.

[82]   J. K. Schnobrich, K. Koh, K. N. Sura, A. J. Matzger, *Langmuir* **2010**, *26*, 5808-5814.

[83]   H. Furukawa, N. Ko, Y. B. Go, N. Aratani, S. B. Choi, E. Choi, A. Ö. Yazaydin, R. Q. Snurr, M. O'Keeffe, J. Kim, O. M. Yaghi, *Science* **2010**, *329*, 424-428.

[84]   H. K. Chae, D. Y. Siberio-Pérez, J. Kim, Y. Go, M. Eddaoudi, A. J. Matzger, M. O'Keeffe, O. M. Yaghi, D. Materials, G. Discovery, *Nature* **2004**, *427*, 523-527.

[85]   D. Feng, T.-F. Liu, J. Su, M. Bosch, Z. Wei, W. Wan, D. Yuan, Y.-P. Chen, X. Wang, K. Wang, X. Lian, Z.-Y. Gu, J. Park, X. Zou, H.-C. Zhou, *Nat. Commun.* **2015**, *6*, 5979.

[86]   G. Férey, C. Serre, C. Mellot‐Draznieks, F. Millange, S. Surblé, J. Dutour, I. J. A. C. Margiolaki, *Angew. Chem. Int. Ed.* **2004**, *116*, 6456-6461.

[87]   J. Park, D. Feng, H.-C. Zhou, *J. Am. Chem. Soc.* **2015**, *137*, 1663-1672.

[88]   T. Li, M. T. Kozlowski, E. A. Doud, M. N. Blakely, N. L. Rosi, *J. Am. Chem. Soc.* **2013**, *135*, 11688-11691.

[89]   C.-C. Liang, Z.-L. Shi, C.-T. He, J. Tan, H.-D. Zhou, H.-L. Zhou, Y. Lee, Y.-B. Zhang, *J. Am. Chem. Soc.* **2017**, *139*, 13300-13303.

[90]   G. Cai, H.-L. Jiang, *Angew. Chem. Int. Ed.* **2017**, *56*, 563-567.

[91]   Y. Mao, D. Chen, P. Hu, Y. Guo, Y. Ying, W. Ying, X. Peng, *Chem. Eur. J.* **2015**, *21*, 15127-15132.

[92]   L. Feng, S. Yuan, L.-L. Zhang, K. Tan, J.-L. Li, A. Kirchon, L.-M. Liu, P. Zhang, Y. Han, Y. J. Chabal, H.-C. Zhou, *J. Am. Chem. Soc.* **2018**, *140*, 2363-2372.

[93]   S. Yuan, L. Zou, J.-S. Qin, J. Li, L. Huang, L. Feng, X. Wang, M. Bosch, A. Alsalme, T. Cagin, H.-C. Zhou, *Nat. Commun.* **2017**, *8*, 15356.

[94]   S. Abedi, A. Morsali, *ACS Catal.* **2014**, *4*, 1398-1403.

[95]   L.-B. Sun, J.-R. Li, J. Park, H.-C. Zhou, *J. Am. Chem. Soc.* **2012**, *134*, 126-129.

[96]   Y. Zhao, J. Zhang, B. Han, J. Song, J. Li, Q. Wang, *Angew. Chem. Int. Ed.* **2011**, *50*, 636-639.

[97]   H. Huang, J.-R. Li, K. Wang, T. Han, M. Tong, L. Li, Y. Xie, Q. Yang, D. Liu, C. Zhong, *Nat. Commun.* **2015**, *6*, 8847.

[98]   L. Peng, J. Zhang, Z. Xue, B. Han, X. Sang, C. Liu, G. Yang, *Nat. Commun.* **2014**, *5*, 4465.

[99]   Y. Cao, Y. Ma, T. Wang, X. Wang, Q. Huo, Y. Liu, *Cryst. Growth Des.* **2016**, *16*, 504-510.

[100] C. Avci, J. Ariñez‐Soriano, A. Carné‐Sánchez, V. Guillerm, C. Carbonell, I. Imaz, D. Maspoch, *Angew. Chem. Int. Ed.* **2015**, *127*, 14625-14629.

[101] M. Hu, Y. Ju, K. Liang, T. Suma, J. Cui, F. Caruso, *Adv. Funct. Mater.* **2016**, *26*, 5827-5834.

[102] Y. Sun, F. Yang, Q. Wei, N. Wang, X. Qin, S. Zhang, B. Wang, Z. Nie, S. Ji, H. Yan, J.-R. Li, *Adv. Mater.* **2016**, *28*, 2374-2381.

[103] Y. Hu, H. Lian, L. Zhou, G. Li, *Anal. Chem.* **2015**, *87*, 406-412.

[104] K.-Y. Andrew Lin, H.-A. Chang, *J. Mater. Chem. A* **2015**, *3*, 20060-20064.

[105] N. Huang, H. Drake, J. Li, J. Pang, Y. Wang, S. Yuan, Q. Wang, P. Cai, J. Qin, H. C. Zhou, *Angew. Chem. Int. Ed.* **2018**, *130*, 9054-9058.

[106] K. Shen, L. Zhang, X. Chen, L. Liu, D. Zhang, Y. Han, J. Chen, J. Long, R. Luque, Y. Li, B. Chen, *Science* **2018**, *359*, 206-210.

[107] S. S. Kistler, *Nature* **1931**, *127*, 741-741.

[108] J. Livage, M. Henry, C. Sanchez, *Prog. Solid State Chem.* **1988**, *18*, 259-341.

[109] R. Du, Q. Zhao, N. Zhang, J. Zhang, *Small* **2015**, *11*, 3263-3289.

[110] R. Du, X. Fan, X. Jin, R. Hübner, Y. Hu, A. Eychmüller, *Matter* **2019**, *1*, 39-56.

[111] J. L. Mohanan, I. U. Arachchige, S. L. Brock, *Science* **2005**, *307*, 397-400.

[112] L. Wang, H. Xu, J. Gao, J. Yao, Q. Zhang, *Coord. Chem. Rev.* **2019**, *398*, 213016.

[113] B. Bueken, N. Van Velthoven, T. Willhammar, T. Stassin, I. Stassen, D. A. Keen, G. V. Baron, J. F. M. Denayer, R. Ameloot, S. Bals, D. De Vos, T. D. Bennett, *Chem. Sci.* **2017**, *8*, 3939-3948.

[114] M. R. Lohe, M. Rose, S. Kaskel, *Chem. Commun.* **2009**, 6056-6058.

[115] S. Xiang, L. Li, J. Zhang, X. Tan, H. Cui, J. Shi, Y. Hu, L. Chen, C.-Y. Su, S. L. James, *J. Mater. Chem.* **2012**, *22*, 1862-1867.

[116] L. Li, S. Xiang, S. Cao, J. Zhang, G. Ouyang, L. Chen, C.-Y. Su, *Nat. Commun.* **2013**, *4*, 1774.

[117] H. Thakkar, S. Eastman, Q. Al-Naddaf, A. A. Rownaghi, F. Rezaei, *ACS Appl. Mater. Interfaces* **2017**, *9*, 35908-35916.

[118] S. Sultan, H. N. Abdelhamid, X. Zou, A. P. Mathew, *Adv. Funct. Mater.* **2019**, *29*, 1805372.

[119] J.-L. Zhuang, D. Ar, X.-J. Yu, J.-X. Liu, A. Terfort, *Adv. Mater.* **2013**, *25*, 4631-4635.

[120] C. Jiao, Z. Wang, X. Zhao, H. Wang, J. Wang, R. Yu, D. Wang, *Angew. Chem. Int. Ed.* **2019**, *58*, 996-1001.

[121] Z. Bai, Y. Zhang, Y. Zhang, C. Guo, B. Tang, D. Sun, *J. Mater. Chem. A* **2015**, *3*, 5266-5269.

[122] X. Wang, L. Yu, B. Y. Guan, S. Song, X. W. Lou, *Adv. Mater.* **2018**, *30*, 1801211.

[123] Y. Yan, F. Du, X. Shen, Z. Ji, X. Sheng, H. Zhou, G. Zhu, *J. Mater. Chem. A* **2014**, *2014 v.2 no.38*, pp. 15875-15882.

[124] V. Soundharrajan, B. Sambandam, J. Song, S. Kim, J. Jo, S. Kim, S. Lee, V. Mathew, J. Kim, *ACS Appl. Mater. Interfaces* **2016**, *8*, 8546-8553.

[125] Y. Lin, Z. Tian, L. Zhang, J. Ma, Z. Jiang, B. J. Deibert, R. Ge, L. Chen, *Nat. Commun.* **2019**, *10*, 162.

[126] X. Xu, R. Cao, S. Jeong, J. Cho, *Nano Lett.* **2012**, *12*, 4988-4991.

[127] R. Wu, X. Qian, K. Zhou, J. Wei, J. Lou, P. M. Ajayan, *ACS Nano* **2014**, *8*, 6297-6303.

[128] R. Wu, X. Qian, F. Yu, H. Liu, K. Zhou, J. Wei, Y. Huang, *J. Mater. Chem. A* **2013**, *1*, 11126-11129.

[129] X. Zhang, W. Qin, D. Li, D. Yan, B. Hu, Z. Sun, L. Pan, *Chem. Commun.* **2015**, *51*, 16413-16416.

[130] J. Shao, Z. Wan, H. Liu, H. Zheng, T. Gao, M. Shen, Q. Qu, H. Zheng, *J. Mater. Chem. A* **2014**, *2014 v.2 no.31*, pp. 12194-12200.

[131] Y. Han, S. Zhang, N. Shen, D. Li, X. Li, *Mater. Lett.* **2017**, *188*, 1-4.

[132] Y. Li, C. Yang, F. Zheng, X. Ou, Q. Pan, Y. Liu, G. Wang, *J. Mater. Chem. A* **2018**, *6*, 17959-17966.

[133] Y. Qian, Z. Hu, X. Ge, S. Yang, Y. Peng, Z. Kang, Z. Liu, J. Y. Lee, D. Zhao, *Carbon* **2017**, *111*, 641-650.

[134] L. Kong, J. Zhu, W. Shuang, X.-H. Bu, *Adv. Energy Mater.* **2018**, *8*, 1801515.

[135] S. Gadipelli, Z. Li, Y. Lu, J. Li, J. Guo, N. T. Skipper, P. R. Shearing, D. J. Brett, *Adv. Sci.* **2019**, *6*, 1901517.

[136] A. Li, Y. Tong, B. Cao, H. Song, Z. Li, X. Chen, J. Zhou, G. Chen, H. Luo, *Sci. Rep.* **2017**, *7*, 40574.

[137] X. Li, H. Yuan, X. Quan, S. Chen, S. You, *Journal of Environmental Sciences* **2018**, *63*, 250-259.

[138] T. Liu, C. Dai, M. Jia, D. Liu, S. Bao, J. Jiang, M. Xu, C. M. Li, *ACS Appl. Mater. Interfaces* **2016**, *8*, 16063-16070.

[139] C. Shen, C. Zhao, F. Xin, C. Cao, W.-Q. Han, *Electrochim. Acta* **2015**, *180*, 852-857.

[140] F. Zheng, Y. Yang, Q. Chen, *Nat. Commun.* **2014**, *5*, 5261.

[141] B. Chen, Z. Yang, G. Ma, D. Kong, W. Xiong, J. Wang, Y. Zhu, Y. Xia, *Microporous Mesoporous Mater.* **2018**, *257*, 1-8.

[142] G. Zou, J. Chen, Y. Zhang, C. Wang, Z. Huang, S. Li, H. Liao, J. Wang, X. Ji, *J. Power Sources* **2016**, *325*, 25-34.

[143] X. Zhang, G. Zhu, D. Yan, T. Lu, L. Pan, *J. Alloys Compd.* **2017**, *710*, 575-580.

[144] Z. Cui, Q. Liu, C. Xu, R. Zou, J. Zhang, W. Zhang, G. Guan, J. Hu, Y. Sun, *J. Mater. Chem. A* **2017**, *5*, 21699-21708.

[145] B. Sambandam, V. Soundharrajan, J. Song, S. Kim, J. Jo, D. P. Tung, S. Kim, V. Mathew, J. Kim, *Inorg. Chem. Front.* **2016**, *3*, 1609-1615.

[146] S. Niu, Z. Wang, T. Zhou, M. Yu, M. Yu, J. Qiu, *Adv. Funct. Mater.* **2017**, *27*, 1605332.

[147] Y. Guo, L. Zhang, *Nanoscale* **2020**, *12*, 7849-7856.

[148] S.-J. Zhang, J.-H. You, J.-D. Chen, Y.-Y. Hu, C.-W. Wang, Q. Liu, Y.-Y. Li, Y. Zhou, J.-T. Li, J. Światowska, L. Huang, S.-G. Sun, *ACS Appl. Mater. Interfaces* **2019**, *11*, 47939-47947.

[149] M.-K. Kim, M.-S. Kim, J.-H. Park, J. Kim, C.-Y. Ahn, A. Jin, J. Mun, Y.-E. Sung, *Nanoscale* **2020**, *12*, 15214-15221.

[150] C. Qu, B. Zhao, Y. Jiao, D. Chen, S. Dai, B. M. deglee, Y. Chen, K. S. Walton, R. Zou, M. Liu, *ACS Energy Lett.* **2017**, *2*, 1263-1269.

[151] W. Li, S. Watzele, H. A. El-Sayed, Y. Liang, G. Kieslich, A. S. Bandarenka, K. Rodewald, B. Rieger, R. A. Fischer, *J. Am. Chem. Soc.* **2019**, *141*, 5926-5933.

[152] J. Yu, X. Gao, Z. Cui, Y. Jiao, Q. Zhang, H. Dong, L. Yu, L. Dong, *Energy Technol.* **2019**, *7*, 1900018.

[153] Y. Yi, W. Zhao, Z. Zeng, C. Wei, C. Lu, Y. Shao, W. Guo, S. Dou, J. Sun, *Small* **2020**, *16*, 1906566.

[154] M. Xu, L. Han, Y. Han, Y. Yu, J. Zhai, S. Dong, *J. Mater. Chem. A* **2015**, *3*, 21471-21477.

[155] X. Xu, J. Feng, J. Liu, F. Lv, R. Hu, F. Fang, L. Yang, L. Ouyang, M. Zhu, *Electrochim. Acta* **2019**, *312*, 224-233.

[156] X. Yang, S. Wang, D. Y. W. Yu, A. L. Rogach, *Nano Energy* **2019**, *58*, 392-398.

[157] X.-R. Zeng, W.-W. Jin, H.-J. Li, S. Inguva, Q. Zhang, S.-Z. Zeng, G.-Z. Xu, J.-Z. Zou, *Nanotechnology* **2020**, *31*, 155602.

[158] Z.-X. Li, B.-L. Yang, K.-Y. Zou, L. Kong, M.-L. Yue, H.-H. Duan, *Carbon* **2019**, *144*, 540-548.

[159] X. Zhou, L. Chen, W. Zhang, J. Wang, Z. Liu, S. Zeng, R. Xu, Y. Wu, S. Ye, Y. Feng, X. Cheng, Z. Peng, X. Li, Y. Yu, *Nano Lett.* **2019**, *19*, 4965-4973.

[160] Q. Li, Z. Dai, J. Wu, W. Liu, T. Di, R. Jiang, X. Zheng, W. Wang, X. Ji, P. Li, Z. Xu, X. Qu, Z. Xu, J. Zhou, *Adv. Energy Mater.* **2020**, *10*, 1903750.

[161] K. Zhao, S. Liu, G. Ye, Q. Gan, Z. Zhou, Z. He, *J. Mater. Chem. A* **2018**, *6*, 2166-2175.

[162] L. Huang, X. Zhang, Y. Han, Q. Wang, Y. Fang, S. Dong, *J. Mater. Chem. A* **2017**, *5*, 18610-18617.

[163] P. Pachfule, D. Shinde, M. Majumder, Q. Xu, *Nat. Chem.* **2016**, *8*, 718-724.

[164] J. Tian, F. Jiang, D. Yuan, L. Zhang, Q. Chen, M. Hong, *Angew. Chem. Int. Ed.* **2020**, *59*, 13101-13108.

[165] B. Y. Guan, A. Kushima, L. Yu, S. Li, J. Li, X. W. Lou, *Adv. Mater.* **2017**, *29*, 1605902.

[166] M. D. Stoller, R. S. Ruoff, *Energy Environ. Sci.* **2010**, *3*, 1294-1301.

[167] G. Wang, L. Zhang, J. Zhang, *Chem. Soc. Rev.* **2012**, *41*, 797-828.

[168] K. M. Choi, H. M. Jeong, J. H. Park, Y.-B. Zhang, J. K. Kang, O. M. Yaghi, *ACS Nano* **2014**, *8*, 7451-7457.

[169] Y. Tan, W. Zhang, Y. Gao, J. Wu, B. Tang, *RSC Adv.* **2015**, *5*, 17601-17605.

[170] W. Gao, D. Chen, H. Quan, R. Zou, W. Wang, X. Luo, L. Guo, *ACS Sustain. Chem. Eng.* **2017**, *5*, 4144-4153.

[171] W.-H. Li, K. Ding, H.-R. Tian, M.-S. Yao, B. Nath, W.-H. Deng, Y. Wang, G. Xu, *Adv. Funct. Mater.* **2017**, *27*, 1702067.

[172] C. Qu, Y. Jiao, B. Zhao, D. Chen, R. Zou, K. S. Walton, M. Liu, *Nano Energy* **2016**, *26*, 66-73.

[173] R. Ramachandran, C. Zhao, D. Luo, K. Wang, F. Wang, *Electrochim. Acta* **2018**, *267*, 170-180.

[174] D. Y. Lee, D. V. Shinde, E.-K. Kim, W. Lee, I.-W. Oh, N. K. Shrestha, J. K. Lee, S.-H. Han, *Microporous Mesoporous Mater.* **2013**, *171*, 53-57.

[175] S. Sundriyal, V. Shrivastav, M. Sharma, S. Mishra, A. J. C. Deep, *ChemistrySelect* **2019**, *4*, 2585-2592.

[176] M. Du, M. Chen, X.-G. Yang, J. Wen, X. Wang, S.-M. Fang, C.-S. Liu, *J. Mater. Chem. A* **2014**, *2*, 9828-9834.

[177] J. Yang, C. Zheng, P. Xiong, Y. Li, M. Wei, *J. Mater. Chem. A* **2014**, *2*, 19005-19010.

[178] J. Xu, C. Yang, Y. Xue, C. Wang, J. Cao, Z. Chen, *Electrochim. Acta* **2016**, *211*, 595-602.

[179]   J. Yang, P. Xiong, C. Zheng, H. Qiu, M. Wei, *J. Mater. Chem. A* **2014**, *2*, 16640-16644.

[180]   Y. Zheng, S. Zheng, Y. Xu, H. Xue, C. Liu, H. Pang, *Chem. Eng. J.* **2019**, *373*, 1319-1328.

[181]   J. Yang, Z. Ma, W. Gao, M. Wei, *Chem. Eur. J.* **2017**, *23*, 631-636.

[182]   X. Liu, C. Shi, C. Zhai, M. Cheng, Q. Liu, G. Wang, *ACS Appl. Mater. Interfaces* **2016**, *8*, 4585-4591.

[183]   R. Du, Q. Feng, H. Ren, Q. Zhao, X. Gao, J. Zhang, *J. Mater. Chem. A* **2016**, *4*, 938-943.

[184]   Y. Yan, P. Gu, S. Zheng, M. Zheng, H. Pang, H. Xue, *J. Mater. Chem. A* **2016**, *4*, 19078-19085.

[185]   J. Hu, H. Wang, Q. Gao, H. Guo, *Carbon* **2010**, *48*, 3599-3606.

[186]   L. Gong, M. Xu, R. Ma, Y. Han, H. Xu, G. Shi, *Sci. China Technol. Sci.* **2020**, *63*, 1470-1477.

[187]   L. Zhang, J. Zhang, Y. Liu, L. Zhang, A. Yuan, *Journal of Nanoscience and Nanotechnology* **2017**, *17*, 2571-2577.

[188]   R. Bendi, V. Kumar, V. Bhavanasi, K. Parida, P. S. Lee, *Adv. Energy Mater.* **2016**, *6*, 1501833.

[189]   M. K. Wu, C. Chen, J. J. Zhou, F. Y. Yi, K. Tao, L. Han, *J. Alloys Compd.* **2018**, *734*, 1-8.

[190]   H. Mei, Y. Mei, S. Zhang, Z. Xiao, B. Xu, H. Zhang, L. Fan, Z. Huang, W. Kang, D. Sun, *Inorg. Chem.* **2018**, *57*, 10953-10960.

[191]   J. Cai, Y. Song, X. Chen, Z. Sun, Y. Yi, J. Sun, Q. Zhang, *J. Mater. Chem. A* **2020**, *8*, 1757-1766.

[192]   K. Jayaramulu, D. P. Dubal, B. Nagar, V. Ranc, O. Tomanec, M. Petr, K. K. R. Datta, R. Zboril, P. Gómez-Romero, R. A. Fischer, *Adv. Mater.* **2018**, *30*, 1705789.

[193]   P. Zhang, B. Y. Guan, L. Yu, X. W. Lou, *Angew. Chem. Int. Ed.* **2017**, *129*, 7247-7251.

[194]   W. Wang, L. Zhang, G. Xu, H. Song, L. Yang, C. Zhang, J. Xu, D. Jia, *Inorg. Chem.* **2018**, *57*, 10287-10294.

[195]   Z. Zhang, H. Yoshikawa, K. Awaga, *J. Am. Chem. Soc.* **2014**, *136*, 16112-16115.

[196]   Z. Zhang, H. Yoshikawa, K. Awaga, *Chem. Mater.* **2016**, *28*, 1298-1303.

[197]   C. Li, X. Hu, X. Lou, L. Zhang, Y. Wang, J.-P. Amoureux, M. Shen, Q. Chen, B. Hu, *J. Mater. Chem. A* **2016**, *4*, 16245-16251.

[198]   L. Shen, H. Song, C. Wang, *Electrochim. Acta* **2017**, *235*, 595-603.

[199]   C. Li, Q. Yang, M. Shen, J. Ma, B. Hu, *Energy Storage Materials* **2018**, *14*, 82-89.

[200]   A. Fateeva, P. Horcajada, T. Devic, C. Serre, J. Marrot, J.-M. Grenèche, M. Morcrette, J.-M. Tarascon, G. Maurin, G. Férey, *Eur. J. Inorg. Chem.* **2010**, *2010*, 3789-3794.

[201]   J. Shin, M. Kim, J. Cirera, S. Chen, G. J. Halder, T. A. Yersak, F. Paesani, S. M. Cohen, Y. S. Meng, *J. Mater. Chem. A* **2015**, *3*, 4738-4744.

[202]   T. Yamada, K. Shiraishi, H. Kitagawa, N. Kimizuka, *Chem. Commun.* **2017**, *53*, 8215-8218.

[203]   Z. Peng, X. Yi, Z. Liu, J. Shang, D. Wang, *ACS Appl. Mater. Interfaces* **2016**, *8*, 14578-14585.

[204]   S. Maiti, A. Pramanik, U. Manju, S. Mahanty, *ACS Appl. Mater. Interfaces* **2015**, *7*, 16357-16363.

[205]   H. Nagatomi, N. Yanai, T. Yamada, K. Shiraishi, N. Kimizuka, *Chem. Eur. J.* **2018**, *24*, 1806-1810.

[206]   S. Gu, Z. Bai, S. Majumder, B. Huang, G. Chen, *J. Power Sources* **2019**, *429*, 22-29.

[207]   C. D. Wessells, S. V. Peddada, M. T. McDowell, R. A. Huggins, Y. Cui, *J. Electrochem. Soc.* **2011**, *159*, A98-A103.

[208] L. Wang, Y. Lu, J. Liu, M. Xu, J. Cheng, D. Zhang, J. B. Goodenough, *Angew. Chem. Int. Ed.* **2013**, *125*, 2018-2021.

[209] Y. Lu, L. Wang, J. Cheng, J. B. Goodenough, *Chem. Commun.* **2012**, *48*, 6544-6546.

[210] P. Nie, L. Shen, G. Pang, Y. Zhu, G. Xu, Y. Qing, H. Dou, X. Zhang, *J. Mater. Chem. A* **2015**, *3*, 16590-16597.

[211] X. Wang, R. Kurono, S.-i. Nishimura, M. Okubo, A. Yamada, *Chem. Eur. J.* **2015**, *21*, 1096-1101.

[212] X. Han, F. Yi, T. Sun, J. Sun, *Electrochem. Commun.* **2012**, *25*, 136-139.

[213] S.-B. Xia, S.-W. Yu, L.-F. Yao, F.-S. Li, X. Li, F.-X. Cheng, X. Shen, C.-K. Sun, H. Guo, J.-J. Liu, *Electrochim. Acta* **2019**, *296*, 746-754.

[214] P. Nie, L. Shen, H. Luo, B. Ding, G. Xu, J. Wang, X. Zhang, *J. Mater. Chem. A* **2014**, *2*, 5852-5857.

[215] C. Li, X. Hu, X. Lou, Q. Chen, B. Hu, *Chem. Commun.* **2016**, *52*, 2035-2038.

[216] C. Li, X. Hu, W. Tong, W. Yan, X. Lou, M. Shen, B. Hu, *ACS Appl. Mater. Interfaces* **2017**, *9*, 29829-29838.

[217] X. Lou, Y. Ning, C. Li, M. Shen, B. Hu, X. Hu, B. Hu, *Inorg. Chem.* **2018**, *57*, 3126-3132.

[218] T. An, Y. Wang, J. Tang, Y. Wang, L. Zhang, G. Zheng, *J. Colloid Interface Sci.* **2015**, *445*, 320-325.

[219] Y. Lin, Q. Zhang, C. Zhao, H. Li, C. Kong, C. Shen, L. Chen, *Chem. Commun.* **2015**, *51*, 697-699.

[220] J. Park, M. Lee, D. Feng, Z. Huang, A. C. Hinckley, A. Yakovenko, X. Zou, Y. Cui, Z. Bao, *J. Am. Chem. Soc.* **2018**, *140*, 10315-10323.

[221] Y. An, H. Fei, Z. Zhang, L. Ci, S. Xiong, J. Feng, *Chem. Commun.* **2017**, *53*, 8360-8363.

[222] C. Li, X. Hu, B. Hu, *Electrochim. Acta* **2017**, *253*, 439-444.

[223] X. Wu, M. Sun, S. Guo, J. Qian, Y. Liu, Y. Cao, X. Ai, H. Yang, *Nat. Commun.* **2015**, *1*, 188-193.

[224] M. L. Aubrey, J. R. Long, *J. Am. Chem. Soc.* **2015**, *137*, 13594-13602.

[225] Y. Wang, Q. Qu, G. Liu, V. S. Battaglia, H. Zheng, *Nano Energy* **2017**, *39*, 200-210.

[226] D. Zhou, J. Ni, L. Li, *Nano Energy* **2019**, *57*, 711-717.

[227] H. Song, L. Shen, J. Wang, C. Wang, *J. Mater. Chem. A* **2016**, *4*, 15411-15419.

[228] Q. Liu, L. Yu, Y. Wang, Y. Ji, J. Horvat, M.-L. Cheng, X. Jia, G. Wang, *Inorg. Chem.* **2013**, *52*, 2817-2822.

[229] Z. Jiang, T. Liu, L. Yan, J. Liu, F. Dong, M. Ling, C. Liang, Z. Lin, *Energy Storage Materials* **2018**, *11*, 267-273.

[230] L. Chen, W. Yang, J. Wang, C. Chen, M. Wei, *Chemistry – A European Journal* **2018**, *24*, 13362-13367.

[231] N. Sharma, S. Szunerits, R. Boukherroub, R. Ye, S. Melinte, M. O. Thotiyl, S. Ogale, *ACS Appl. Energy Mater.* **2019**, *2*, 4450-4457.

[232] Y. Zhang, S. Yang, X. Chang, H. Guo, Y. Li, M. Wang, W. Li, L. Jiao, Y. Wang, *Chem. Commun.* **2018**, *54*, 11793-11796.

[233] Y. Liu, X. Zhao, C. Fang, Z. Ye, Y.-B. He, D. Lei, J. Yang, Y. Zhang, Y. Li, Q. Liu, Y. Huang, R. Zeng, L. Kang, J. Liu, Y.-H. Huang, *Chem* **2018**, *4*, 2463-2478.

[234] E. M. Miner, M. Dincă, *Philos. Trans. Royal Soc. A* **2019**, *377*, 20180225.

[235] B. M. Wiers, M.-L. Foo, N. P. Balsara, J. R. Long, *J. Am. Chem. Soc.* **2011**, *133*, 14522-14525.

[236] R. Ameloot, M. Aubrey, B. M. Wiers, A. P. Gómora-Figueroa, S. N. Patel, N. P. Balsara, J. R. Long, *Chem. Eur. J.* **2013**, *19*, 5533-5536.

[237] L. Shen, H. B. Wu, F. Liu, J. L. Brosmer, G. Shen, X. Wang, J. I. Zink, Q. Xiao, M. Cai, G. Wang, Y. Lu, B. Dunn, *Adv. Mater.* **2018**, *30*, 1707476.

[238] S. S. Park, Y. Tulchinsky, M. Dincă, *J. Am. Chem. Soc.* **2017**, *139*, 13260-13263.

[239] E. M. Miner, S. S. Park, M. Dincă, *J. Am. Chem. Soc.* **2019**, *141*, 4422-4427.

[240] J. Cepeda, S. Pérez-Yáñez, G. Beobide, O. Castillo, E. Goikolea, F. Aguesse, L. Garrido, A. Luque, P. A. Wright, *Chem. Mater.* **2016**, *28*, 2519-2528.

[241] S. Fischer, J. Roeser, T. C. Lin, R. H. DeBlock, J. Lau, B. S. Dunn, F. Hoffmann, M. Fröba, A. Thomas, S. H. Tolbert, *Angew. Chem. Int. Ed.* **2018**, *57*, 16683-16687.

[242] W. Xu, X. Pei, C. S. Diercks, H. Lyu, Z. Ji, O. M. Yaghi, *J. Am. Chem. Soc.* **2019**, *141*, 17522-17526.

[243] F. Zhu, H. Bao, X. Wu, Y. Tao, C. Qin, Z. Su, Z. Kang, *ACS Appl. Mater. Interfaces* **2019**, *11*, 43206-43213.

[244] M. L. Aubrey, R. Ameloot, B. M. Wiers, J. R. Long, *Energy Environ. Sci.* **2014**, *7*, 667-671.

[245] Q. Cheng, Y. Chen, X. Lin, J. Liu, Z. Yuan, Y. Cai, *J. Phys. Chem. C* **2020**, *124*, 8624-8632.

[246] S. Liu, J. Zhou, H. Song, *Small* **2018**, *14*, 1703548.

[247] Z. Xiu, M. H. Alfaruqi, J. Gim, J. Song, S. Kim, T. V. Thi, P. T. Duong, J. P. Baboo, V. Mathew, J. Kim, *Chem. Commun.* **2015**, *51*, 12274-12277.

[248] Z. Xiu, M. H. Alfaruqi, J. Gim, J. Song, S. Kim, P. T. Duong, J. P. Baboo, V. Mathew, J. Kim, *J. Alloys Compd.* **2016**, *674*, 174-178.

[249] Y. Zhang, Y. Lu, S. Feng, D. Liu, Z. Ma, S. Wang, *J. Mater. Chem. A* **2017**, *5*, 22512-22518.

[250] Y. Wang, B. Wang, F. Xiao, Z. Huang, Y. Wang, C. Richardson, Z. Chen, L. Jiao, H. Yuan, *J. Power Sources* **2015**, *298*, 203-208.

[251] Y. Feng, X.-Y. Yu, U. Paik, *Chem. Commun.* **2016**, *52*, 6269-6272.

[252] S. Wang, M. Chen, Y. Xie, Y. Fan, D. Wang, J.-J. Jiang, Y. Li, H. Grützmacher, C.-Y. Su, *Small* **2016**, *12*, 2365-2375.

[253] M. Wang, Y. Huang, Y. Zhu, N. Zhang, J. Zhang, X. Qin, H. Zhang, *Electrochim. Acta* **2020**, *335*, 135694.

[254] Y. Han, J. Li, T. Zhang, P. Qi, S. Li, X. Gao, J. Zhou, X. Feng, B. Wang, *Chem. Eur. J.* **2018**, *24*, 1651-1656.

[255] G. Fang, J. Zhou, Y. Cai, S. Liu, X. Tan, A. Pan, S. Liang, *J. Mater. Chem. A* **2017**, *5*, 13983-13993.

[256] Y. Song, Y. Chen, J. Wu, Y. Fu, R. Zhou, S. Chen, L. Wang, *J. Alloys Compd.* **2017**, *694*, 1246-1253.

[257] F. Wu, S. Zhang, B. Xi, Z. Feng, D. Sun, X. Ma, J. Zhang, J. Feng, S. Xiong, *Adv. Energy Mater.* **2018**, *8*, 1703242.

[258] J.-M. Fan, J.-J. Chen, Q. Zhang, B.-B. Chen, J. Zang, M.-S. Zheng, Q.-F. Dong, *ChemSusChem* **2015**, *8*, 1856-1861.

[259] K. J. Zhu, G. Liu, Y. J. Wang, J. Liu, S. T. Li, L. Y. Yang, S. L. Liu, H. Wang, T. Xie, *Mater. Lett.* **2017**, *197*, 180-183.

[260] S. Su, Q. Liu, J. Wang, L. Fan, R. Ma, S. Chen, X. Han, B. Lu, *ACS Appl. Mater. Interfaces* **2019**, *11*, 22474-22480.

[261] H.-J. Peng, G.-X. Hao, Z.-H. Chu, Y.-L. Cui, X.-M. Lin, Y.-P. Cai, *Inorg. Chem.* **2017**, *56*, 10007-10012.

[262] W. Zhang, X. Jiang, Y. Zhao, A. Carné-Sánchez, V. Malgras, J. Kim, J. H. Kim, S. Wang, J. Liu, J.-S. Jiang, Y. Yamauchi, M. Hu, *Chem. Sci.* **2017**, *8*, 3538-3546.

[263] P. Xiong, X. Zhao, Y. Xu, *ChemSusChem* **2018**, *11*, 202-208.

[264] G. Huang, F. Zhang, L. Zhang, X. Du, J. Wang, L. Wang, *J. Mater. Chem. A* **2014**, *2*, 8048-8053.

[265] H. Li, M. Liang, W. Sun, Y. Wang, *Adv. Funct. Mater.* **2016**, *26*, 1098-1103.

[266] X. Xu, K. Cao, Y. Wang, L. Jiao, *J. Mater. Chem. A* **2016**, *4*, 6042-6047.

[267] L.-L. Wu, Z. Wang, Y. Long, J. Li, Y. Liu, Q.-S. Wang, X. Wang, S.-Y. Song, X. Liu, H.-J. Zhang, *Small* **2017**, *13*, 1604270.

[268] F. Zou, X. Hu, Z. Li, L. Qie, C. Hu, R. Zeng, Y. Jiang, Y. Huang, *Adv. Mater.* **2014**, *26*, 6622-6628.

[269] J. Liu, Y. Fang, L. Zeng, J. Liu, L. Xu, J. Luo, B. Huang, Q. Qian, M. Wei, Q. Chen, *J. Alloys Compd.* **2020**, *817*, 152728.

[270] Y. Wang, C. Wang, Y. Wang, H. Liu, Z. Huang, *J. Mater. Chem. A* **2016**, *4*, 5428-5435.

[271] L. Kong, C.-C. Xie, H. Gu, C.-P. Wang, X. Zhou, J. Liu, Z. Zhou, Z.-Y. Li, J. Zhu, X.-H. Bu, *Small* **2018**, *14*, 1800639.

[272] C. Liu, Y. Li, D. Lin, P.-C. Hsu, B. Liu, G. Yan, T. Wu, Y. Cui, S. Chu, *Joule* **2020**, *4*, 1459-1469.

[273] Z. Ji, T. Li, O. M. Yaghi, *Science* **2020**, *369*, 674.

[274] Y. Seo, P. A. Shinde, S. Park, S. Chan Jun, *Electrochim. Acta* **2020**, *335*, 135327.

[275] C. Li, T. Chen, W. Xu, X. Lou, L. Pan, Q. Chen, B. Hu, *J. Mater. Chem. A* **2015**, *2015 v.3 no.10*, pp. 5585-5591.

[276] Z. Bai, Y. Zhang, Y. Zhang, C. Guo, B. Tanga, D. Sun, *J. Mater. Chem. A* **2015**.

[277] Y. V. Kaneti, J. Zhang, Y.-B. He, Z. Wang, S. Tanaka, M. S. A. Hossain, Z.-Z. Pan, B. Xiang, Q.-H. Yang, Y. Yamauchi, *J. Mater. Chem. A* **2017**, *5*, 15356-15366.